Proteolytic and Mechanical Matrix Remodeling During Capillary Morphogenesis

by

Benjamin Juliar

A dissertation submitted in partial fulfillment
of the requirements for the degree of
Doctor of Philosophy
(Biomedical Engineering)
In the University of Michigan
2020

Doctoral Committee:

Professor Andrew Putnam, Chair
Professor David Antonetti
Assistant Professor Brendon Baker
Professor Jan Stegeman

Benjamin Juliar

bjuliar@umich.edu

ORCID iD: 0000-0003-4828-9053

DEDICATION

This dissertation is dedicated to the future students and scientists who will build upon this work.

ACKNOWLEDGEMENTS

First and foremost, I would like to thank my advisor Andrew Putnam for taking me into his lab. I truly appreciate all the collaborations and personal ideas you gave me space to pursue and even though we haven't always agreed, I always felt that you had my best interests at heart. I would also like to thank my committee members; Jan Stegemann, Brendon Baker and David Antonetti. I have appreciated all of your helpful insights and support in preparing to graduate.

I would like to thank Mark Keating ad Elliot Botvinick at UC Irvine, who contributed equally as first and supporting authors for Chapter 3. Thank you for your help with conceiving the experiments and performing active microrheology and confocal reflection microscopy as a function of time. I would also like to thank Yen Kong for his contribution to Chapter 3 in developing the bulk rheological methods and training me in their application.

I want to give a particular thanks to Jeff Beamish, who contributed equally to Chapter 4 and Chapter 6. Your rigorous work ethic was truly an inspiration. I would also like to thank the undergraduates David S. Cleveland, Megan E. Busch and Likitha Nimmagada for all of your help writing code, imaging and analyzing experiments, and performing RNA isolations, purifications and quantifications, you were all an important part of the engine that drove my research.

I want to give huge thanks to the former PhD students out of the Cell Signaling and Engineered Tissues (CSET) lab, Jonathan Bezenah and Ana Rioja, thank you for helping me get started by training me in basic techniques. I would also like to thank the newer members of the lab, Emily Margolis and Nicole Friend, you two have been such a joy to work with and I am sure great things lie ahead for you both.

I would also like to acknowledge my funding sources. Much of the research reported in this dissertation was supported by the National Heart, Lung, and Blood Institute of the National Institutes of Health under Award Number R01-HL085339. I also want to acknowledge the support I received from the Tissue Engineering and Regeneration Training Program at the University of Michigan (T32-DE007057) and by the Training Program in Translational Cardiovascular Research and Entrepreneurship (T32-HL125242). David Kohn, thank you for all the blunt advice and guidance you've given me and my fellow trainees. Dan Michele, thank you for choosing me to join CVRE, the hands-on experience in mouse surgical models and the exposure to entrepreneurship the program provided were both fantastic.

Last, but not least, I would like to thank all my friends and family for all of the support along the way. Thank you to all of my fellow researchers in LBME for all of the great chats over lunch and during coffee hours. Thank you Mom and Dad for listening over and over as I tried to explain what I'm working on, and thank you Becca, Nate and Zach for being impressed regardless of how much you understood what I was talking about, I love you all very much. Most importantly, thank you Dana, my love, for always bringing joy to my life and listening endlessly as a sounding board for ideas. Your support and celebration of my successes has meant the world to me.

Table of Contents

LIST OF FIGURES

LIST OF VIDEOS

LIST OF APPENDICES

LIST OF ABBREVIATIONS

2D	2-dimensional
2xVPMS	crosslinking peptide: GCRDVPMSMRGGVPMSMRGGDRCG
3D	3-dimensional
α-SMA	alpha-smooth muscle actin
ACTA2	alpha-smooth muscle actin gene abbreviation
AMR	active microrheology
ANOVA	analysis of variance
ANTXR2	capillary morphogenesis gene 2 protein gene abbreviation
bFGF	basic fibroblast growth factor
BM	basement membrane
BSA	bovine serum albumin
cDNA	complementary deoxyribonucleic acid
CMG	capillary morphogenesis gene 2 protein
COL1A1	collagen 1, alpha 1 chain gene abbreviation
COL4A1	collagen 4, alpha 1 chain gene abbreviation
DAPI	4',6-diamidino-2-phenylindol
DFs	dermal fibroblasts
DMEM	Dulbecco's modified eagle medium
DMSO	dimethyl sulfoxide
DSU	disk scanning unit
Dual	crosslinking peptide: GCYKNRDVPMSMRGGDRCG
ECFCs	endothelial colony forming cells
ECM	extracellular matrices
ECs	endothelial cells
EDTA	ethylenediaminetetraacetic acid
EGM	Lonza endothelial growth media-2
EPCs	endothelial progenitor cells
FBS	fetal bovine serum
FN1	fibronectin gene abbreviation
G'	real component of the complex shear modulus
GAPDH	glyceraldehyde 3-phosphate dehydrogenase
HEPES	4-(2-hydroxyethyl)-1-piperazineethanesulfonic acid
HRP	horseradish peroxidase
HUVECs	human umbilical vein endothelial cells
IC50	the half maximal inhibitory concentration
IgG	immunoglobulin g

KDR	vascular endothelial growth factor receptor gene abbreviation
LAMB1	laminin, beta 1 chain gene abbreviation
LFs	lung fibroblasts
MMP	matrix metalloproteinase
MSCs	mesenchymal stem cells
MT-MMP	membrane-type matrix metalloproteinase
MVECs	microvascular endothelial cells
NG2	neural-glial antigen-2
PBS	phosphate buffered saline
PCR	polymerase chain reaction
PDGF	platelet-derived growth factor
PDGFB	platelet derived growth factor-β gene abbreviation
PDGFRB	platelet derived growth factor receptor-β gene abbreviation
PEG	poly(ethylene glycol)
PEG-VS	poly(ethylene glycol)-vinyl sulfone
PVDF	polyvinylidene fluoride
R^2	statistical coefficient of determination
RGD	adhesive peptide: CGRGDS
RhoA	ras homolog family member a
RNA	ribonucleic acid
ROI	region of interest
SCID	severe combined immunodeficiency
STICS	spatio-temporal image correlation spectroscopy
TBS	tris-buffered saline
TFM	traction force microscopy
TGF-α	transforming growth factor-α
TGFβ	transforming growth factor β1
TIMP	tissue inhibitor of metalloproteinases
tPA	tissue plasminogen activator
UEA	ulex europaeus agglutinin-1
uPA	urokinase-type plasminogen activator
VEGF	vascular endothelial growth factor
VEGFR-2	vascular endothelial growth factor receptor-2
VL	Vasculife VEGF medium
VPMS	crosslinking peptide: GCRDVPMSMRGGDRCG
YD-KND-R	crosslinking peptide: GCY(K_D)N(R_D)DCG
YKNR	crosslinking peptide: GCYKNRDCG
Z-fix	zinc-buffered formalin solution

ABSTRACT

Engineering large viable tissues requires techniques for encouraging rapid capillary bed formation to prevent necrosis. A convenient means of creating this micro-vascular network is through spontaneous neovascularization, which occurs when endothelial cells (ECs) and supportive stromal cells are co-encapsulated within a variety of hydrogel-based extracellular matrices (ECM) and self-assemble into an interconnected network of endothelial tubules. Although this is a robust phenomenon, the environmental and cell-specific determinants that affect the rate and quality of micro-vascular network formation still require additional characterization to improve clinical translatability. This thesis investigates how the proteolytic susceptibility of engineered matrices effects neovascular self-assembly in poly(ethylene glycol) (PEG) hydrogels and provides characterization of changes to matrix mechanics that accompany neovascular morphogenesis in fibrin and PEG hydrogels.

Proteolytic ECM remodeling is essential for the process of capillary morphogenesis. Pharmacological inhibitor studies suggested a role for both matrix metalloproteinases (MMP)- and plasmin-mediated mechanisms of ECM remodeling in an EC-fibroblast co-culture model of vasculogenesis in fibrin. To further investigate the potential contribution of plasmin mediated matrix degradation in facilitating capillary morphogenesis we employed PEG hydrogels engineered with proteolytic specificity to either MMPs, plasmin, or both. Although fibroblasts spread in plasmin-selective hydrogels, we only observed robust capillary morphogenesis in MMP-sensitive matrices, with no added benefit in dual susceptible hydrogels. Enhanced capillary morphogenesis was observed, however, in PEG hydrogels engineered with increased

susceptibility to MMPs without altering proteolytic selectivity or hydrogel mechanical properties. These findings highlight the critical importance of MMP-mediated ECM degradation during vasculogenesis and justify the preferential selection of MMP-degradable peptide crosslinkers in the design of synthetic hydrogels used to promote vascularization.

Matrix stiffness is a well-established cue in cellular morphogenesis, however, the converse effect of cellular remodeling on environmental mechanics is comparatively under characterized. In fibrin hydrogels, we applied traditional bulk rheology and laser tweezers-based active microrheology to demonstrate that both ECs and fibroblasts progressively stiffen the ECM across length scales, with the changes in bulk properties dominated by fibroblasts. Despite a lack of fibrillar architecture, a similar stiffening effect was observed in MMP-degradable PEG hydrogels. This stiffening tightly correlated with degree of vessel formation and critically depended on active cellular contractility. To a lesser degree, deposition of ECM proteins also appeared to contribute to progressive hydrogel stiffening. Blocking cell-mediated hydrogel degradation abolished stiffening, demonstrating that matrix metalloproteinase (MMP)-mediated remodeling is required for stiffening to occur. EC co-culture with mesenchymal stem cells (MSCs) in PEG resulted in reduced vessel formation compared to fibroblast co-cultures and no change in hydrogel mechanics over time. The correlation between matrix stiffening and enhanced vessel formation, and dependence on cellular contractility, suggests differences in vessel formation between fibroblasts and MSCs may be partially mediated by differences in cellular contractility. Collectively, these findings provide a deeper understanding of mechanobiological effects during capillary morphogenesis and highlight the dynamic reciprocity between cells and their mechanical environment

CHAPTER I. Introduction

1.1 Motivation, initial hypothesis, objectives, and summary of scientific contributions

Engineering vascularized viable tissues requires techniques for encouraging rapid capillary bed formation to prevent tissue necrosis. Spontaneous neovascularization is a convenient means of creating this microvascular network, which occurs when a variety of endothelial and supportive stromal cells are co-encapsulated within natural and synthetic hydrogel-based extracellular matrices (ECM) (1) and self-assemble into an interconnected network of endothelial tubules. This morphogenetic process is controlled by biomolecular signaling (2), integrin mediated signaling (3), ECM proteolytic degradation (4, 5), and through cellular mechanosensing (6). Although there is a breadth of knowledge characterizing how these cellular cues regulate vessel formation, there is still a critical need for translating these mechanistic insights into the rational design of tissue constructs that support the formation of extensive vascular networks. In particular, the work presented in this dissertation focuses on characterizing the interdependence of ECM proteolytic degradation and cell-mediated changes to matrix mechanics with the rate of vessel formation in engineered tissues to further our understanding of tissue design criteria that support extensive vascularization.

Matrix metallo-proteinases are widely considered to be the primary class of ECM proteinases involved in regulating capillary morphogenesis (4, 5). Previous work in our lab, however, has also suggested a plasmin-mediated contribution to angiogenic sprouting in fibrin for certain co-culture models (7). Our lab observed accelerated vessel formation in fibrin

hydrogels when endothelial cells (ECs) were co-encapsulated with fibroblasts compared to mesenchymal stem cells (MSCs) as the supportive stromal cell types and this was correlated with plasmin activity (7). A plasmin-mediated contribution to angiogenic sprouting may either be due to direct matrix degradation (8) or through plasmin-mediated MMP activation (9). This accelerated vessel formation also correlated with reduced barrier function for ECs co-encapsulated with fibroblasts compared to with MSCs (10, 11). However, despite these previous observations, some conflicting reports have demonstrated a lack of plasmin-mediated effects during capillary morphogenesis both *in vivo* (8) and *ex vivo* (12). As such, there remains a knowledge gap in understanding the circumstances and through what mechanism plasmin may contribute to capillary morphogenesis. To address this knowledge gap, and based on our previous observations, our initial hypothesis was that global plasmin-mediated fibrinolysis in the presence of fibroblasts contributes to accelerated capillary network formation and may concurrently result in network destabilization and functional immaturity.

The initial objective of this thesis was to assess whether enhanced ECM proteolytic degradation, either by plasmin or MMPs, facilitates accelerated vessel formation. In an effort to determine whether global plasmin-mediated fibrinolysis occurs during capillary morphogenesis in the presence of fibroblasts, we first investigated whether a combination of active microrheology (AMR) and bulk shear rheology to track matrix mechanics across length scales could be used to observe ECM degradation over time in fibrin. Additionally, a synthetic poly(ethylene glycol) (PEG) based hydrogel with selective proteolytic susceptibility to MMPs, plasmin, or both, was used to assess whether direct plasmin-mediated matrix degradation facilitates capillary morphogenesis. Results from these studies, however, did not support our initial hypothesis; proteolysis did not have a detectable contribution to changes in matrix

mechanics in fibrin and plasmin-mediated matrix degradation did not appear to substantially contribute to capillary morphogenesis in PEG hydrogels. Increasing PEG-hydrogel susceptibility to MMPs did however accelerate vessel formation. These results help illustrate the ubiquitous contribution of MMPs for vessel formation, whereas plasmin may only play a substantive role in limited circumstances. Moreover, these results inform the design of synthetic matrices intended to support capillary morphogenesis by suggesting the importance of focusing research efforts on MMP-degradable matrices rather than plasmin- or dual-degradable matrices.

The work presented in this thesis also provides insights into cell-mediated changes to matrix mechanics both in fibrin and PEG. In both hydrogel systems capillary morphogenesis was accompanied by progressive hydrogel stiffening rather than our initial expectation of softening which would be indicative of degradation. Although there is substantial work investigating the effect of environmental mechanics on capillary morphogenesis (13), the converse effect of capillary morphogenesis on changes to environmental mechanics is highly understudied. Results from this thesis provide insights into cell-population specific contributions to changes in matrix mechanics on both the macro and micro scale in fibrin as well as the contribution of essential cellular-remodeling processes to changes in matrix mechanics. This work also demonstrates a dependence on initial matrix mechanics as well as supportive stromal cell type in PEG on affecting degree of stiffening. Continuing to develop an understanding of cellular remodeling associated with capillary morphogenesis is essential for designing engineered tissues that support extensive vascular network formation. In addition to characterizing cellular remodeling processes that occur during capillary morphogenesis in engineered tissues, these results also help support the concept of a dynamic and reciprocal relationship between cellular behavior and

environmental properties by demonstrating that initial matrix mechanics may alter cellular behavior associated with changes to matrix mechanics over time.

1.2 Overview of dissertation

Chapter 1 introduces the motivation and the contents of the studies presented in this thesis.

Chapter 2 provides a review of capillary morphogenesis in physiology and in engineered tissues. The role of biomolecular signaling, ECM proteolytic degradation, integrin mediated signaling, and cellular mechanosensing are covered. Different cell types and matrices that have been used for supporting vascular network formation in engineered tissues as well as applications in regenerative medicine are also introduced.

In **Chapter 3**, micro- and macro-scale hydrogel mechanical properties were tracked over time in a model of angiogenic sprouting supported by fibroblasts in fibrin. Active microrheology and bulk shear rheology were used to assess whether changes in ECM mechanics could be used as a surrogate for assessing proteolytic degradation. Contrary to an expected softening of hydrogels over time, a pronounced matrix stiffening was observed. Contributions from ECs and fibroblasts both contributed to this observed stiffening effect. This observation has potential mechanobiological implications when applying similar models of capillary morphogenesis to vascularize tissue constructs in which control of mechanical properties is an important consideration.

In **Chapter 4**, a proteolytically degradable PEG-based hydrogel crosslinked with peptides selectively susceptible to MMPs, plasmin, or both, was used to assess whether plasmin-mediated matrix degradation facilitates capillary morphogenesis. Robust capillary network formation was observed in MMP-selective matrices, but network formation was impeded in

plasmin-selective matrices despite robust fibroblast spreading. No morphological differences were observed in comparative studies between MMP-selective and dual-sensitive peptide crosslinkers. These results suggest MMP-mediated matrix degradation is the dominant contributor to capillary morphogenesis in this culture model. We were surprised to observe that MMP-selective hydrogels stiffened over time, similar to our observations in fibrin, and this phenomenon is further investigated in subsequent chapters.

Chapter 5 presents initial studies demonstrating that enhancing PEG-hydrogel crosslinker susceptibility to MMP-mediated degradation, without altering other hydrogel properties results in accelerated vessel formation. A preliminary study comparing morphogenetic behavior depending on crosslink identity in a subcutaneous implant model is then presented.

In **Chapter 6**, we further characterized our observation that soft MMP-selective PEG-hydrogels dramatically stiffen over time. Enhanced vessel formation in our softest hydrogel formulation correlated with pronounced hydrogel stiffening over time. This effect was dependent on active cellular contractility and correlated with increased expression of alpha smooth muscle actin. Upregulation and increased deposition of collagen 1 was also correlated with stiffening suggesting ECM deposition may contribute to changes in matrix mechanics over time. Like our results in fibrin, these findings are contextualized for their mechanobiology implications.

Chapter 7 presents preliminary studies demonstrating that capillary morphogenesis proceeding in the presence of MSCs results in reduced hydrogel stiffening compared to fibroblasts in both fibrin and PEG. Because hydrogel stiffening strongly depends on active cellular contractility, these results suggest accelerated rates of vessel formation in the presence of fibroblasts compared to MSCs may in part be due to differences in contractility.

Chapter 8 provides an overview of the work presented herein, discusses the relevance of these findings for the rational design of vascularized tissue constructs, and offers suggestions for future work that could be performed.

Chapter II. Background

2.1 CARDIOVASCULAR PHYSIOLOGY AND DEVELOPMENT

2.1.1 Cardiovascular physiology

The cardiovascular system is comprised of the heart, blood vessels, and blood. Its primary functions are to transport oxygen, nutrients and endocrine signals to tissues throughout the body and for the removal of metabolic waste. Systemic circulation carries oxygenated blood away from the heart through the aorta which then branches into arteries and then further into arterioles and finally capillaries where diffusive transport between the circulatory system and interstitia occurs. Deoxygenated blood is then returned to the heart through venules which merge into veins and drain in to the superior and inferior vena cava which empty into the heart (14).

Arteries, arterioles, capillaries, venules, and veins each have different architectures (**Fig 2.1**, adapted from (15)) but are generally comprised of an internal endothelial layer, extracellular matrix components, and an external layer of cells which provide structural support for the blood vessel termed mural cells as shown in. Arteries and veins have internal lumen diameters ranging from ~30mm for the aorta and vena cava to ~0.1 mm for small arteries and veins, arterioles and venules have lumen diameters from 20 - 100 microns and capillaries have lumen diameters between 5 – 20 microns (14, 16, 17). Arteries and large arterioles have much thicker walls then veins and large venules to resist the high blood pressures they encounter, but the walls of each of these types of blood vessels are comprised of 3 layers: the tunica externa, the tunica media, and the intima. The tunica externa is primarily collagenous connective tissue and is supported by the

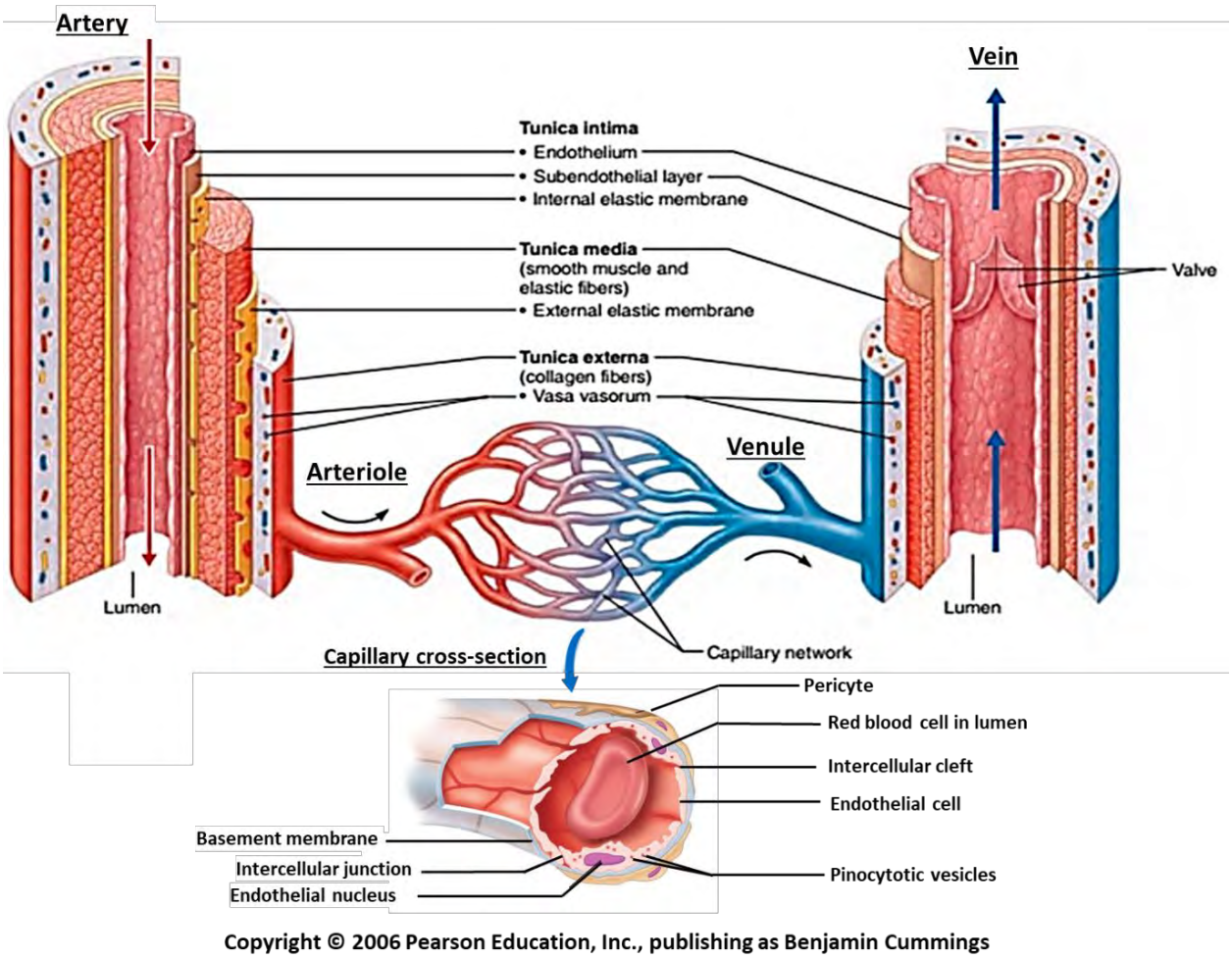

Figure 2.1: Hierarchical organization and structure of blood vessels. The organization and direction of blood flow through arteries, arterioles, capillaries, venules and veins is shown with major components of blood vessel structure.

external elastic lamina. The tunica media is comprised of smooth muscle cells and elastic tissue. The intima is comprised of the endothelium and is supported by the internal elastic membrane. These layers provide structural support, regulate blood flow, and are impermeable, whereas capillaries are selectively permeable to allow diffusion with interstitial tissues (17).

2.1.2 Capillary structure and function

Capillaries are the smallest vascular structure with diameters comparable to single red blood cells (18). As in all blood vessels, endothelial cells form the interior lining of capillaries, but in small capillaries a single cell may wrap around the lumen to contact itself. This endothelial layer

is ensheathed in a layer of ECM material termed the basement membrane (BM). The BM provides physical support, helps regulate cell behavior, and is primarily comprised of collagen IV, laminin, heparan-sulphate proteoglycans, and nidogen (19). Mural cells for capillaries are termed pericytes. Pericytes are embedded within the endothelial BM and make multiple forms of contact with ECs including cell-cell junctions, notably mediated through N-cadherin, fibronectin-rich adhesion plaques, and connexin-43 (20–27).

Pericytes tend to be located over tight junction regions and contribute to endothelial barrier function (28). Pericyte expression of α-SMA, primarily in pre-capillary regions surrounding arterioles also suggests their role in regulating capillary bed blood flow (28). The ratio of ECs to pericytes ranges from 1:1 to 1:100 depending on tissue type, with the degree of coverage corresponding to tissue-specific endothelial barrier function (25). Very low pericyte coverage in skeletal muscle, in which capillaries are continuous and maintain baseline barrier function excluding solutes larger than ~3 nm diameter (29) suggests their presence may be somewhat dispensable in some tissues. Enhanced pericyte coverage is also typically associated with reduced EC turnover (30).

The three types of capillaries are continuous, fenestrated, and sinusoidal. Each type of capillary differs in its anatomical location and permeability. Continuous capillaries are most common, occurring in skin, muscles, lungs, and brain, and have the lowest molecular permeability. Tight junctions between all adjacent endothelial cells helps restrict the paracellular diffusion of molecules greater than 4k Da in the blood-brain barrier (31). Fenestrated capillaries have an intermediate molecular permeability and are found in endocrine glands, renal glomeruli, and intestinal villi. The intercellular junctions of fenestrated capillaries are less well developed, and the endothelial cells are fenestrated, containing 50-100 nm wide pores that span the endothelium.

Sinusoidal capillaries are discontinuous with gaps large enough for blood cells to pass through and are found in the liver, spleen and bone marrow (17).

2.1.3 Overview of embryonic vasculogenesis and angiogenesis

The cardiovascular system is the first functional organ to develop during embryogenesis, playing an essential role in nutrient transport as well as endocrine signaling (32). Vasculogenesis is defined as the initial formation of a vascular network during embryogenesis in which angioblasts arrange into a network of cords and subsequently mature into the primary vascular plexus (33). This process occurs following gastrulation with the derivation of hemangioblasts from mesodermal cells. Hemangioblasts are multipotent stem cells believed to be precursors for both hematopoietic and endothelial cells (34). Hemangioblasts coalesce in the mesoderm to form blood islands. Peripheral hemangioblasts in blood islands differentiate into angioblasts and go on to form endothelial cells, whereas interior hemangioblasts differentiate into hematopoietic cells. These blood islands self-assemble into a network of cords, which become lumenized as angioblasts continue to differentiate into endothelial cells forming the primary capillary plexus (32).

Two mechanisms of lumenogenesis have been observed in *in vitro* and *in vivo* models termed cell hollowing and cord hollowing. In the process of cell hollowing, new lumens emerge intracellularly through the coalescence of intracellular vacuoles to form a central lumen which connects with vacuoles in adjacent cells. During the process of cord hollowing, however, luminal space is formed extracellularly in the center of the cord as ECs remain adhered around the periphery of the cord (35). Although these processes appear to differ depending on species and anatomical location, and have not been well characterized during human development (35), processes indicative of cord hollowing have been observed during lumen formation in the developing mouse aorta (36).

After lumenization, the primary capillary plexus is then reshaped into a hierarchical network of vessels and extends throughout the embryo via angiogenic remodeling and sprouting angiogenesis. Angiogenesis is broadly defined as either the sprouting of new vessels from the wall of preexisting vessels or the remodeling of preexisting vessels resulting in morphological changes in size or arrangement (32). Early remodeling processes result in the formation of the primitive heart. Angiogenic blood islands join to form endocardial tubes, which during embryonic folding fuse to form the primitive heart tube. The primitive heart tube begins to beat on day 22, circulation starts on days 27-29. Circulation contributes to continued vascular remodeling. The embryonic heart and cardiovascular system resemble the post-natal system by week 30, but they continue to grow and develop throughout most of gestation (37).

2.2 OVERVIEW OF ANGIOGENIC REMODELING

Angiogenic remodeling includes intussusception, anastomosis, regression and arteriogenesis (32). Intussusceptive angiogenesis is the splitting of pre-existing vessels, initiated by the formation of pillar-like microstructures that span the endothelial lumen and extend to split the lumen into distinct microvessels. Intussusceptive remodeling is particularly important for the rapid expansion of the alveolar capillary bed during lung development in the mouse (38). Anastomosis, also known as inosculation, is the bridging between lumens of two distinct vessels which have come in contact. During anastomosis, the basement membrane of abutting vessels degrades at the point of contact, allowing new tight junctions to form between apposing ECs, then subsequent selective loss of tight junctions allows lumens to connect (32). During development, anastomosis plays an important role in the formation of the aorta (39). Inosculation between vascularized tissue constructs and the host vascular system is essential for their efficacy. Characterizing, improving, and accelerating this process is a central goal in tissue engineering

(40). Capillary regression occurs when endothelial cells undergo programmed cell death or retract and reincorporate into adjacent vessels. Regression often occurs through genetically determined processes, with the cessation of blood flow, or reduction of growth-factor mediated maintenance, and is important during development and for pruning of redundant vessels (32). Arteriogenesis is the circumferential expansion of arterioles to accommodate increased blood flow, and is activated by increased fluid shear stress and circumferential wall stress caused by increased blood pressure (41). Activation of the endothelium from these physical forces contributes to basement membrane degradation, leukocyte invasion, proliferation of endothelial and smooth muscle cells, and neointima formation resulting in vessel enlargement (42).

2.3 ANGIOGENIC SPROUTING

2.3.1 Overview of angiogenic sprouting

Blood vessels are normally quiescent in adults but can be induced to undergo angiogenic sprouting during wound recovery or because of ischemia. Cytokine signaling induces disassociation of pericytes and degradation of the basement membrane resulting in vessel hyperpermeability and leakage of blood plasma proteins into the interstitial space creating a local proangiogenic provisional matrix rich with fibrin, fibronectin, and vitronectin (3). Accepted dogma is that newly forming sprouts are led by a migratory endothelial tip cell, characterized by numerous filopodia, which integrates environmental cues to dictate direction of growth. The tip cell leads stalk cells, which are highly proliferative and maintain intercellular junctions to ensure the stability of the newly forming vessel (43). Vessels return to quiescence as proangiogenic signaling subsides, new basement membrane is deposited, and pericytes are recruited (44).

2.3.2 Induction of angiogenic sprouting

Hypoxia is a potent inducer of angiogenic sprouting. Most transcriptional changes in response to hypoxia are regulated by hypoxia inducible factors (HIFs). HIFs help promote endothelial cell proliferation and migration, induce vasodilation and vascular permeability, ECM and BM degradation, and recruitment of pericytes to newly forming vessels (45). Notable signaling molecules that stimulate angiogenesis include vascular endothelial growth factor (VEGF), basic fibroblast growth factor (bFGF), transforming growth factor-α (TGF-α), platelet-derived growth factor (PDGF), and angiopoietin-1 and -2 (Ang-1 and Ang-2). VEGF is a well-known EC mitogen and induces tight (46) and adherens (47) junction disassembly. There is a large family of VEGF molecules with various isoforms that are either cell membrane-bound, ECM-bound, or soluble (48). Thrombin, which converts fibrinogen to fibrin initiating blood clot formation, induces hyperpermeability and enhances angiogenesis via an RGD-binding sequence that interacts with $\alpha_v\beta_3$ on endothelial cells (49). Fibroblasts, the most common connective tissue cell type, help mediate the pro-angiogenic response, upregulating VEGF under hypoxia (50). Fibroblasts secrete angiogenic growth factors that support EC invasiveness and lumen formation (51, 52). Ang-1 has been shown to act cooperatively with VEGF to induce angiogenesis despite mural cell induced quiescence (53). Intracellular signaling molecules that increase permeability and are typically associated with angiogenesis include elevated intracellular calcium and activation of protein kinase C (PKC), myosin light-chain kinase (MLCK), Src family kinases, and the small GTPase RhoA (54).

2.3.3 Proteolysis in Capillary Morphogenesis

Proteinases are key regulators of angiogenic sprouting, contributing to BM and interstitial ECM degradation, liberation of ECM sequestered cytokines, and activation of proteolytic and bioactive zymogens (4). Matrix metalloproteinases (MMPs), and in particular the membrane-

type (MT)-MMPs are critical mediators of matrix remodeling during angiogenic sprouting (7, 12, 55, 56). MMPs are secreted as inactive zymogens and their catalytic activity is tightly regulated (8). MT1-MMP contributes to both direct matrix degradation and intracellular signaling to coordinate lumen formation (57). MMP-mediated ECM proteolysis is widely regarded as the predominant class of enzymes regulating capillary morphogenesis (4). However, in some conditions the serine protease plasmin, which is also activated at the cell membrane, has been demonstrated to contribute to capillary morphogenesis (8, 58–60).

Plasminogen is activated to plasmin by urokinase (uPA) and by tissue plasminogen activator (tPA). Plasmin is a serine-protease with broad spectrum tryptic activity capable of hydrolyzing fibrin (8). Plasmin is also known to contribute to the activation of certain MMP proenzymes (9) and uPA is upregulated in response to bFGF (61). Inhibition of plasmin in an *in vitro* model of capillary morphogenesis in a supraphysiologic concentration of fibrin restricted vessel formation (62). Plasmin binding to $\alpha_v\beta_3$ on endothelial cells has been shown to induce endothelial migration (63). These observations suggest the plasmin/uPA system may play a role in capillary morphogenesis either through direct matrix degradation and/or through regulation of MMPs, but studies have contrarily demonstrated that normal vascular development and wound healing proceed in plasminogen null mice (8) and that plasminogen is not necessary for angiogenic sprouting in an *ex vivo* model (12).

2.3.4 Mechanosensitive effects in capillary morphogenesis

An early demonstration of mechanical forces contributing to capillary morphogenesis was the observation of deformations of a flexible silicon rubber substrate coated with Matrigel during EC cord self-assembly (6) The laminin receptor α6β1 was essential for endothelial self-assembly into cord like structures and for Matrigel deformation (6). Endothelial cells have been

shown to apply forces to and deform individual ECM fibers during network formation in fibrin (64) and in a pseudo-3D network of synthetic fibers (65, 66). Cyclic mechanical strain applied to ECs in 2D culture have been shown to promote proliferation through a mechanosignaling cascade initiated by vascular endothelial growth factor receptor-2 (VEGFR-2) activation (67). In a 3D model of angiogenic sprouting in fibrin with cyclic strain applied to the hydrogels, endothelial cells tended to sprout parallel to the direction of applied strain (68). Gradients in mechanical properties of hydrogels have also been shown to direct angiogenic sprouting from spheroids, with more extensive outgrowth parallel to the direction of the gradient (69).

2.4 REGULATION OF CAPILLARY MATURITY

2.4.1 Endothelial barrier function

Vessel maturity is generally defined as maintaining endothelial barrier function, which is the tight regulation of transport across the endothelium. Maturity is conferred by the presence of intercellular tight and adherens junctions, a continuous BM, and varying degrees of pericyte coverage. Barrier function and angiogenic induction are typically anti-correlated with numerous cellular cues affecting both in opposing manners. Transport across the endothelium may either occur through the cytoplasm of ECs (transcellular) or through gaps between ECs (paracellular). Transcellular transport can occur passively by diffusion of lipophilic molecules, or through ATP-dependent vesicular or carrier mediated transport (54). Transcellular transport is largely regulated depending on cell type and receptor expression profile, whereas paracellular transport is regulated by the architecture of intercellular junctions (20). Extravasation of large molecules and blood cells typically occurs paracellularly (54). Paracellular barrier function is regulated through the formation of tight junctions and adherens junctions. Tight junctions between ECs are primarily formed by the protein families of claudins and occludins which mediate cell-cell

interactions and are most prevalent in maintaining the blood-brain barrier. Claudins are a large family of transmembrane proteins that are essential for tight junction formation. They seal paracellular gaps and form ion-specific channels that help regulate paracellular transport (20). Adherens junctions are more widely prevalent and in addition to helping control the flux of solutes they also function to link the cytoskeleton of neighboring ECs to maintain the structural integrity of vessels and control growth through contact inhibition. Homotypic interactions between the transmembrane protein family of cadherins mediate this interaction (22). Hemodynamic shear stress stimulates adherens junction formation and cytoskeletal remodeling, conferring enhanced barrier function (70). In addition to cell-cell junctions amongst ECs, endothelial interactions with the ECM and pericytes also help regulate barrier function (6).

2.4.2 Endothelial-matrix interactions affecting vessel maturity

Most mature quiescent blood vessels are coated in a continuous basement membrane rich in laminins, collagen-IV, perlecan, fibronectin, and nidogens (3). Knockdown of any of these BM proteins except nidogens results in embryonic lethality in mice and is correlated with vascular permeability (3). Laminin induces persistent Rac activity in ECs (71) which promotes vessel stability and adherens junction formation (72). Collagen-IV helps induce vessel quiescence by blocking matrix-metalloproteinase-2 (MMP-2) activity, and upregulating TIMP-2 expression (73). In general, intracellular signaling molecules associated with vessel maturity include protein kinase A (PKA), Epac, sphingosine-1-phosphate (S1P), and the small GTPases Rac-1 and cdc42 (54).

Focal adhesions are mediated by EC integrins binding to ECM proteins and play an important role in regulating barrier function. Typically, $\alpha_1\beta_1$ and $\alpha_2\beta_1$ bind to collagen, $\alpha_3\beta_1$, $\alpha_6\beta_1$, and $\alpha_6\beta_4$ bind to laminin, $\alpha_5\beta_1$ binds to fibronectin, and $\alpha_v\beta_3$ and $\alpha_v\beta_5$ bind to vitronectin

(54, 74). ECs invading fibrin clots initially express $\alpha_v\beta_3$ but lose expression as wounds become rich in collagen (75). Endothelial binding to BM proteins via integrins $\alpha_3\beta_1$ or $\alpha_5\beta_1$ induces a less permeable phenotype (76). Angiogenesis occurs much more rapidly in pure fibrin gels than in pure collagen-I *in vitro*, although a combination of both ECM proteins supported nearly the same degree of vessel formation as pure fibrin (77). Both ECM proteins are part of the provisional matrix ECs experience during wound healing and collagen-I is known to stimulate angiogenesis and Rho A activity through integrin signaling, disrupting adherens junction formation (71). The interstitial ECM within most tissues in the body is predominately collagen-I, and fibroblasts are the predominant source of collagen-I secretion. Integrin signaling between fibroblasts and collagen-I provides a negative feedback loop to reduce collagen synthesis when its availability is sufficiently high (78).

2.4.3 Endothelial-pericyte interactions affecting vessel maturity

Pericyte recruitment to EC vessels stimulates BM deposition which contributes to paracellular barrier function (44, 79). Leakiness in tumors is associated with an irregular pericyte coat and disorganized basement membrane deposition (80–82), highlighting the importance of pericytes in regulating normal vascular function. Direct ECs-pericyte interactions are largely mediated by heterotypic N-cadherin interactions, and loss of N-cadherin expression in either ECs or pericytes results in poor EC barrier function both in vitro (72) and in vivo (23). EC-pericyte interactions induce EC expression of TIMP-2 and pericyte expression of TIMP-3 contributing to endothelial tube stabilization. TIMP-2 and -3 inhibit MT1-MMP preventing morphogenesis and also provide cues preventing capillary tube regression (83).

Well-known pericyte markers include neural-glial antigen-2 (NG2), α-smooth muscle actin (α-SMA), desmin, and platelet derived growth factor receptor-β (PDGFRβ) (84–86), and

possibly lesser-used markers including calponin, (7) non-muscle myosin, tropomyosin, nestin, aminopeptidase A, aminopeptidase N (CD13), and sulfatide (80). Many of these markers are shared with other cell types including smooth muscle cells, as such, one of the more widely accepted indicators of pericyte identity in addition to biomolecular markers is co-embedment within the endothelial BM.

2.5 MODELS OF VASCULOGENESIS AND ANGIOGENESIS

In vitro models of capillary morphogenesis broadly fall into the categories of either vasculogenic or angiogenic (**Fig 2.2**). Capillary networks self-assemble from dispersed endothelial cells in vasculogenic models, whereas networks sprout from predefined nodes or confluent layers in angiogenic models (87). Early models of vasculogenesis demonstrated that endothelial cells seeded on a surface coated with adhesive proteins, or on top of gels made of collagen, fibrin, matrigel, or various synthetic substrates, self-assemble into a network of

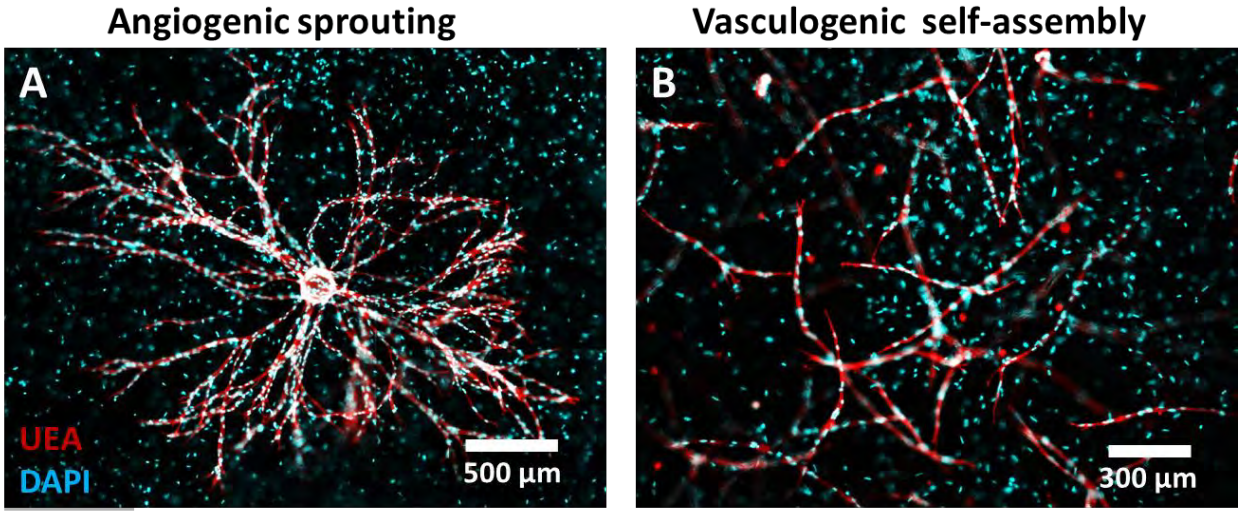

Figure 2.2: Examples of angiogenic and vasculogenic models used in this dissertation. (A) Endothelial cells (ECs) are coated on Cytodex microcarrier beads which here are embedded in a fibrin hydrogel with fibroblasts distributed throughout the matrix. Endothelial cells sprout away from the microcarrier creating a capillary like network. (B) ECs and fibroblasts are both distributed in the hydrogel and ECs self-assemble into a capillary like network. Ulex Europaeus Agglutinin I (UEA) is a fluorescently labeled lectin that preferentially binds ECs. 4′,6-diamidino-2-phenylindole (DAPI) stains all cellular nuclei. UEA-negative nuclei are presumed fibroblasts.

capillary like structures (87). In three dimensional models of vasculogenesis, endothelial cells are dispersed within various hydrogel matrices and typically require co-culture with a supportive stromal cell to form an interconnected capillary like network. Angiogenic models include sprouting from monolayers of endothelial cells into a hydrogel either from on top of a hydrogel (88) or from coated channels (89), and sprouting from predefined nodes such as aortic ring explants (90), spheroids (91), or from EC-coated microcarrier beads (92).

To date, most studies of capillary morphogenesis have been conducted in biologically derived scaffolds such as fibrin, collagen, Matrigel, and hyaluronic acid (93). Although biological scaffolds tend to support extensive capillary-network formation, they are difficult to precisely engineer and are typically derived from animal sources prompting concerns of batch-to-batch variation and immuno-rejection. These concerns with naturally derived scaffolds has driven interest in synthetic ECM scaffolds, which provide an attractive alternative for clinically translatable applications because of low-immunogenicity, tunable material properties, and industrial scalability (94). Within engineered hydrogel scaffolds, many endothelial cell types have demonstrated the capacity to undergo capillary morphogenesis, including human umbilical vein endothelial cells (HUVECs) (7), endothelial colony forming cells (ECFCs) (95), circulating endothelial progenitor cells (EPCs) (96), microvascular endothelial cells (MVECs) (97), and ECs derived from induced pluripotent stem cells (98). Similarly, numerous stromal cells have demonstrated a capacity for supporting vessel formation including multipotent cells from bone marrow (56, 99, 100), adipose tissue (10, 101, 102), and cord blood (100), a variety of fibroblasts (11, 52, 103, 104), and smooth muscle cells (53, 91, 105). There is little consensus, however, on the relative benefits of using certain cell types over others with very few studies directly comparing morphogenetic behavior depending on endothelial and stromal cell choices.

2.6 APPLICATIONS OF VASCULAR SELF-ASSEMBLY IN TISSUE ENGINEERING AND CARDIOVASCULAR DISEASE TREATMENT

Most tissues require a permeating dense and mature micro-vascular network to supply nutrients and remove waste for cell survival. A widespread hurdle in tissue engineering is the formation of this functional capillary network within implanted tissue constructs, necessary for their long-term viability. Techniques for stimulating the formation of this microvascular network broadly fall into the categories of either angiogenic ingrowth and vasculogenic self-assembly (40). Methods that support angiogenic ingrowth often rely on the release of proangiogenic growth factors such as VEGF to encourage vascularization (106–108). The formation of a vascular bed by angiogenic ingrowth results in the formation of an autologous capillary network, which circumvents the issue of implanting allogeneic cells that may elicit an immune response. Vasculogenic self-assembly relies on the delivery of an appropriate combination of ECs and stromal cell types that cooperatively interact to induce capillary morphogenesis. Vasculogenic strategies are convenient for rapid formation of a capillary bed. Implantation of acellular hydrogels without pro-angiogenic growth factors often results in little to no vascularization (11, 106, 109). Vasculogenic strategies, however, are still generally believed to require some degree of angiogenic invasion for the implant to become perfused (95), resulting in chimeric vessels (110).

Vascularization strategies are widely relevant for many tissue engineering applications including revascularizing ischemic tissues, pre-vascularizing tissues for implantation, and *in vitro* organoid models. There are emerging techniques for fabricating larger tissue constructs with vascular conduits on the 100 μm-mm scale (111, 112) allowing for arteriole scale networks. Implantation of a biomaterial with 3D printed arteriole scale conduits (113) or the injection of

biomaterials that support micro-vessel network formation inducing collateral blood flow (114, 115) are potential treatment alternatives to autologous or synthetic grafts for arterial bypass surgery (116). Intelligent scaffold design is additionally relevant for the fabrication of tissue-engineered vascular grafts that facilitate the formation of *vasa vasorum* to enhance graft viability (117). Biomaterials that promote capillary morphogenesis without macro-scale conduits also present a possible treatment of occluded blood vessels and ischemic pathologies by rapidly vascularizing and inosculating with host vasculature to provide collateral blood-flow to bypass occluded regions (115, 118).

Clinically, there is immediate applicability towards vascularization of a variety of tissues for implantation including bone grafts to treat bone defects (119, 120) and therapeutic organoids that secrete designated biomolecules to replace or supplement patient deficiencies in endocrine or immune function (121, 122). Treatment of type 1 diabetes by transplanting pancreatic islets in a scaffold to secrete insulin is a well-studied example near clinical translatability (122). Recently, significant effort has been invested in vascularizing these therapeutic organoid constructs to improve their efficacy, including a PEG-based composite of immuno-isolating and angiogenic scaffold materials (123). Moreover, recapitulating cellular cross talk between parenchymal and vascular tissues *in* vitro is essential for accurately constructing tissue models in which the parenchyma and endothelium are intimately linked, such as in models of the liver (124), kidney (125), and pancreas (126) to study pathological conditions.

2.7 POLY(ETHYLENE GLYCOL) HYDROGEL DESIGN

Synthetic ECM scaffolds provide an attractive alternative to natural ECM scaffolds for clinically translatable applications because of low-immunogenicity, tunable material properties, and industrial scalability (94). Amongst synthetic scaffolds, proteolytically degradable poly (ethylene

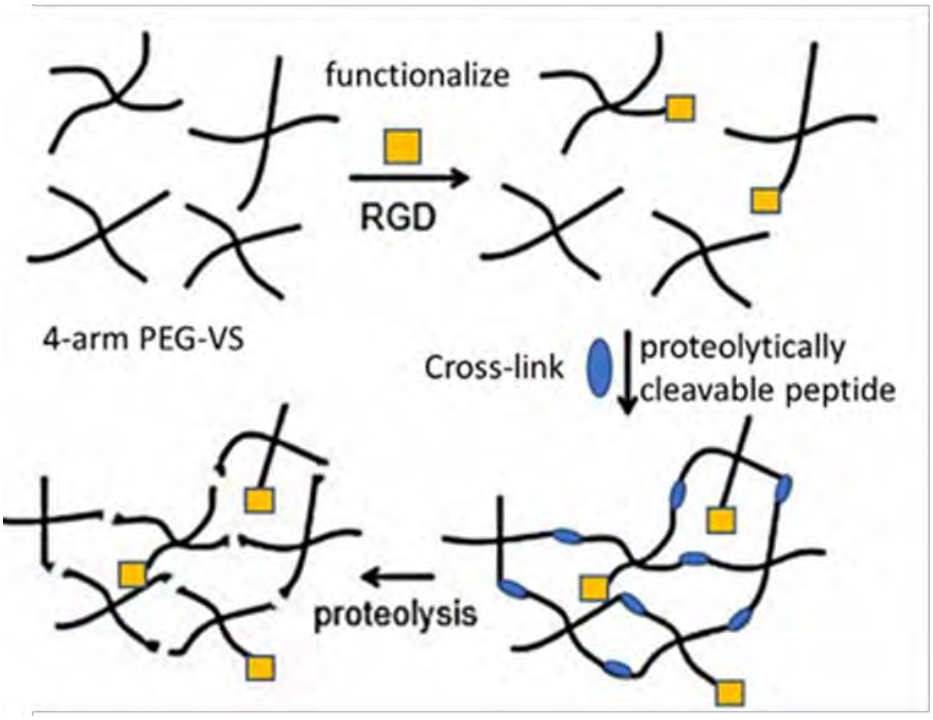

Figure 2.3: Reaction scheme for formation of PEG-hydrogels via Michael-type addition. Hydrogels used in this work were formed by the conjugation of free cysteines on peptides to vinyl-sulfone groups on 4-arm PEG molecules via a Michael-type addition reaction. First, RGD is conjugated to PEG to functionalize the hydrogels for cellular adhesion. The hydrogels are then crosslinked with a proteolytically labile dithiol containing peptide to form a hydrogel. Embedded cells can then remodel this matrix via proteolysis during morphogenetic processes.

glycol) (PEG)-based hydrogel scaffolds have garnished particular interest because of their biocompatibility and versatile macromer chemistry allowing tunable hydrogel design (94). The PEG-based hydrogels used in this dissertation are formed via a Michael-type nucleophilic addition reaction between vinyl sulfone groups on 4-arm PEG molecules (20kDa), and thiol groups on terminal cysteine residues of varying peptides (**Fig 2.3**) (114, 127, 128). Peptide crosslinks are proteolytically degradable and can be varied to modulate the rate and specificity of degradation without affecting other material properties (128–130). Scaffolds also contain a short integrin binding peptide, RGD, which binds numerous integrins and allows for cell adhesion (74). Like crosslinks, the identity and concentration of adhesive ligand can be titrated independent of other hydrogel material properties.

Despite wide-spread interest in PEG-based scaffolds for regenerative medicine applications, and various strategies for improving vascularization (106–108), capillary morphogenesis remains highly restricted within these scaffolds compared to those derived from natural ECM (**Fig 2.4**), and significant work remains to characterize how vascular self-assembly occurs in these materials. The nano-scale amorphous architecture of PEG-based hydrogels rather than micro-scale fibrous architecture of most natural ECMs results in differences in cellular morphogenesis. There are differences in integrin mediated signaling, mechanical cues from the matrix, diffusive transport, and cell migration (129). Key design parameters of PEG hydrogels that have been shown to influence capillary morphogenesis include the specificity (131, 132) and susceptibility (89, 91) to proteolytic degradation, degree of crosslinking (131, 133), their mechanical properties (134), and the presentation of growth factors (107, 108, 121, 123).

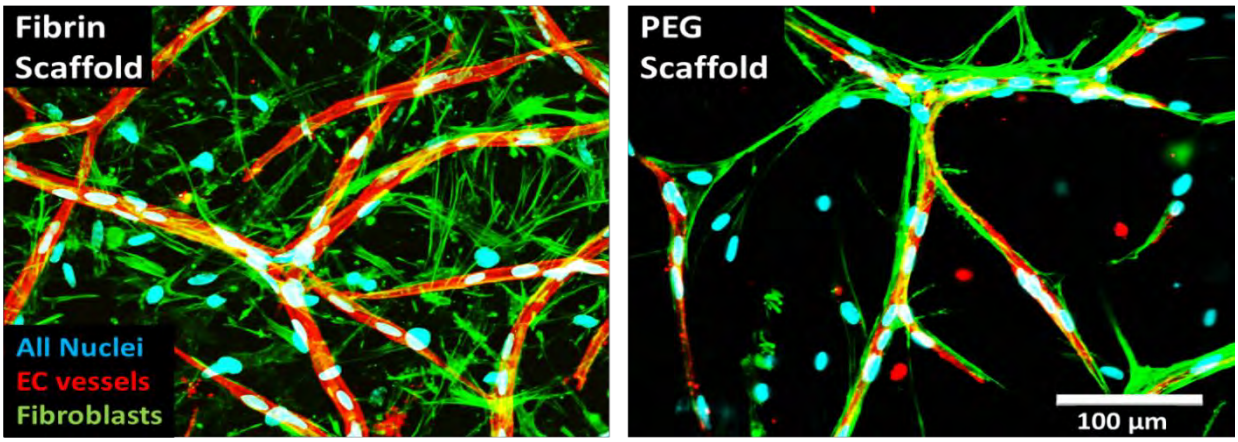

Figure 2.4: Endothelial network formation and overall cell spreading are restricted in PEG-hydrogels compared to fibrin. Representative images of EC-DF co-cultures after 7 days in either 2.5 mg/ml fibrin or 27 mg/ml PEG are shown. EC vessels are shown in red stained with UEA, all cellular nuclei are shown in cyan stained with DAPI, and all cell bodies are stained in green with phalloidin. UEA-negative cell-bodies are presumed fibroblasts.

2.8 PREVIOUS WORK COMPARING FIBROBLASTS AND MSCS AS SUPPORTIVE STROMAL CELLS

Comparative studies in which cellular identity and ECM properties are systematically varied help illuminate the relative strengths and weaknesses of various culture models. Our lab

has previously demonstrated that varying the stromal support cell in fibrin hydrogels between fibroblasts and bone marrow mesenchymal stem cells (MSCs) results in vessels with varying quality. Fibroblasts stimulate more rapid vessel formation than MSCs and these vessels are more permeable both *in vitro* (10) and *in vivo* (11). Barrier function in the presence of either stromal cell type improves over time *in vitro,* however, at all time points vessels are more permeable when cultured with fibroblasts (10).

MSCs are generally believed to act as pericytes (135, 136) and endothelial cells have been shown to stimulate recruitment and differentiation of multipotent mesenchymal cells into mural lineages such as smooth muscle cells and pericytes (137). Pericyte recruitment is an essential step in stimulating BM formation and in stabilizing nascent vessels (44). Whether fibroblasts can act as pericytes however, is less well known. Our group and others have seen fibroblasts associate with vessels in a pericyte like manner (103, 118). Fibroblast-secreted ECM proteins have been shown to enhance EC vessel formation (52, 138), and fibroblasts are also known to stimulate cutaneous (139–141) and pulmonary (142) BM deposition and decrease paracellular permeability in lumenized epithelial spheroids (143). We have also seen that both MSCs and fibroblasts express α-SMA in our fibrin based angiogenesis assays but only MSCs express NG2 (7), suggesting MSCs are more capable of acting as pericytes. EC-pericyte crosstalk through NG2 helps stimulate vessel maturity through a β_1 integrin dependent pathway (144). Our group and others have reported enhanced cadherin expression in the presence of MSCs over fibroblasts (10, 72), also suggesting their enhanced capacity to act as pericytes. Moreover, MSCs have the capacity to differentiate into a variety of stromal and mural lineages (135, 136) which may be essential for maintaining vessel functionality. Differentiation of MSCs (145) and trans-differentiation of mural cells (146) into fibroblast phenotypes are well known

physiological processes, however the converse is not typically known to occur. Dermal fibroblasts are only known to dedifferentiate into a more pluripotent MSC phenotype when treated with embryonic cell extract (147), and adventitial fibroblasts may convert into medial smooth muscle cells during vascular regeneration (148), but physiological dedifferentiation of fibroblasts into MSCs in adult cells has not been reported.

In addition to differences in pericytic capacity depending on stromal cell identity there are also differences in secretory profiles. Fibroblasts, unlike MSCs, upregulate tumor necrosis factor α (TNFα) and hepatocyte growth factor (HGF) in the presence of HUVECs (101), suggesting an inflammatory wound healing response may also contribute to enhanced angiogenesis in the presence of fibroblasts. Myofibroblast differentiation has been associated with HGF upregulation (149). In wound healing environments, fibroblasts are known to differentiate into myofibroblasts and increase pro-angiogenic cytokine secretion, ECM deposition, and increase contractility, which contributes to a proangiogenic response (150–152). Although α-SMA expression is often associated with pericyte association, it can also be indicative of myofibroblastic differentiation, of which both cell types are capable in a wound healing environment (150, 153).

Our lab has previously demonstrated that fibroblast-mediated sprouting in fibrin is less susceptible to MMP inhibition than MSC-mediated sprouting unless serine-proteases are additionally inhibited (7). This effect may be mediated either by enhanced serine-protease activation of MMPs in fibroblast co-cultures offsetting MMP inhibition, or through a direct fibrinolytic contribution of serine-proteases mitigating deficiencies in MMP-mediated ECM degradation (7). Plasmin is a key serine-protease implicated in both fibrinolysis (154) as well as activation of numerous MMPs (5, 9). HUVECs upregulate the expression of urokinase

plasminogen activator (uPA) in the presence of fibroblasts but not MSCs (101), and fibroblasts express uPA at a much higher level than MSCs in general (7), implicating the role of plasmin in stimulating enhanced fibroblast-mediated invasiveness. Whether plasmin-mediated fibrinolysis contributes to angiogenic invasion, however, remains debatable (8, 12, 59, 62).

Within this thesis I have largely characterized the morphogenetic behavior of endothelial cells in the presence of dermal fibroblasts (DFs), with some comparison to lung fibroblasts (LFs) and MSCs. Much of our lab's previous work has used LFs, however, DFs are more translationally relevant in that they can be easily obtained autologously (155) without the invasive bronchoscopy required to obtain LFs (156). Autologously obtaining MSCs is similarly invasive, requiring bone-marrow aspiration (157), with the added difficulty of expanding MSCs while maintaining their pluripotent phenotype (158). Characterizing endothelial morphogenesis in the presence of DFs provides insight into their morphogenetic behavior while facilitating vascularization of engineered tissue constructs. Furthermore, comparison of potential stromal cell sources in supporting capillary morphogenesis demonstrates cell-dependent differences, which helps inform the rational choice of supportive stromal cells depending on the specified application.

CHAPTER III

Sprouting Angiogenesis Induces Significant Mechanical Heterogeneities And ECM Stiffening Across Length Scales In Fibrin Hydrogels

3.1 ABSTRACT

Matrix stiffness is a well-established instructive cue in two-dimensional cell cultures. Its roles in morphogenesis in 3-dimensional (3D) cultures, and the converse effects of cells on the mechanics of their surrounding microenvironment, have been more elusive given the absence of suitable methods to quantify stiffness on a length-scale relevant for individual cell-extracellular matrix (ECM) interactions. In this study, we applied traditional bulk rheology and laser tweezers-based active microrheology to probe mechanics across length scales during the complex multicellular process of capillary morphogenesis in 3D, and further characterized the relative contributions of neovessels and supportive stromal cells to dynamic changes in stiffness over time. Our data show local ECM stiffness was highly heterogeneous around sprouting capillaries, and the variation progressively increased with time. Both endothelial cells and stromal support cells progressively stiffened the ECM, with the changes in bulk properties dominated by the latter. Interestingly, regions with high micro-stiffness did not necessarily correlate with remodeled regions of high ECM density as shown by confocal reflectance microscopy. Collectively, these findings, especially the large spatiotemporal variations in local stiffness around cells during morphogenesis in soft 3D fibrin gels, underscore that characterizing ECM mechanics across length scales provides an opportunity to attain a deeper mechanobiological understanding of the microenvironment's roles in cell fate and tissue patterning.

3.2 INTRODUCTION

Numerous cell types demonstrate differential phenotypic responses and differentiation potential depending on the elasticity of the environment in which they reside (159). Tuning substrate rigidity in 2D, ostensibly without altering porosity, diffusive transport, or ligand density, alters cell spreading (160, 161), proliferation (162, 163), migration (161, 164), and differentiation (165, 166). Despite the interdependence of elasticity with other properties in real tissues, ECM mechanical properties also appear to control cell fate in 3D (167, 168). Nevertheless, despite considerable interest in the effects of matrix rigidity on cell phenotypes, how cells change the mechanical properties of the surrounding ECM, particularly on a microscale, remains poorly understood. Moreover, the instructive cue of matrix stiffness has largely been treated as unidirectional and static, with measurements of bulk stiffness at a singular initial time point correlated with cell fate. In reality, complex morphogenetic processes in 3D involve dynamic and reciprocal mechanical cross-talk between cells and the surrounding ECM.

ECM stiffness has also been postulated to be an important instructive cue governing capillary morphogenesis (169), affecting the magnitudes of contractile forces endothelial cells (ECs) exert on their surroundings to control their invasive abilities (170). We have previously shown that EC contractile forces are essential for capillary morphogenesis (171), and the rate at which ECs deform ECM fibers depends on the initial matrix concentration and correlates with the rate at which they form vessel-like structures in 3D (64). However, different material platforms and cross-linking schemes have led to discrepancies in the literature, with some studies suggesting softer matrices are more supportive of vascular morphogenesis and others reporting higher stiffness yields more invasion. Regardless, across all material platforms, the spatiotemporal evolution of ECM micromechanics during angiogenic sprouting remains unclear.

In this study, we exploited a well characterized model of angiogenic sprouting in which ECs coated on microcarrier beads invade a 3D fibrin matrix when co-cultured with stromal fibroblasts (92, 172). Fibrin is the major component of the provisional matrix in a blood clot (173), and thus is a suitable model for investigating the mechanical evolution of ECM during wound healing. Fibroblasts secrete pro-angiogenic cytokines and other factors that are essential for EC tubulogenesis when co-embedded with ECs in the fibrin matrix, where they can act in a pericyte-like manner and directly associate with the nascent capillaries (7), or overlaid on top of the gels as a monolayer (52, 104). In addition to supporting angiogenesis, fibroblasts play important roles in wound closure and healing by increasing contractility and depositing ECM (174), both of which effect the elasticity of the matrix (52, 175).

Through a combination of shear rheology to track bulk elastic properties and laser-based optical tweezers active microrheology (AMR) to quantify elasticity on a length scale relevant for individual cells, we explicitly quantified changes in ECM mechanics across length scales, over time, and with unprecedented resolution during the complex morphogenetic process of angiogenic sprouting *in vitro*. Our findings reveal significant mechanical heterogeneities encountered by cells on the microscale and demonstrate the extent to which the ECs themselves alter the mechanical properties of the surrounding ECM. We further assessed whether pericytic association affects the rate and degree to which local ECM stiffening occurs, and determined the effect fibroblasts have on the ECM when distant from sprouting microvasculature. Collectively, this study highlights the importance of characterizing ECM mechanical properties on an appropriate length scale and over time, as initial bulk characterization misses the dynamic and highly varied environment individual cells experience.

3.3 MATERIALS AND METHODS

3.3.1 Cell culture:

Normal human dermal fibroblasts (DFs, Lonza, Walkersville, MD) were cultured in Dulbecco's modified eagle medium (DMEM, Life Technologies, Grand Island, NY) supplemented with 10% fetal bovine serum (FBS, Life Technologies) and 1% penicillin streptomycin (Life Technologies) and were used up to passage 7. Human umbilical vein endothelial cells (ECs) were either harvested from fresh umbilical cords as previously described (172) or purchased from a commercial source (Lonza). Two different sources of ECs were used to ensure robustness of the observed biological responses. The ability of these two different sources of HUVECs to sprout in our fibrin-based assays was quantitatively equivalent (data not shown). HUVECs for all experiments were cultured in fully supplemented EGM2 (Lonza) and used between passages 2-4. Media for both cell types were exchanged 3 times a week and cells were harvested below 80% confluence using 0.05% trypsin-EDTA (Life Technologies).

3.3.2 Fibrin-based capillary morphogenesis assay:

A three-dimensional cell culture model of capillary morphogenesis was assembled following adapted protocols as previously described (92, 172, 176). Briefly, EC-coated microbeads were embedded in fibrin gels with DFs either embedded or overlaid on the gel as a monolayer. A stock solution of sterilized Cytodex microcarrier beads (Sigma-Aldrich, St Louis, MO) was prepared ahead of time by autoclaving in PBS. The day before construct assembly, microbeads were coated with ECs by combining $1x10^4$ microbeads with $4x10^6$ ECs in 5 mL of EGM2 in an upright T-25 tissue culture flask (Corning Inc, Corning, NY). The flask was incubated for 4 hours with periodic agitation every 30 minutes. Afterwards, 5 mL of fresh EGM2 was added, and the 10 mL suspension of freshly coated beads was transferred to a new T-25 and allowed to incubate

overnight in the standard tissue culture position. The following day, beads were transferred to a 15 mL conical tube (VWR, Radnor, PA) and allowed to settle by gravity between two washes with fresh EGM2. Fibrinogen from bovine plasma (Sigma) was dissolved in serum free EGM2 to achieve a final concentration of 2.5 mg/mL clottable fibrinogen upon gelation, and sterile filtered through a 0.22 μm PES membrane filter (Merck Millipore Ltd, Tullagreen, Carrigtwohill, Co. Cork, IRL). For conditions in which the stromal fibroblasts were embedded within the fibrin gel ("embedded") a suspension of DFs was added to the fibrinogen at a final concentration of $2.5x10^4$ cells/mL; for the other conditions, an equal volume of EGM2 was added instead. Microbeads were added to the solution at 50 beads/mL. Heat-inactivated FBS was added to the solution immediately prior to gelation for a final concentration of 5%. Tissue culture dishes were spotted with 40 μL of 100 U/mL thrombin reconstituted in ddH_2O per mL fibrinogen. Dishes were allowed to sit for 5-minutes before being transferred to incubate at 37 °C for another 25 minutes to allow for complete gelation. After gelation, 2 mL of EGM2 per 1 mL of fibrin gel was overlaid for all gels. For conditions in which the stromal fibroblasts were cultured on top of the gel ("overlay"), DFs were introduced in the overlaid EGM2 at a concentration of $2.5x10^4$ cells/mL of fibrin gel to achieve equal DF numbers per gel for both overlay and embedded conditions. For each independent experiment, multiple gels were cast for each time point. Gel constructs (0.5 mL total volume) were fabricated in 24-well tissue culture plates (Corning Inc) for bulk rheology and network quantification assays. For micro-rheology and reflection confocal imaging, gel constructs (1 mL total volume) were fabricated in 35 mm glass bottom dishes (MatTek, Ashland, MA).

For experiments involving Transwell inserts, fibrin based gel constructs (2 mL total volume) were fabricated in the bottom chamber of 6-well Transwell plates (24 mm diameter inserts containing 3.0 μm pores; Corning). DFs were cultured on top of the insert, and DAPI staining was

used to confirm these cells did not migrate through the porous insert to the gel surface during the assay. Because the bottom of the insert would rest on the gel if used as provided, sterilized silicon O-rings (MSC, Melville, NY, part # S70-028) were used to space the insert off the top of the gel. All tissue constructs were cultured for up to two weeks with media exchanged on day 1 and every two days thereafter.

3.3.3 Fluorescent imaging and quantification of capillary morphogenesis:

Images were acquired using an Olympus IX81 confocal microscope equipped with a USH-103OL mercury lamp (Olympus America, Center Valley, PA), a Hamamatsu Orca II CCD camera (Hamamatsu Photonics, Hamamatsu City, Japan), and Metamorph Premier software (Molecular Devices, Sunnyvale, CA). For visualization of tubules and cell nuclei, co-cultures were fixed with Z-Fix aqueous buffered zinc formalin fixative (Anatech, Battle Creek, MI) and stained with a rhodamine-conjugated lectin from *Ulex europaeus* (UEA, Vector Laboratories, Burlingame, CA) and 4',6-diamidino-2-phenylindol (DAPI, Sigma-Aldrich). UEA binds glycoproteins and glycolipids specific to endothelial cells. UEA- and DAPI-stained samples were acquired using red (Ex: 562 nm, bandwidth: 40 nm; Em: 641 nm, bandwidth: 75 nm) and blue (Ex: 377 nm, bandwidth: 50 nm; Em: 477 nm, bandwidth: 60 nm) filter sets, respectively. Network length was quantified at days 1, 4, 7, and 14 with all beads imaged at 4x magnification. On day 14, multiple images often had to be stitched together to fit the entire network from a single bead. For unbiased measurements, the microscope was rastered through each gel and all beads were imaged that were far enough away from the edge of plate such that sprouting was unimpinged and did not have overlapping networks with a neighboring bead. This resulted in 8-40 beads per condition for each independent experiment being quantified, with diminishing beads meeting the criteria as time progressed. Three independent experiments (N=3) were conducted for each condition and time

point, and the aggregate data from all beads across all 3 independent experiments were presented to illustrate the spread in biological response. Total tube length per bead was quantified using the Angiogenesis Tube Formation module in Metamorph. The average network length per bead for each condition of each independent experiment was then used for statistical analysis. DF proliferation in overlay conditions was quantified by taking DAPI images of the DFs in a monolayer on top of the gel and manually determining cell density.

3.3.4 Bulk rheology:

The bulk mechanical properties of fibrin-based constructs were measured via parallel plate shear rheology using an AR-G2 rheometer (TA Instruments, New Castle, DE) equipped with an 8 mm diameter measurement head and a Peltier stage. Oscillatory shear measurements of 6% strain amplitude and a frequency of 1 rad/sec were performed on days 1, 4, 7, and 14 directly in multi-well tissue culture plates with the rheometer stage maintained at 37 °C. Cell culture media were aspirated before measurements, with a small volume left to ensure the gel remained wet. Rheology of elastic pre-swollen hydrogels typically involves application of a small normal force prior to data acquisition, and/or use of a consistent gap width between the bottom of the sample and the platen. However, fibrin's viscoelasticity precludes use of the former method, while varying degrees of cell-mediated gel compaction over time preclude the latter. Instead, a protocol was developed whereby the top platen was lowered until it made initial contact with the hydrogel, followed by measurements of shear modulus (G') taken at 200 μm intervals while closing the gap between platen and stage. Gels exhibited a plateau in G' as the gap was progressively decreased after making contact with the gel (**Supplementary, Fig 3.6A, B**). The peak G' measured of 3 gap heights after making contact with the gel was used as our reported value for the given region of interest. One region of interest was interrogated per gel in 24-well plates, and three regions of

interest were interrogated per gel in 6-well plates. The measurement head was carefully centered in 24-well plates to avoid edge effects contributing to G' measurements. Comparisons between acellular gels in 24 and 6-well plates over time (2.5 cm^2 and 9.8 cm^2 areas, respectively) were used to confirm the robustness of the methods across gels of different sizes (**Supplementary, Fig. 3.6C**). Overlay cultures in 6-well plates were also tracked over 14 days to ensure well size did not influence observed stiffening behavior (**Supplementary, Fig 3.7**). Overlay and embedded conditions with AMR beads included were also tested to ensure bulk G' was unaffected by their inclusion (**Supplementary, Fig 3.8**). At least 3 measurements were taken per time point per independent experiment. Three independent experiments were conducted (N=3) and for each independent experiment, the gels for all time points were cast from the same stock of reagents.

3.3.5 Laser tweezers-based Active Microrheology:

Active microrheology (AMR) was conducted using a dual-laser optical tweezers system, as has been previously described (177) and used in the study of capillary morphogenesis (64). Briefly, fibrin hydrogels were polymerized as described above within 35 mm glass bottom dishes (MatTek, Ashland, MA) with a dispersion of 2 μm carboxylated silica microbeads (Bangs Laboratories, Fishers, IN) at a concentration of 0.08% (w/v) throughout the hydrogel. During AMR measurements, beads within a volume of approximately 250 x 175 x 30 μm are oscillated at 50 Hz by optical forces induced by a focused 1064 nm laser (trapping beam), at an amplitude of 175 nm. A stationary 785 nm laser (detection beam) was used to detect each probe particle movement in response to the driving force. The oscillation of the input trapping beam and the deflection of the detection beam by the microbead are recorded by a pair of quadrant photodiodes (Newport, Irvine, CA). These measurements allow for calculation of the complex material response α^*. Data here is presented as the real component (G') of the complex shear modulus G^*, computed from α^*, as

previously done (178, 179). AMR measurements were performed on days 1, 4, 7, and 14 (N=3, per day, per condition) within a custom-built stage top incubator. The volume measured within each measurement location within cell-free samples was chosen randomly, while measurements within capillary morphogenesis assays were chosen to be localized around the sprouting endothelial cells or proximal to Cytodex beads on day 1.

3.3.6 Confocal Reflection Microscopy:

Reflection confocal stacks were acquired prior to AMR measurement of each sample. Confocal microscopy was conducted using a Fluoview 1200 system (Olympus), integrated into the optical tweezers microscope. Image stacks were imaged using the 488 nm laser line with a depth of approximately 60 μm and step size of 1 μm. For z-projections, stacks were trimmed to remove effect of glass aberration in reflection confocal and in order to keep a consistent number of planes for each z projection. Images were acquired using the same objective as for AMR; 1.45NA 60X TIRF Oil Objective (Olympus).

3.3.7 Statistics:

Varying statistical methods were performed depending on the nature of the data analyzed and are indicated as appropriate on the figure captions. For analyzing network length, the average sprout length per bead from 8-40 beads per time point per replicate was considered for statistical analysis in comparing conditions. Linear regression was used for analyzing network length data for embedded and overlay conditions. For analyzing bulk rheology data, the average bulk modulus from 3-6 ROIs per time point per replicate was considered in comparing conditions. Heteroscedastic 2-tail t-tests were used to verify overlay and Transwell conditions had equitable sprouting on any given day, that AMR beads do not influence bulk G' or sprouting, and that culture well size does not influence bulk-G'. One-way ANOVA was used to determine differences in bulk

mechanical properties and followed with Tukey HSD post-hoc testing if differences were detected. Mann-Whitney U tests with a Bonferroni correction were performed between pairs of aggregate AMR data.

3.4 RESULTS

3.4.1 DFs stimulate EC neovessel formation when overlaid or embedded in fibrin matrices:

ECs cultured on microcarrier beads embedded in fibrin gels of physiological concentration (180) undergo a complex 3D morphogenetic program that results in vessel-like structures radiating from the microcarrier bead when co-cultured with a variety of stromal cells (7, 92, 101). Here we demonstrate that normal human dermal fibroblasts (DFs), a clinically relevant and potentially autologous cell source, similarly support angiogenic outgrowth of ECs from microcarrier beads. DFs were either embedded or overlaid on the fibrin matrix to better elucidate the relative contributions of DFs versus EC tubules on the micro- and macro-rheological properties of the gel. Cartoon schematics of these two culture models are shown (**Fig. 3.1A**), along with representative images of the typical morphogenetic progression for both culture models (**Fig. 3.1B**). (Day 1 images reveal approximately comparable levels of EC confluence on the Cytodex beads achieved via the methods described.) Quantification of these types of images over a 14-day time course reveals an increase in the total length of the vessel-like networks for both conditions, with aggregate data from all beads across each independent experiment shown to illustrate the spread in the observed biological response (**Fig. 3.1C**). The average total network lengths for the embedded culture model were consistently higher than the overlay model after day 1, but this increase was not statistically significant. Additionally, inclusion of AMR beads did not affect the rate of network formation (**Supplementary, Fig 3.9**). Over the duration of the culture period, the

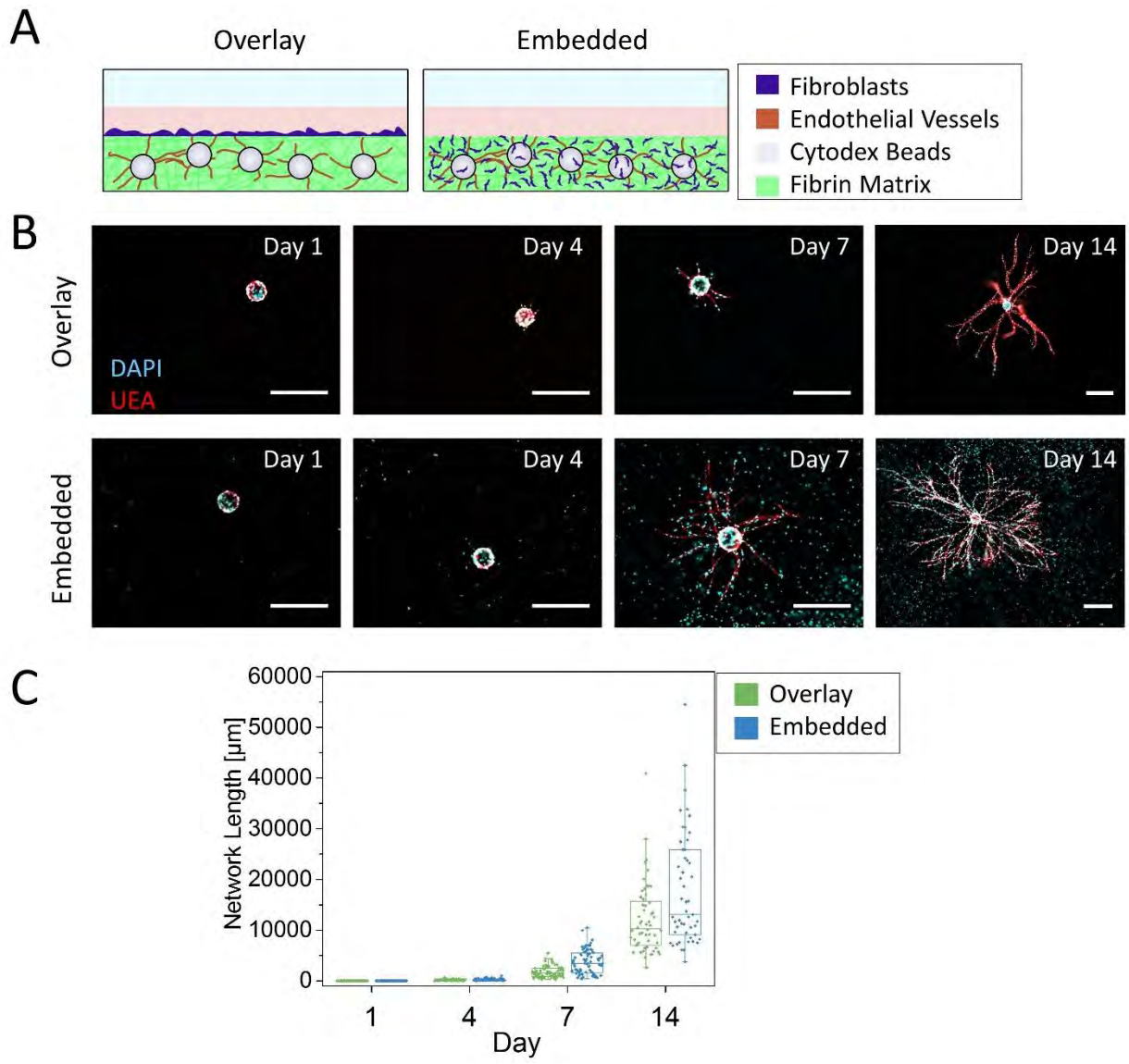

Figure 3.1: DFs induce EC branching morphogenesis when overlaid or embedded within 3D fibrin matrices. **A)** Schematic representation of the capillary morphogenesis assay. The "Overlay" condition involves culturing DFs on top of the fibrin gel, while the DFs are distributed throughout the fibrin gel in the "Embedded" condition. **B)** Representative images from each condition over a 14 day time course. UEA and DAPI staining indicate ECs and total cell nuclei, respectively. Scale bar = 500 µm. **C)** Quantified network lengths vs. time for both Overlay and Embedded conditions (8-40 beads assessed per replicate, N=3 per condition, per time point). A general linear model resulted in Log(Network Length) = 3.776*Log(Day), $p < 0.0001$, $R^2 = 0.988$. Boxed regions show median and interquartile range (IQR) of aggregate data, whiskers show range within 1.5 IQR.

average network length per bead scaled across multiple orders of magnitude with the variance scaling accordingly. Data were log transformed and analyzed with a general linear model. The resulting model is: Log(Network Length) = 3.776*Log(Day). The single regression parameter is

highly significant with $p < 0.0001$ and the model has an R^2 value of 0.988, demonstrating that vessel growth was exponential in time.

3.4.2 Acellular fibrin gels are mechanically stable over 14 days as assessed by macro-rheology and AMR:

To characterize the bulk rheological properties of both acellular (pre-swollen) and cell-seeded fibrin constructs, we devised a new method described in the *Supplemental Materials and Methods.* Cartoon schematics illustrating the relative scale of bulk rheology compared to AMR are presented in **Fig 3.2A** to illustrate the large difference in resolution between the two techniques. Bulk rheology showed acellular fibrin gels are mechanically stable, maintaining a nearly constant (time-invariant) G' of 119 ± 19 Pa (mean + st. dev. from all trials and days) over the course of the culture period. Moreover, the inclusion of Cytodex (**Fig 3.2B**) and/or AMR beads (**Supplementary, Fig 3.9**) did not influence the bulk properties of the gel. Additionally, agreement between G' measurements of gels cast in multiple well sizes illustrates the validity of the method developed, independent of gel size (**Supplementary, Fig 3.6**). Moving forward, we have used G' (the elastic component of the shear modulus) interchangeably with the more colloquial term "stiffness."

AMR measurements of acellular fibrin gels, both with and without Cytodex beads, exhibited notable stiffness heterogeneity spanning nearly two orders of magnitude (**Fig 3.2C;** min value of 8 Pa, max value of 933 Pa across all conditions and time points shown on the graph). Repeatedly, the mean stiffness of these cell-free systems was slightly higher at Day 1, as compared to Days 4, 7, and 14 ($p<0.05$, for both +/- Cytodex beads). However, comparisons of local G' values across the later time points were not statistically different from one another, illustrating the mechanical stability of these acellular fibrin gels at the microscale consistent with bulk rheology.

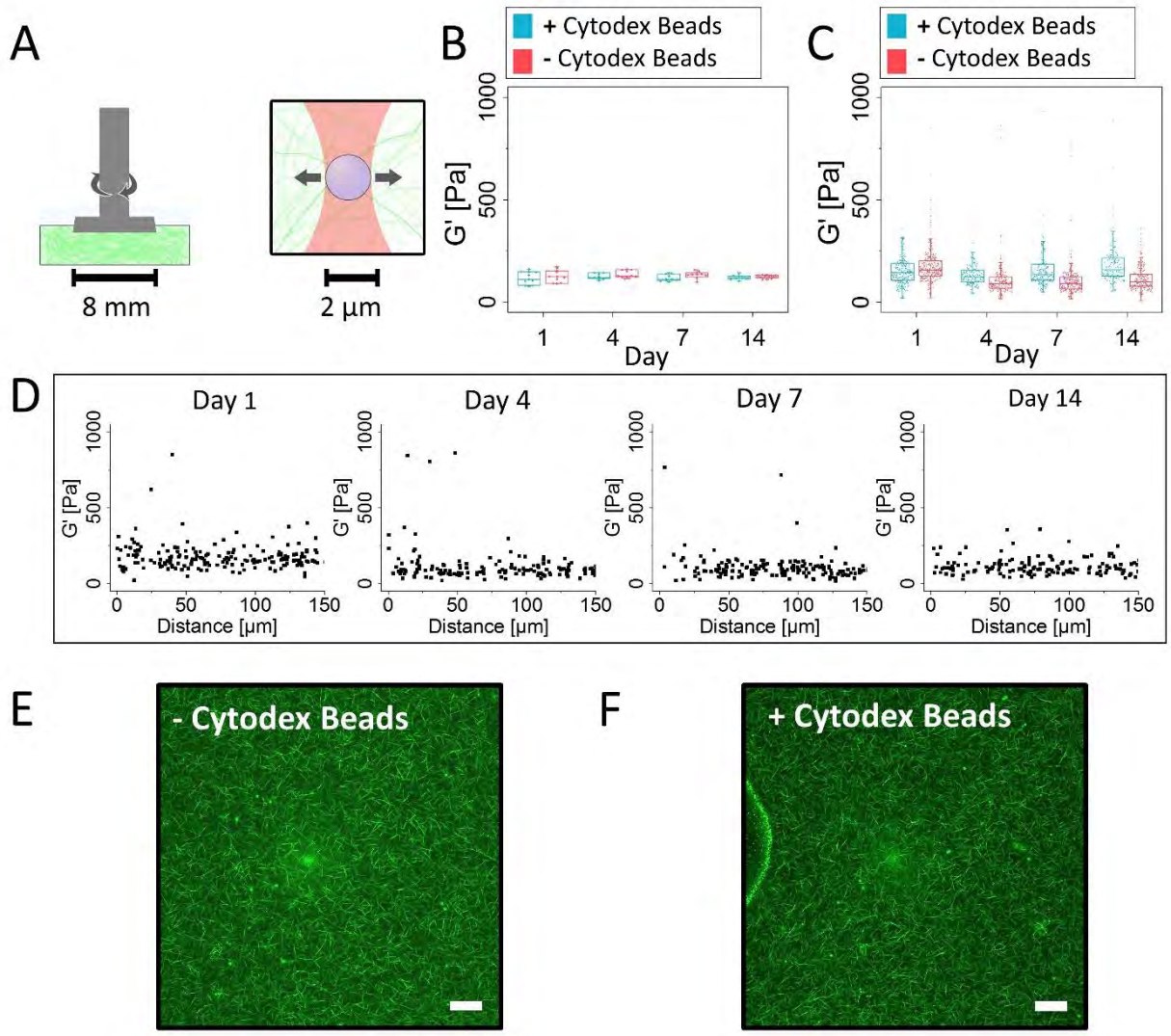

Figure 3.2: **Bulk rheology and AMR of acellular fibrin gels reveal the gels are mechanically stable over 2 weeks in culture conditions**. **A)** Schematic diagram of methods used to quantify stiffness in bulk using parallel plate rheology (left) and at the microscale using active microrheology (right). **B)** Bulk rheology over 14 days with (red) and without (blue) Cytodex beads. (N=3, per condition, per timepoint). One-way ANOVA of G' +/- Cytodex beads yielded a P value of 0.93. **C)** Microrheology over 14 days with and without Cytodex beads (aggregate data, N=3 independent samples, with $n_{AMRbeads}$>150 per time point, per condition). Boxed regions in panels B and C show median and interquartile range (IQR) of aggregate data, whiskers show range within 1.5 IQR. The asterisk above Day 1 indicates significant differences ($p<0.05$) relative to all other time points for both conditions (+/- Cytodex beads). **D)** Microrheology data from **(C)** plotted as a function of distance from the edge of the Cytodex bead. **E,F)** Confocal reflection of the fibrin meshwork without and with Cytodex beads (Scale bar = 20 µm).

Furthermore, the presence of the Cytodex beads did not appreciably affect the distribution of local stiffness, as demonstrated by plotting G' values at increasing distance from the Cytodex beads (**Fig 3.2D)**. Additionally, confocal reflection images near Cytodex beads were indistinguishable from gels without cytodex beads, illustrating that Cytodex beads do not disrupt the fibrillar architecture (**Fig 3.2E, F**).

3.4.3 Bulk rheology reveals tissue constructs stiffen over time during morphogenesis:

Fibrin gels with DFs either overlaid or embedded demonstrated significant stiffening over time, with overlay conditions stiffening more rapidly than embedded conditions (**Fig 3.3A**). Controls in which DFs were included but Cytodex microcarrier beads were not coated with ECs demonstrate similar bulk stiffening behavior over time (**Fig 3.3B**). Scaffolds with DFs embedded stiffened ~2-fold to a final G' of 253 ± 27 Pa, while scaffolds with DFs overlaid stiffened ~3.3-fold to a final G' of ~394 ± 43 Pa over the course of 2 weeks. Heteroscedastic 2-tail t-tests were used to verify no significant differences occurred between G' measured for any given culture model and day compared to its respective *DF Only* control (**Fig 3.3A, 3.3B**). In addition, experiments in which DFs were cultured on Transwell inserts, and then removed for gel rheological measurements, showed that construct mechanical properties did not significantly change over a 14-day time course in the absence of DFs, even when ECs were included in the culture and tubulogenesis occurred (**Fig. 3.3C**). Lack of contact of the DFs with the fibrin construct via the Transwell did not adversely affect capillary sprouting, as revealed by the equivalent total network lengths (**Fig. 3.3D**). Together, these data demonstrate that DFs dominate the bulk stiffening of the scaffolds, while the ECs undergoing morphogenesis did not significantly affect the bulk mechanical properties of the constructs in this assay.

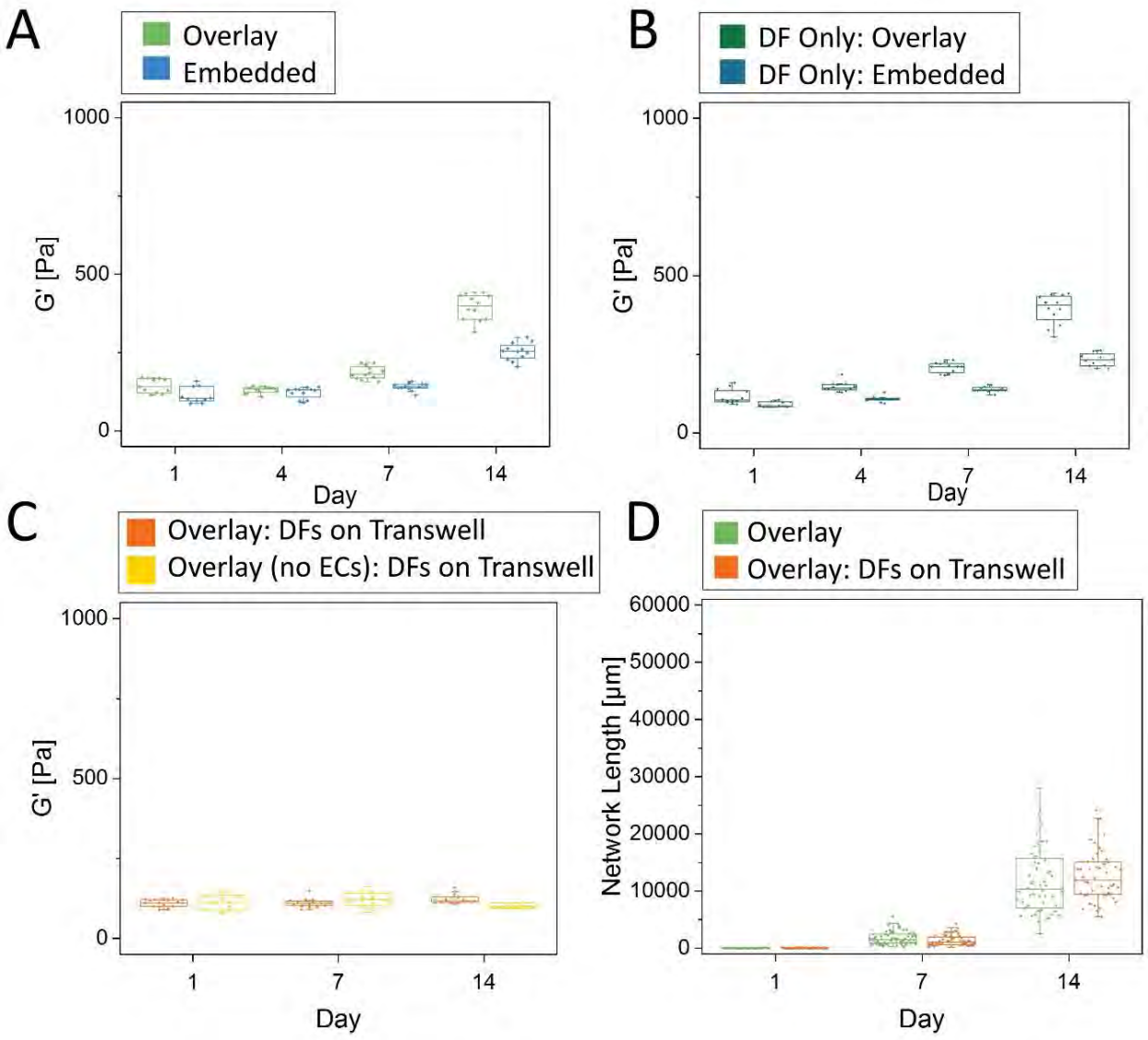

Figure 3.3: **Bulk rheology reveals an increase in stiffness with time during morphogenesis**. Parallel plate rheology of **(A)** bead assay in both the Overlay and Embedded conditions, (**B)** fibrin constructs with only DFs (no ECs) either overlaid on top of the gel or embedded within, and **(C)** a bead assay and a fibrin construct with DFs located on a Transwell (N=3 independent experiments for each time point and condition). Asterisks in **(A)** and **(B)** indicate statistical differences from all other time points for a given assay type ($p<0.05$). **D)** Quantified network lengths between the Overlay condition and Overlay with DFs on a Transwell (multiple ROIs assessed per sample, N=3, per condition, per time point). There were no statistical differences between Transwell and Overlay conditions for any given day. Boxed regions show median and interquartile range (IQR) of aggregate data, whiskers show range within 1.5 IQR.

3.4.4 Capillary morphogenesis is accompanied by dynamic spatiotemporal changes in local ECM stiffness and organization:

Results from selected AMR measurements for both overlay and embedded conditions proximal to the endothelial sprouts show that ECM micro-stiffness changed considerably in both space and time during capillary sprouting (**Fig 3.4A**, **3.4B, phase**). In some cases, AMR beads in close proximity reported G' values that differed by as much as 5-10x within only a few microns in the same ECM (**Fig 3.4**, **arrows**). Matched maximum intensity confocal reflection z-projections (**Fig 3.4A, 3.4B, confocal reflection**) demonstrated how the ECM was simultaneously remodeled. At early time points (Days 1 and 4), a typical fibrin mesh was detected proximal to the ECs. Stepping through assembled z-stacks revealed a distinct high contrast fibrillar architecture surrounding Cytodex beads on Day 1 for both the overlay (**Supplementary, Video 3.1**) and embedded (**Supplementary, Video 3.2**) culture models; this architecture is a hallmark signature of fibrin's microstructure. In the embedded model, however, the ECM was already changing spatially around the embedded fibroblasts. By Day 14, this fibrillar meshwork was replaced with a diffuse signal indicative of remodeling by the cells at later time points (Days 7 and 14). The fibrous structure was difficult to resolve near capillaries in the overlay conditions (**Supplementary, Video 3.3**), and throughout the dish for embedded cultures (**Supplementary, Video 3.4**)**.** Interestingly, changes in pericellular ECM architecture over time did not necessarily correlate with regions of elevated stiffness as measured by AMR in the same locations. This was particularly evident in the Day 7 overlay condition, where punctate stiff areas are found both in and out of the remodeled area, though generally appears elevated near sprouts.

3.4.5 AMR quantitatively reveals significant local ECM stiffness heterogeneities during capillary morphogenesis:

AMR measurements were conducted for both the overlay and embedded conditions in triplicate, and the results are shown in aggregate (**Fig 3.5A)**. Generally, there was an increase in average micro-stiffness over time. As early as Day 1, the embedded condition showed a broader range of G' values as compared to the overlay condition, with both conditions showing an orders-

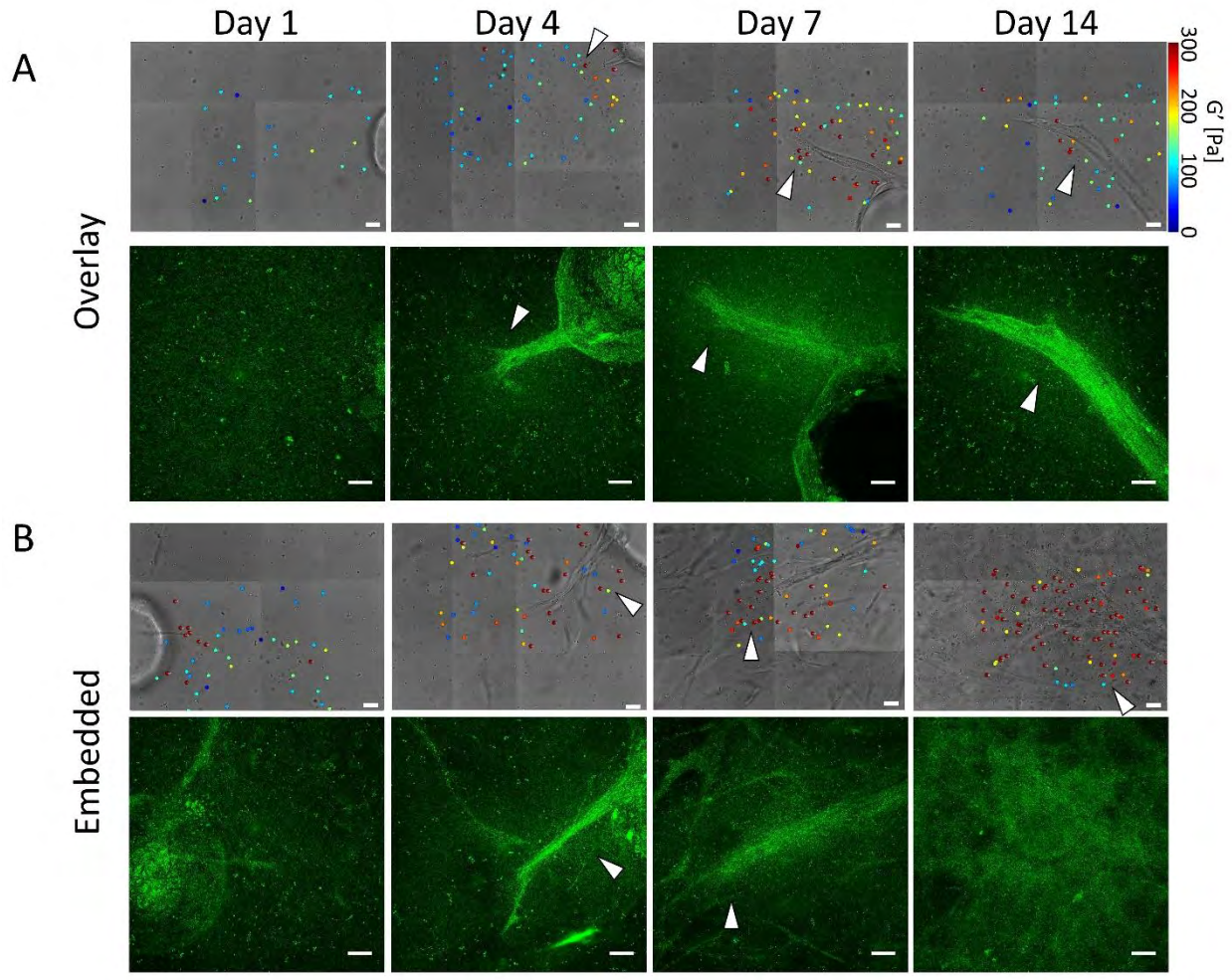

Figure 3.4: Capillary morphogenesis is accompanied by dynamic spatiotemporal changes in local ECM stiffness and organization. Selected stiffness maps generated using AMR and corresponding confocal reflection maximum intensity z-projections for the **(A)** Overlay and **(B)** Embedded conditions. Z-projections were created from 60 µm z-stacks with a step size of 1 µm, with those planes affected by distortion from the coverglass trimmed out prior to z-projection. Scale bar = 20 µm for brightfield images and 20 µm for reflection confocal z-projections. Arrows added emphasize areas where there is close proximity of stiffness heterogeneity, especially in the context of areas that appear different from the fibrous structure of fibrin. Please note the color map for G' saturates at 300 Pa. Stiffness values for individual beads reporting stiffness above 300 Pa are annotated on the beads.

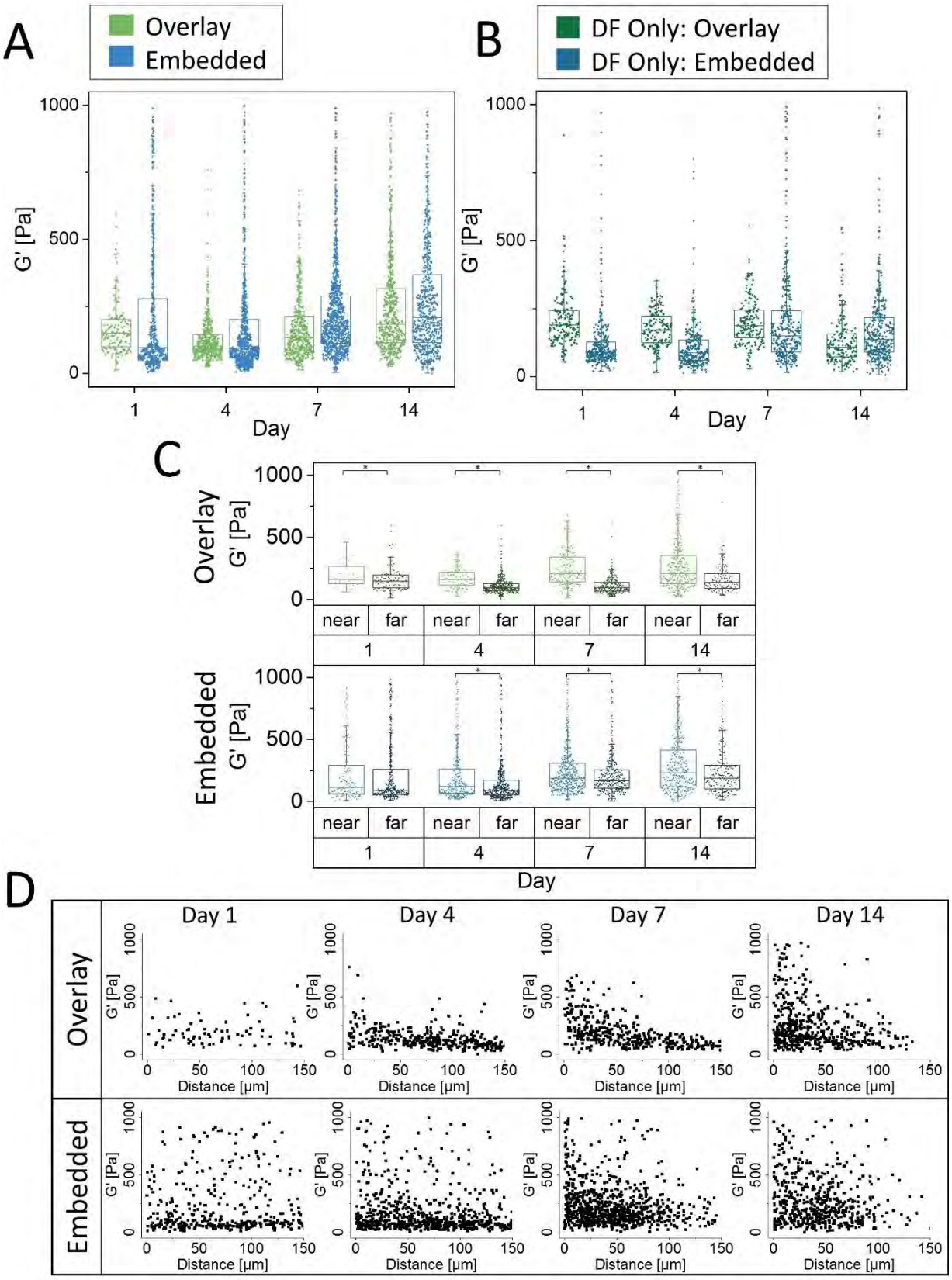
A
Overlay
Embedded
G' [Pa]
1000
500
0
1
4
7
14
Day
B
DF Only: Overlay
DF Only: Embedded
G' [Pa]
1000
500
0
1
4
7
14
Day
C
Overlay
G' [Pa]
Embedded
G' [Pa]
near
far
1
4
7
14
Day
D
Overlay
Embedded
Day 1
Day 4
Day 7
Day 14
G' [Pa]
Distance [µm]
0
50
100
150

Figure 3.5: AMR quantitatively reveals significant local ECM stiffness heterogeneities during capillary morphogenesis. **A)** Microrheology proximal to the sprout tips in both the Overlay and Embedded conditions (aggregate data, N=3 per condition, per timepoint). **B)** Microrheology in fibrin constructs only containing DFs (no ECs) either overlaid on top of the gel or embedded within (aggregate data, N=3 independent samples, with $n_{AMRbeads}$>150 per time point, per condition). **C)** Microrheology from (**A**) segregated into two classes, near or far, based on distance from endothelial cells (<50 μm or >50 μm, respectively). For panels A-C, asterisks indicate statistical differences between groups ($p<0.05$) Boxed regions show median and interquartile range (IQR) of aggregate data, whiskers show range within 1.5 IQR. **D)** Microrheology data from (A) plotted as a function of probe bead proximity to the ECs.

of-magnitude distribution. Within the embedded condition, this heterogeneity was observed as early as Day 1. Consistent with acellular gels (**Fig 3.2C**), average local stiffness in the overlay condition decreased slightly between Days 1 and 4 ($p<0.05$), and by Day 14 was similar on average to the embedded condition. To assess the effects of DFs on the peri-endothelial stiffness, AMR was conducted in fibrin gels containing only fibroblasts in both the overlay and embedded conditions (**Fig 3.5B**). In the embedded case, the effects of fibroblast remodeling were evident (increasing *G'*) by Day 7, whereas in the overlay case, no such effect was observed. In fact, overlay gels softened at Day 14 ($p<0.05$, compared to all other days), an effect not observed with bulk rheology (**Fig 3.3B**).

To further analyze the spatial distribution of stiffness observed in both the overlay and embedded conditions, AMR measurements were classified as either near or far, based on the proximity of each probe particle (<50μm or >50μm, respectively) to the nearest endothelial tubule (**Fig 3.5C**). Within these conditions, *G' near* is significantly greater than *G' far* at all time points, except for Day 1 of the embedded case (Mann-Whitney Test, $p<0.05$). This indicates that the effects of endothelial vessel stiffening of the ECM are concentrated proximal to the vessel, with the effect dissipating with distance. Plots of *G'* as a function of probe bead proximity to the ECs (**Fig 3.5D**) show that in the overlay case stiffening is concentrated in a region approximately

within 50 μm of the ECs and increases over time. In contrast, the stiffness topography is more heterogeneous at all time points in the embedded case.

3.5 DISCUSSION

Branching morphogenesis is a complex phenomenon that occurs throughout the life of all metazoan organisms (181), and there is strong evidence that ECM mechanics and cell-generated forces play important roles in shaping the organization (and disorganization) of both normal and diseased tissues (182, 183). Studies using biomimetic materials have shown that matrix stiffness regulates cell fate in 2D (165) and 3D (167). More recent studies have shown the ECM's mechanical regulation of cell behavior goes well beyond initial bulk material properties (e.g., compressive, tensile, shear moduli), with strong evidence that stress relaxation (184), fibrillar architectures (65), mechanical patterns/gradients (185, 186), and dynamic changes in mechanical properties (187–189) all play significant roles. To better understand the mechanical influence of a natural ECM on a complex morphogenetic process in 3D, we applied a laser tweezers-based active microrheology method and traditional parallel plate shear macrorheology to a well-established and biologically relevant 3D fibrin-based co-culture model of capillary morphogenesis, and tracked the spatiotemporal evolution of the micro- and macro-scale shear elastic modulus during the formation of an extensive microvascular network.

AMR revealed mechanical micro-heterogeneities within acellular fibrin-based matrices, with G' values spanning an order of magnitude within each gel. This microscale heterogeneity increased in the presence of cells and with time in culture, coincident with an overall increase in the bulk G' values of the tissue constructs. Experiments to dissect the cellular origins of this increased stiffness revealed that the supportive DFs largely accounted for the observed increases in the bulk mechanical properties of the ECM, as DF monocultures lacking ECs also increased

their bulk mechanical properties with time in culture. Additional experiments in which DFs were cultured on a Transwell insert placed on top of the gel revealed that the bulk mechanical properties of gels not in physical contact with DFs did not increase. Equivalent EC sprouting occurred when DFs were in direct contact with the gel or on a Transwell. Because we have previously shown that sprouting is deficient in the presence of fibroblast-conditioned media (171), these experiments show that reciprocal cross-talk between ECs and DFs necessary for morphogenesis still occurs when the latter are cultured on Transwells.

While the bulk mechanical property changes were largely attributable to the DFs, AMR revealed that ECs undergoing sprouting angiogenesis also progressively stiffened the ECM as they invaded. Significant increases in the micro-stiffness of the ECM occurred within 50 μm ("near") of the sprouting vessel-like structures, regardless of whether DFs were overlaid or embedded in the matrix. The AMR experiments in the overlay conditions were particularly indicative of the EC-induced local stiffening because the DFs were located on top of the gel a fixed distance away from the z-plane (> 500 μm) in which the EC-coated beads tend to settle and in which our AMR measurements were taken. The increased heterogeneity of G' values with time in the "near" region proximal to the vessel-like structures in the overlay conditions was also likely due to ECs. ECs apply traction forces (64, 170) and deposit new matrix (190) during capillary morphogenesis, both of which would be expected to locally stiffen the ECM.

In addition to our AMR measurements, we observed changes in ECM architecture during morphogenesis via confocal reflection microscopy. Previous studies have shown that EC tubules invading a fibrous collagen ECM deposit new collagen matrix (appearing specular as opposed to fibrillar) proximal to the lumen as EC tubules grow (190). The ECM's appearance proximal to vessels in our culture models (**Supplementary Videos 3 and 4)** was consistent with these previous

findings. What has not been clear is how such changes affect local stiffness over time. Our AMR results show that local stiffness heterogeneity increased over time in culture, an effect localized to EC tubules in the overlay culture, but ubiquitous in the embedded cultures that contain an increasing population of DFs. In some cases, stiffness distal to EC tubules and located in fibrous ECM increased to values similar to those found proximal to EC tubules in specular ECM. Furthermore, this distal effect was limited in extent for the overlay conditions; beyond ~50 μm from the tubule surface, stiffness values were similar to those measured by bulk rheology and AMR of acellular gels. Therefore, areas of obvious matrix remodeling did not necessarily coincide with regions of elevated stiffness or even the greatest stiffness heterogeneities. This observation casts important limitations on methods that correlate mechanical properties with fiber architecture (191) or rely on quantification of fiber deformations (192).

In the context of vascular morphogenesis, inconsistencies regarding the roles of ECM mechanics remain in the literature. Early evidence demonstrated that mechanical cues directly impact tubulogenesis, with softer gels better able to support capillary morphogenesis in 2D (193, 194). In 3D cultures, angiogenic process extension was attenuated in fibrin gels whose mechanical properties were manipulated by adding exogenous factor XIII to form additional cross-links (195). We previously demonstrated that increasing fibrin's bulk mechanical properties by increasing fibrinogen concentration beyond the physiologic provisional clot concentration used here (~2.5 mg/mL) (180) results in significant reductions in angiogenic sprouting not only *in vitro* (172) but also *in vivo* (196); however, sub-physiologic concentrations yield overly soft gels that slowed angiogenic invasion due to reduced resistance to cell-generated traction forces (64). Efforts to decouple ECM stiffness from other cues using glycated collagen matrices have demonstrated that stiffer ECM promotes increased angiogenic outgrowth, invasion, and branching, independent of

changes in matrix density (197, 198). Similarly, angiogenic invasion of ECs was increased in collagen gels cross-linked with transglutaminase to increase the stiffness without affecting the concentration (199). However, other studies have reported that increased stiffness induced by collagen glycation attenuates vessel morphogenesis (200, 201).

Because of the limitations of natural ECMs and the inconsistencies in the literature, we (and many others) have turned to synthetic material platforms in an effort to decouple the mechanical and chemical effects of the ECM and thereby differentiate the contributions of mechanical cues in isolation. In such systems, softer, less cross-linked gels susceptible to cell-secreted proteases were better able to support the formation of vessel-like networks *in vitro* (114, 202); the identity of the degradable peptides was a bigger influence than the starting mechanical properties of the gels on the formation of functional microvasculature *in vivo* (114). However, engineered hydrogels lack key features of native ECM, which is typically fibrillar, macroporous, heterogeneous, mechanically anisotropic, and is actively remodeled by the cells that reside within it. The amorphous nature and mechanical homogeneity of synthetic gels are essential for their utility in 3D traction force microscopy (203), but questions remain regarding their physiological relevance for addressing mechanistic questions.

Our findings underscore the importance of characterizing across length scales when deciphering the roles of ECM mechanics on morphogenesis in 3D. Bulk rheology was useful for establishing ensemble averaged mechanical properties and quantifying the large degrees of stromal cell-mediated matrix remodeling with a relatively accessible technique. Understanding bulk properties is important for handling of tissue constructs and regenerative medicine applications. By contrast, AMR was useful for the precise spatiotemporal quantification of ECM mechanics on subcellular length scales during 3D capillary morphogenesis in soft fibrin matrices. Similar AMR

measurements have also revealed enormous heterogeneity in the micromechanical properties of type-I collagen gels (204). Interestingly, in these collagen gels, local cell-mediated stiffening requires both myosin-mediated traction forces (204) and active proteolysis via MMPs (205). Future work will address if the wide spatiotemporal variations in ECM stiffness observed during capillary growth and invasion in soft fibrin gels translate to other natural materials (of different concentrations), and if they directly influence phenotypic bifurcations (i.e., cell fate decisions), including the induction of vessel branching or the guidance of vascular invasion.

3.6 SUPPLEMENTARY FIGURES AND VIDEOS

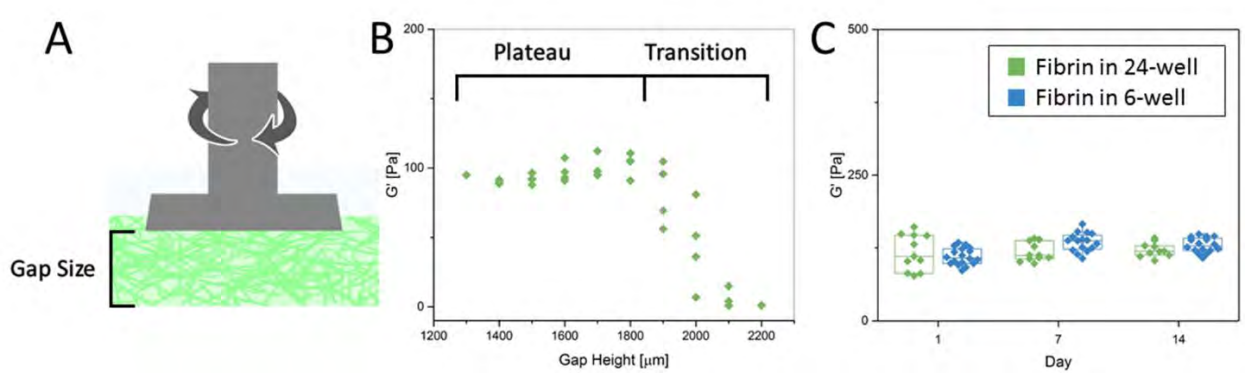

Figure 3.6: Acellular fibrin gels in culture plates reach consistent plateau value for G' and are consistent across well sizes. A) Schematic illustrating gap height from bottom of sample to measurement head. B) Shear modulus as a function of gap height is shown as the rheometer measurement head was progressively lowered onto acellular fibrin gels cast in 24-well plates. A plateau value of ~110 Pa was quickly reached after the measurement head made contact with the gels and was consistent over hundreds of microns before gradually decreasing. (Aggregate data shown, N=4) C) Shear modulus is consistent between 24-well (2.5 cm^2) and 6-well (9.8 cm^2) plates across time. One-way ANOVA resulted in $p = 0.60$ between all conditions and time points. (Aggregate data shown, N=3, per condition, per time point)

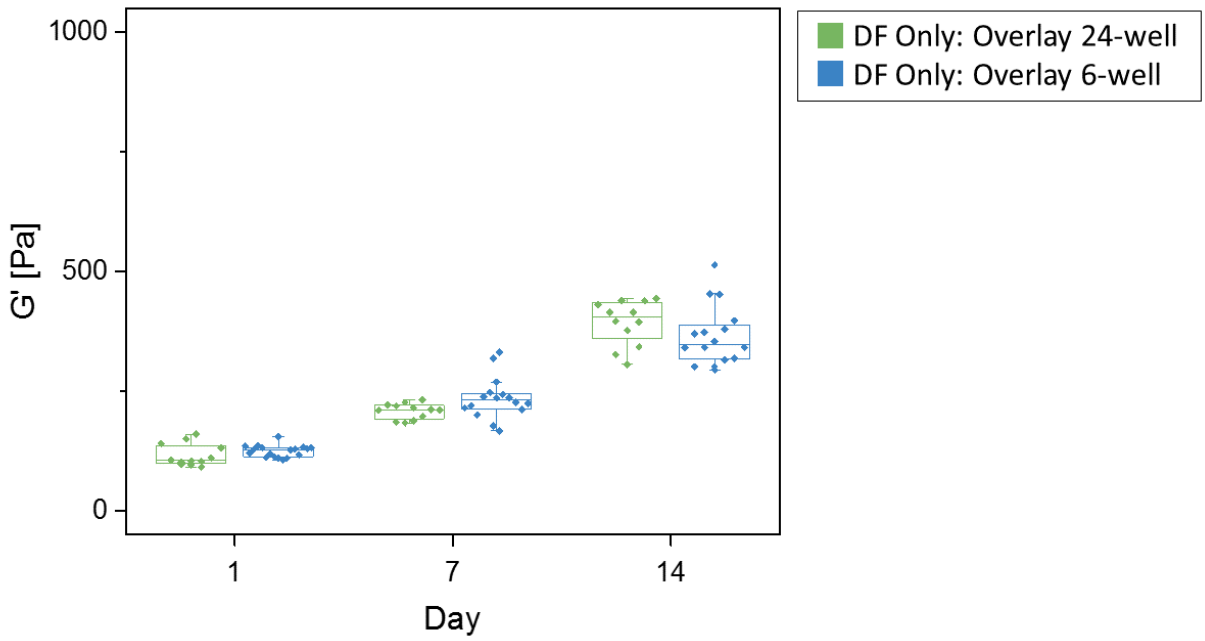

Figure 3.7: Culture well size does not influence stiffening behavior of overlay conditions. Bulk G' on days 1, 7, and 14 was unaffected by the size of well in which cells were cultured, as assessed with t-tests between matching conditions. (Aggregate data shown, N=3 for all conditions)

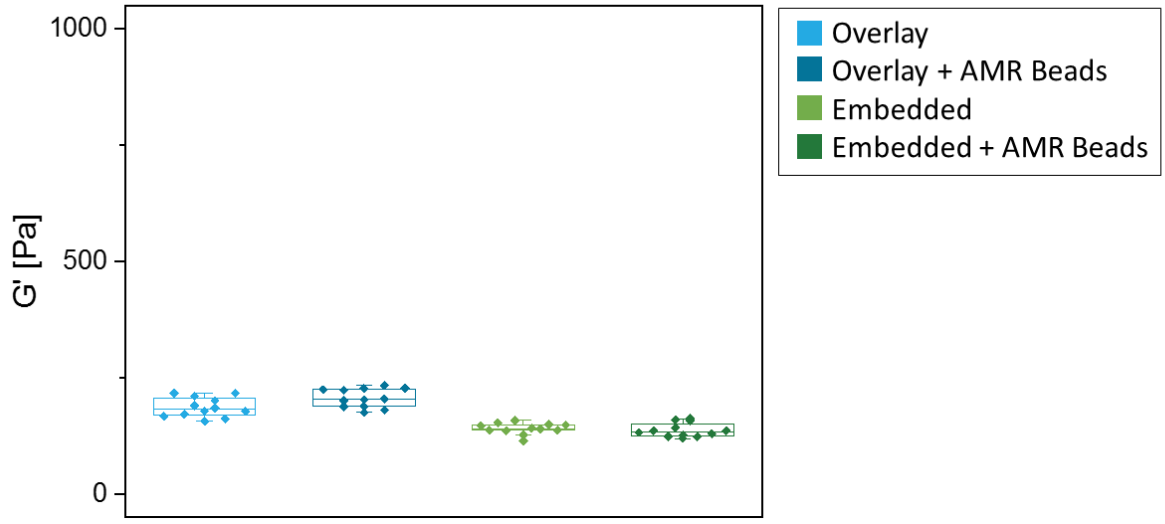

Figure 3.8: Inclusion of AMR beads does not influence bulk G' of cell cultures on Day 7. Bulk G' was unaffected by the inclusion of AMR beads for either co-culture model, as assessed with t-tests between matching conditions. (Aggregate data shown, N=3 for all conditions)

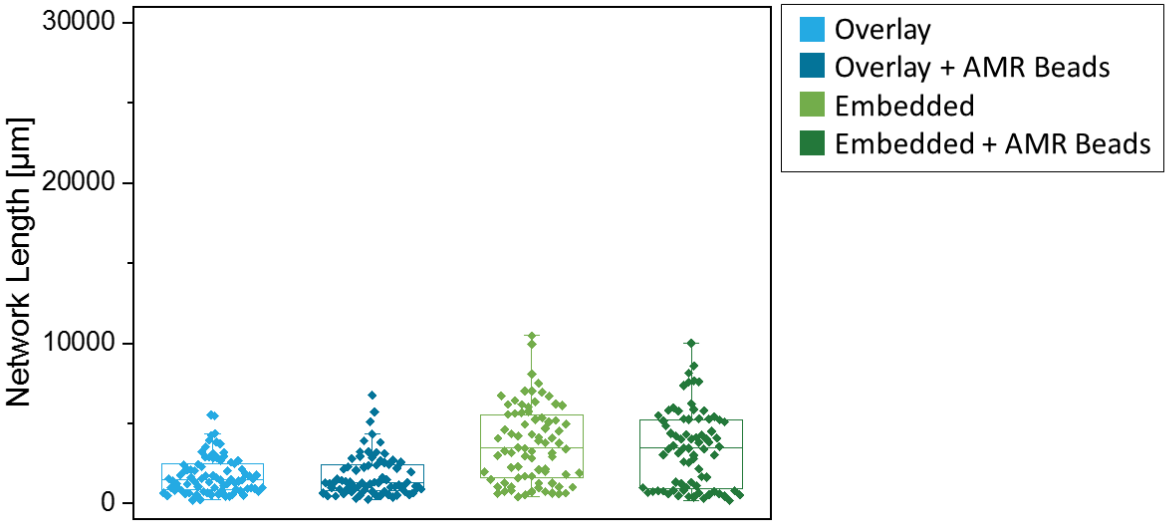

Figure 3.9: Inclusion of AMR beads does not influence capillary network formation at Day 7. Average network lengths were unaffected by the inclusion of AMR beads for either co-culture model, as assessed with t-tests between matching conditions. (Aggregate data shown, N=3 for all conditions)

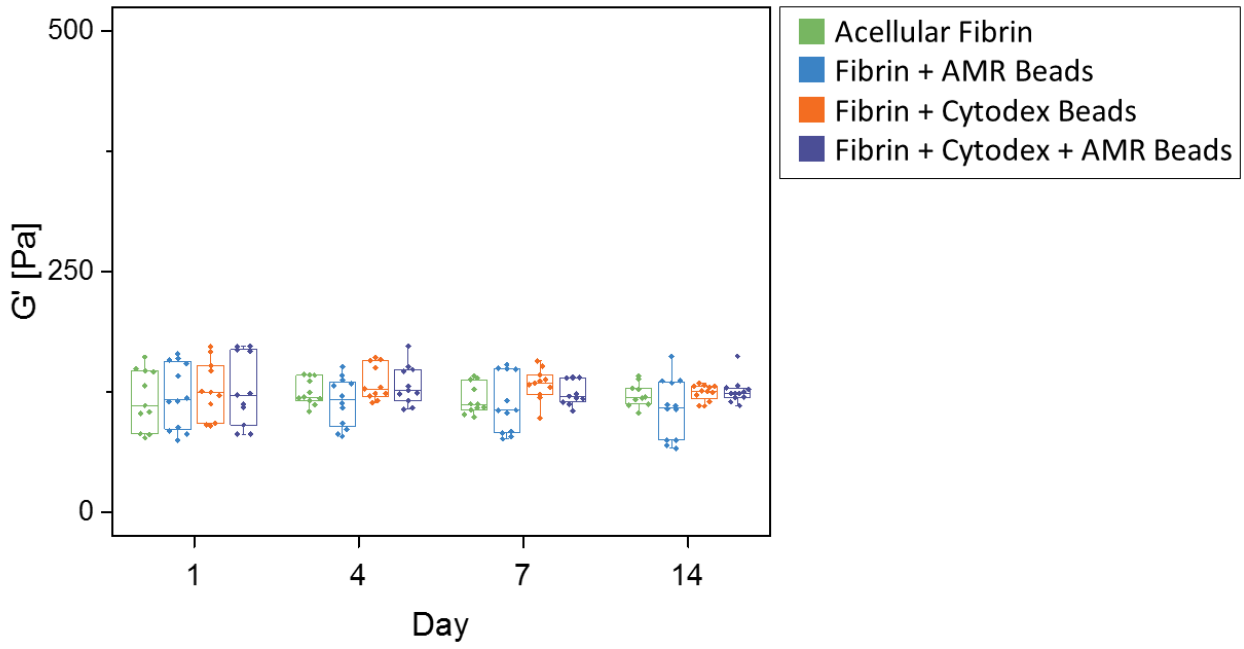

Figure 3.10: Inclusion of Cytodex and/or AMR beads does not influence the bulk properties of acellular gels over time. No significant differences in bulk G' were observed between any condition across all time points. One-way ANOVA resulted in $p = 0.91$ between all conditions and time points. (Aggregate data shown, N=3, per condition, per time point)

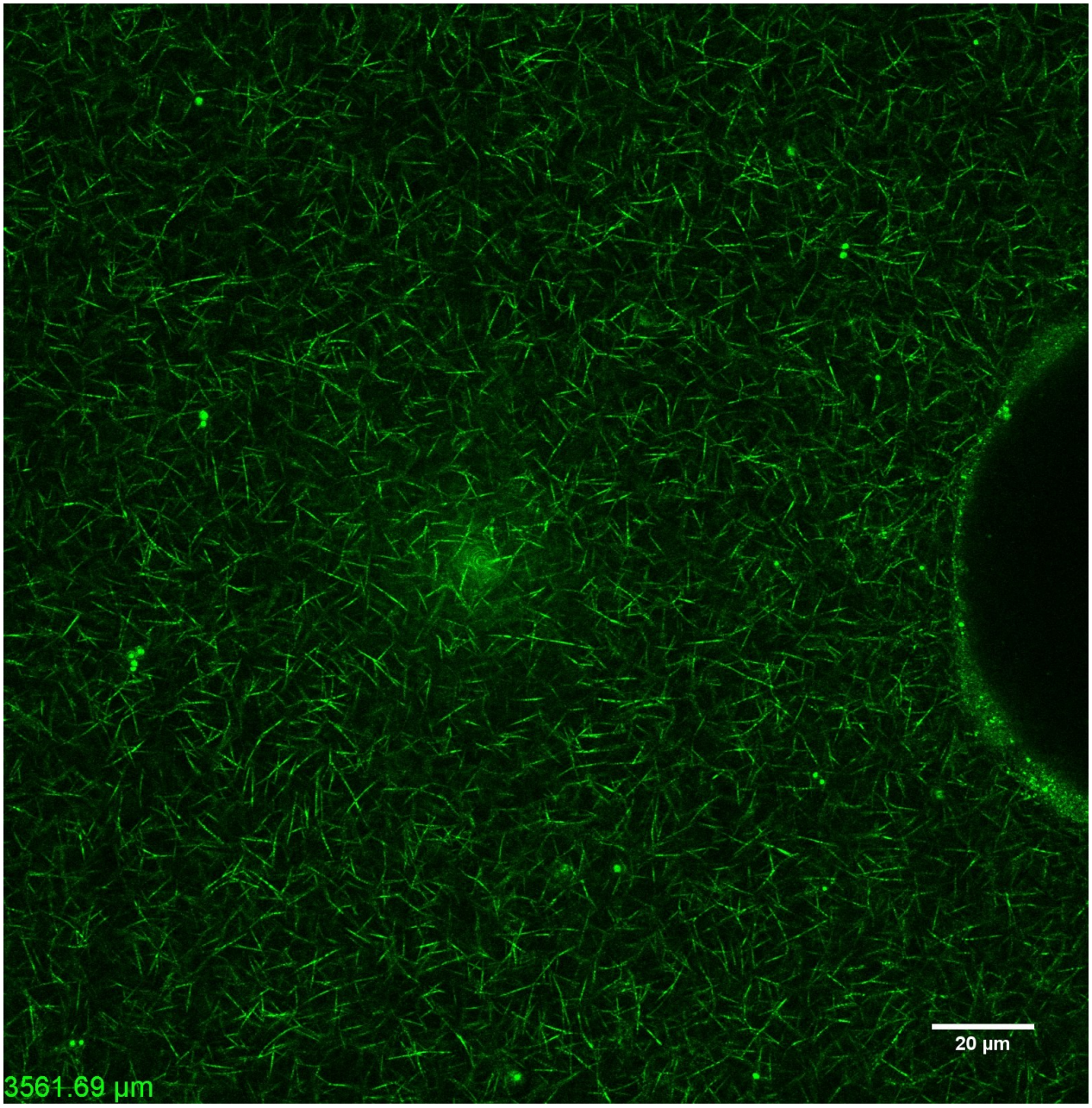

Video 3.1: Day 1 Overlay Condition - Reflection confocal z-stack. EC-coated cytodex bead within fibrin matrix highlighting the structure of the fibrin matrix prior to sprouting when DFs are in the overlay configuration.

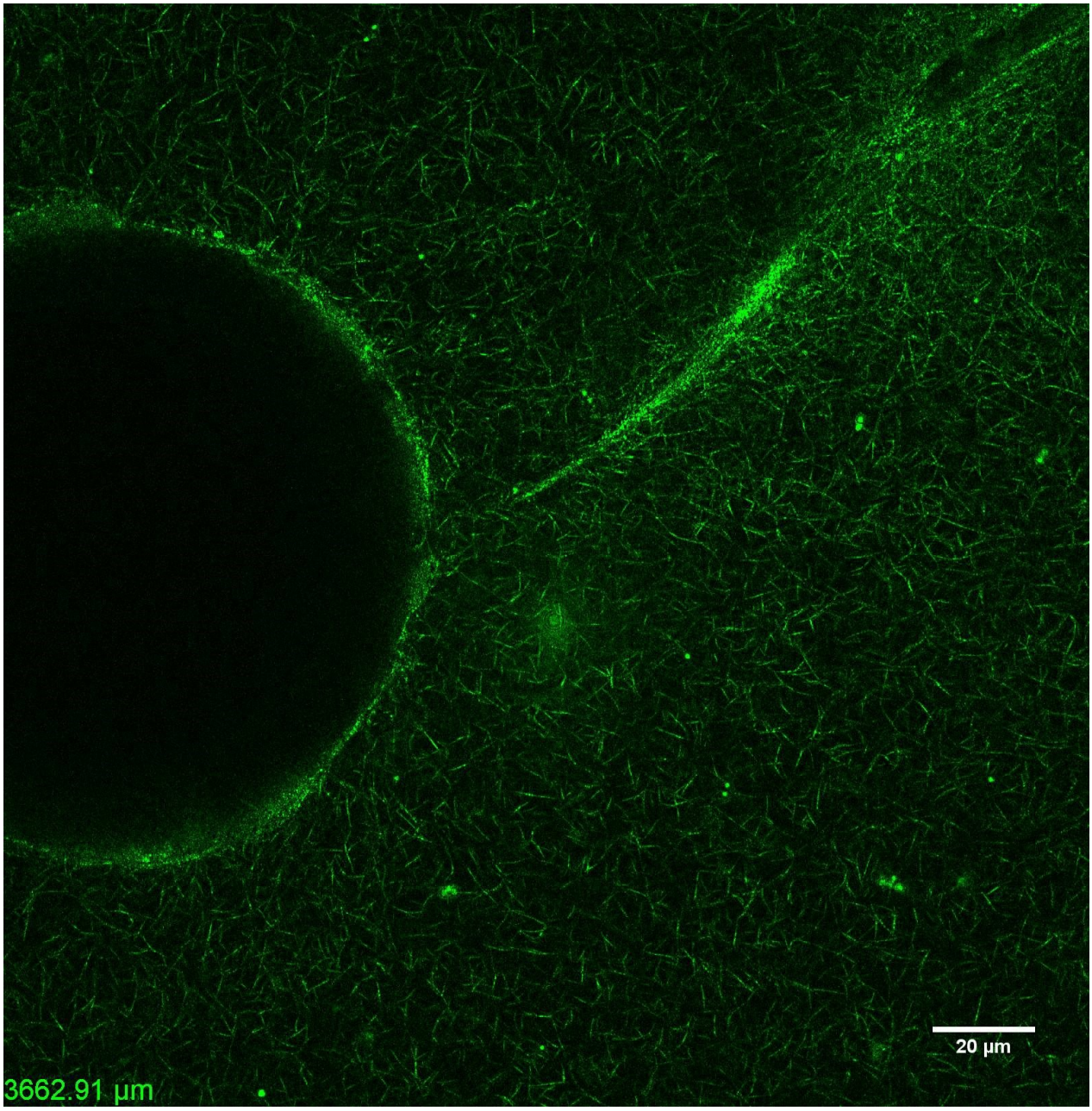

Video 3.2: Day 1 Embedded Condition - Reflection confocal z-stack. EC-coated cytodex bead within fibrin matrix highlighting the structure of the fibrin matrix prior to sprouting when DFs are in the embedded configuration.

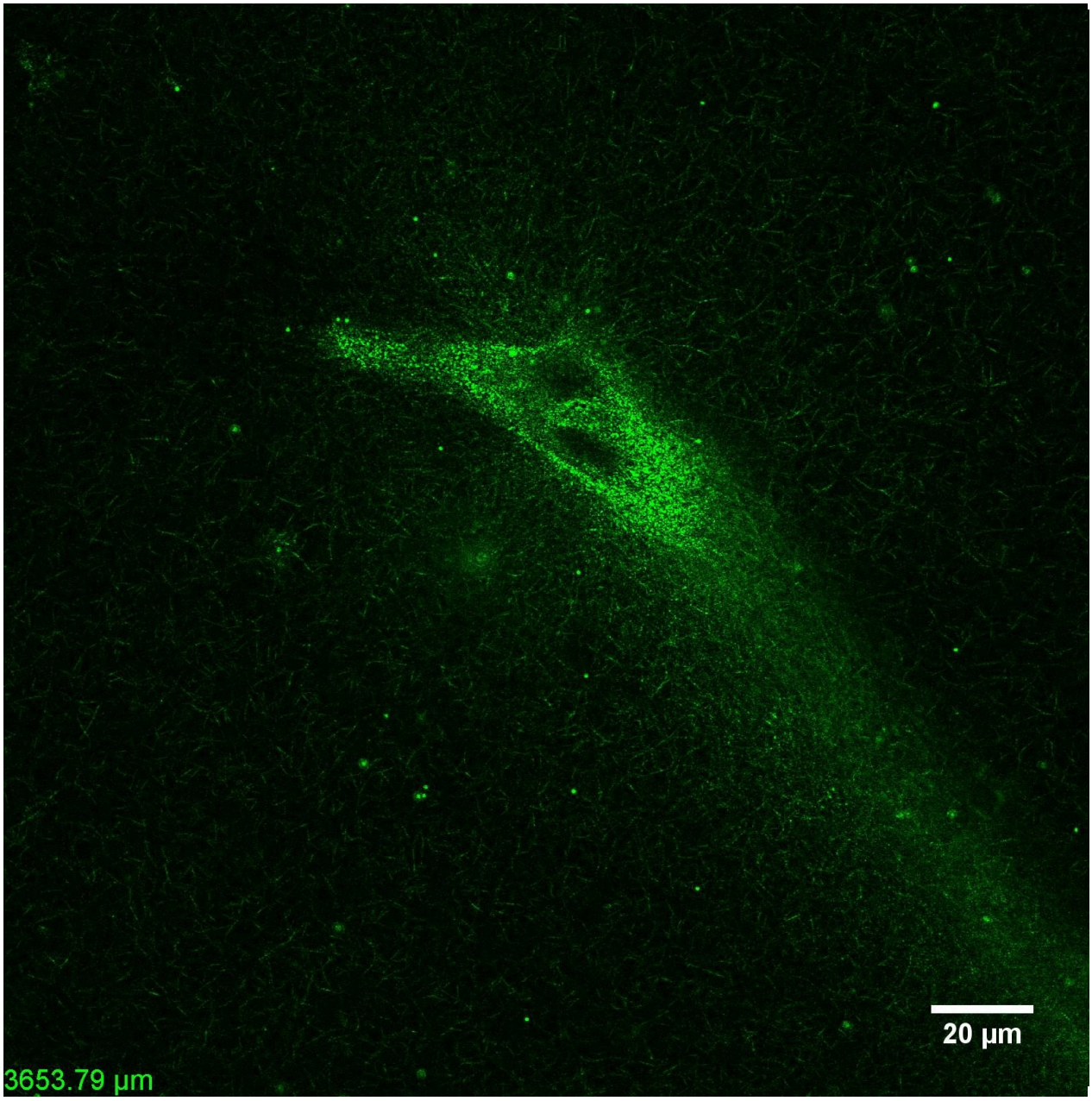

Video 3.3: Day 14 Overlay Condition - Reflection confocal z-stack. EC sprout within fibrin matrix highlighting the structure of the fibrin matrix following 14 days of growth with DFS in the overlay configuration.

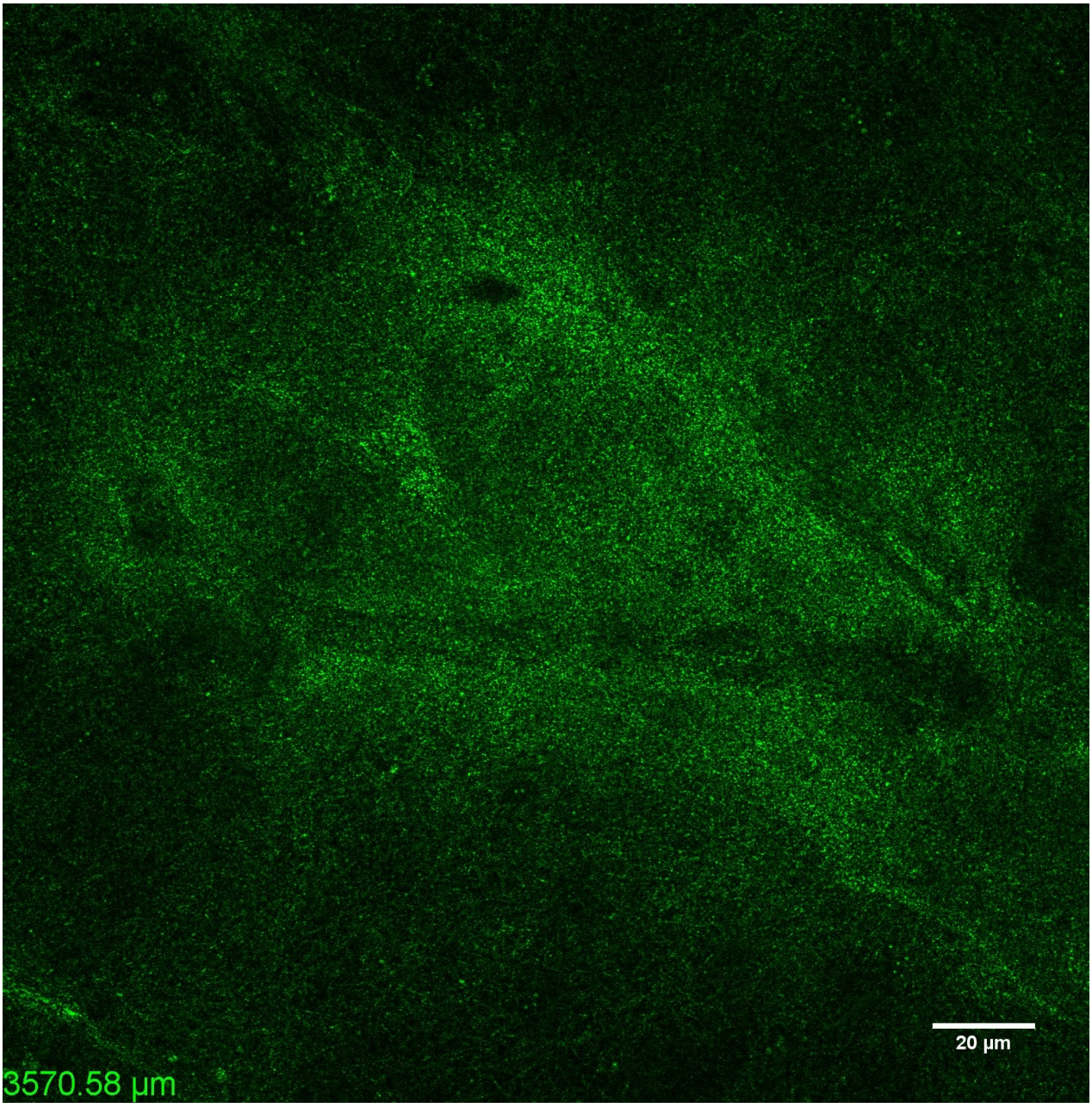

Video 3.4: Day 14 Embedded Condition - Reflection confocal z-stack. EC sprout within fibrin matrix highlighting the structure of the fibrin matrix following 14 days of growth with DFS in the embedded configuration.

CHAPTER IV

Deciphering The Relative Roles Of Matrix Metalloproteinase- And Plasmin-Mediated Matrix Degradation During Capillary Morphogenesis Using Engineered Hydrogels

4.1 ABSTRACT

Extracellular matrix (ECM) remodeling is essential for the process of capillary morphogenesis. Here we employed synthetic poly(ethylene glycol) (PEG) hydrogels engineered with proteolytic specificity to either matrix metalloproteinases (MMPs), plasmin, or both to investigate the relative contributions of MMP- and plasmin-mediated ECM remodeling to vessel formation in a 3D-model of capillary self-assembly analogous to vasculogenesis. We first demonstrated a role for both MMP- and plasmin-mediated mechanisms of ECM remodeling in an endothelial-fibroblast co-culture model of vasculogenesis in fibrin hydrogels using inhibitors of MMPs and plasmin. When this co-culture model was employed in engineered PEG hydrogels with selective protease sensitivity, we observed robust capillary morphogenesis only in MMP-sensitive matrices. Fibroblast spreading in plasmin-selective hydrogels confirmed this difference was due to protease preference by endothelial cells, not due to limitations of the matrix itself. In hydrogels engineered with crosslinks that were dually susceptible to MMPs and plasmin, capillary morphogenesis was unchanged. These findings highlight the critical importance of MMP-mediated degradation during vasculogenesis and provide strong evidence to justify the preferential selection of MMP-degradable peptide crosslinkers in synthetic hydrogels used to study vascular morphogenesis and promote vascularization.

4.2 INTRODUCTION

The microvasculature is essential to the normal function, maintenance, and repair of nearly all tissues. This complex network continuously evolves to meet changing demands of tissues. Throughout this process, the extracellular matrix is continuously remodeled, making extracellular proteolytic systems central to the regulation of capillary morphogenesis (5, 206). There are a wide range of proteolytic systems implicated in the formation of new vessels (206). Matrix metalloproteinases (MMPs), and in particular the membrane-type (MT)-MMPs, have emerged as critical mediators of matrix remodeling not only in collagen but also in fibrin (7, 12, 55, 56). However, the serine protease plasmin, which is also activated at the cell membrane, may provide an alternative mechanism for proteolytic remodeling, and in some conditions, is necessary for capillary morphogenesis in fibrin (58–61). The relative importance of these systems in capillary morphogenesis therefore remains an open question.

In 3D models, endothelial cells co-cultured with supporting stromal cells undergo capillary morphogenesis (7). We have observed that stromal cell identity modulates the contribution of the plasmin pathway to this process in fibrin (7, 101) and have correlated these observations with differences in the extent of vessel formation, morphology, and permeability both *in vitro* (7, 10) and *in vivo* (11). These findings suggest the mechanisms of proteolytic remodeling during vessel formation may dictate functional properties of the resulting capillary network, which has important implications for the design of synthetic biomaterial scaffolds that support the formation of new vessels.

Deciphering the roles of specific proteolytic pathways has traditionally leveraged molecular genetic tools to create knock-out cells and animals (12, 56). However, redundancies in proteolytic enzyme expression and mechanisms of ECM degradation may complicate

interpretations from knock-outs. To complement such approaches, here we used engineered hydrogels (114) with selective degradability to investigate the relative importance of MMP- versus plasmin-dependent ECM degradation during capillary morphogenesis in 3D.

4.3 MATERIALS AND METHODS

4.3.1 Cell culture

All reagents were obtained from Thermo Fisher Scientific (Waltham, MA) unless specified. Human umbilical vein endothelial cells (ECs) were harvested from fresh umbilical cords and cultured in fully supplemented EGM2 (Lonza, Walkersville, MD) as previously described (172). ECs were used between passages 2-4. Normal human dermal fibroblasts (DFs, Lonza) and normal human lung fibroblasts (LFs, Lonza) were cultured in Dulbecco's modified eagle medium (DMEM) supplemented with 10% fetal bovine serum (FBS) and 1% penicillin streptomycin and were used up to passage 15. Bone marrow mesenchymal stem cells (MSCs, RoosterBio, Frederick, MD) were cultured in RoosterNourish-MSC medium (RoosterBio) and used up to passage 5. All cells were cultured at 37 ºC and 5% CO_2 with thrice weekly medium exchange. These cell types were chosen because prior work has suggested they exhibit differential utilization of MMP- and plasmin-mediated proteolysis (7, 101).

4.3.2 Fibrin-based vasculogenesis assay with drug inhibitors

A 3D model of capillary morphogenesis was adapted from our previously described protocol (77) as follows. ECs ($1.25x10^5$ cells/mL) and a supportive stromal cell type ($1.25x10^5$ cells/mL) were distributed in 0.5 mL fibrin hydrogels formed in a 24-well culture plate from 2.5 mg/mL of 0.22 μm filtered bovine fibrinogen (Sigma-Aldrich, St Louis, MO) dissolved in serum free DMEM and polymerized with 1 U/mL bovine thrombin (Sigma). After gelation, 1 mL of Vasculife VEGF Endothelial Medium (Lifeline Cell Technology LLC, Frederick, MD) was

added to the hydrogel with indicated inhibitors. Aprotinin, derived from bovine lung (Sigma), was added in sterile water at a final concentration 2.2 μM, which is nearly 3 orders of magnitude greater than the IC50 for plasmin (4 nM) (207) and has been previously shown to have a saturating effect on capillary morphogenesis (62). The broad-spectrum MMP inhibitor, GM6001 (Sigma), was supplemented in a constant volume of DMSO vehicle to achieve indicated concentrations.

4.3.3 PEG-VS hydrogel formation

Hydrogels were formed from 4-arm poly(ethylene glycol) vinyl sulfone (PEG-VS; 20 kDa, Jenkem USA, Allen TX) and a combination of thiol containing adhesive and protease-sensitive peptides adapted from published protocols (114, 127). All reagents were prepared in batches of single-use aliquots. Peptides, dissolved in 25 mM acetic acid, and PEG-VS, dissolved in ultrapure water, were 0.22 μm filtered, lyophilized, and stored desiccated at -20 ºC. Precise thiol content of each batch of peptide aliquots was determined using Ellman's reagent. An optimal thiol:vinyl sulfone ratio (typically 0.8-0.9) which yielded the maximum hydrogel shear modulus was also determined for each batch. Immediately before use, PEG-VS was dissolved in HEPES (100 mM, pH 8.4) and CGRGDS peptide (RGD, Genscript, Piscataway, NJ) was reacted with the PEG-VS for 30 min at a final concentration of 400 μM. In rapid succession, dithiol crosslinking peptides at the optimized thiol:vinyl sulfone ratio (accounting for RGD conjugation) were added to the PEG-VS solution, gently mixed, dispensed into a sterile 0.5 (for 30 μl gels) or 1 mL (50 μl gels) syringe with the needle end cut off, and allowed to polymerize for 1 h at 37 ºC in a sealed 50 mL conical tube. Crosslinking peptides included: Ac-GCRDVPMS↓MRGGDRCG-NH2 ("VPMS"), Ac-GCYK↓NRDCG-NH2 ("YKNR"), Ac-GCYK↓NRDVPMS↓MRGGDRCG-NH2 ("Dual"), and Ac-GCY($_{D}$-K)N($_{D}$-R)DCG-NH2 ("Y$_{D}$-

KN_{D}-R") each containing an N-terminal acetylation and a C-terminal amidation (Genscript, cleavage site indicated by ↓). Polymerized hydrogels were punched into culture medium or phosphate buffered saline (PBS).

4.3.4 Mechanical and proteolytic characterization of PEG-VS hydrogels

Hydrogels were allowed to swell overnight, then were mounted on an AR-G2 rheometer (TA Instruments, New Castle, DE) between an 8-mm measurement head and a Peltier stage, each covered with P800 sandpaper. Shear storage modulus (G') was determined at 0.05 N normal force, 5% strain amplitude, and 1 Hz frequency and averaged over a 2-minute time sweep. For proteolysis experiments, hydrogels were allowed to swell overnight then transferred to either 5 mU/mL plasmin from human plasma (Sigma) in PBS or to 1 U/mL collagenase IV from *Clostridium histolyticum* (used as a qualitative surrogate for MMP degradation as both MMPs and collagenase IV were found to degrade the VPMS peptide sequence) in PBS supplemented with 0.4 mM $CaCl_2$ and 0.1 mM $MgCl_2$. Shear modulus was measured at 0, 3, and 24 h. 30 μL hydrogels were used for proteolysis experiments. 50 μL hydrogels were used for all other experiments.

4.3.5 PEG-based vasculogenesis assays

Hydrogels were formed as above except that a cell pellet was resuspended just after adding the dithiol peptide to achieve a final cell density of $2x10^6$ cells/mL of each cell type. 50 μl samples of the resulting suspension were dispensed into 1 mL syringes and polymerized as above. Each hydrogel was cultured in 2 mL of medium in a 12-well plate for 7 d. Either EGM2 or Vasculife VEGF medium were used for these studies. Controls comparing results in both medium types were performed for selected conditions. For the drug inhibitor studies, medium

was exchanged daily and inhibitors were added as in the fibrin-based experiments. For all other experiments, medium was exchanged on days 1, 3, and 5.

4.3.6 Fluorescent imaging and quantification methods

On day 7, co-cultures were fixed with Z-fix (Anatech, Battle Creek, MI). All PEG-VS hydrogels were cut down the cylinder diameter prior to staining, yielding two halves. Samples were stained with rhodamine-conjugated lectin from *Ulex europaeus* (UEA, Vector Laboratories, Burlingame, CA, specific for endothelial cells, 1:200), 4', 6-diamidino-2-phenylindol (DAPI, 1 μg/ml, Sigma), and AlexaFluor 488 phalloidin (1:200). PEG-hydrogels were imaged on the cut side to ensure images were representative of cellular behavior within the hydrogels. Images were acquired using an Olympus IX81 microscope equipped with a disk scanning unit (DSU, Olympus America, Center Valley, PA) and Metamorph Premier software (Molecular Devices, Sunnyvale, CA). For all analyses, confocal z-stacks were acquired using the DSU. Z-series were collapsed into maximum intensity projections prior to analysis. Quantifications of vessel and nuclei densities were performed on 300 μm stacks (30 μm/slice) imaged at 4x. Total vessel length per region of interest (ROI) was quantified using the Angiogenesis Tube Formation module in Metamorph and reported as vessel length per volume of ROI (2.16 x 1.65 x 0.3 mm). Total nuclei per ROI was quantified using a custom ImageJ script (included in appendices). Cell body circularity and projected cell area per volume of ROI were quantified from 30 μm thick stacks (3 μm/slice) imaged at 10x with a custom ImageJ script (included in appendices). For each sample, 6 ROIs were used to determine a mean for each of 3 independent experiments.

4.3.7 Statistics

Statistical analysis was performed using GraphPAD Prism (La Jolla, CA). Unless noted, data are represented as mean ± standard deviation of at least 3 independent experiments. Data

were analyzed using one- or two-way ANOVA with Tukey post-hoc testing for pre-specified comparisons. A value of $\alpha < 0.05$ was considered significant.

4.4 RESULTS

4.4.1 Synergistic restriction of vasculogenesis by broad spectrum inhibition of MMP- and serine protease-dependent pathways is stromal cell dependent.

We first investigated how inhibition of MMP-dependent and plasmin-dependent fibrinolysis affected capillary morphogenesis in a model of vasculogenesis in which ECs were distributed with DFs, LFs, or MSCs for 7 d in fibrin hydrogels. The extent of baseline capillary morphogenesis depended on stromal cell identity, with the length of networks in EC-MSC co-cultures 50% and 39% compared to EC-LF or EC-DF co-cultures respectively (**Fig 4.1** and **Supplemental, Fig 4.7**). Baseline capillary morphogenesis was unaffected by vasculogenic medium used (**Supplemental, Fig 4.8**). GM6001, a broad-spectrum inhibitor of MMPs, consistently reduced vessel formation in a dose-dependent manner regardless of stromal cell identity (**Fig 4.1** and **Supplemental, Fig 4.7**, $p < 0.0001$ by two-way ANOVA). Aprotinin, a broad-spectrum inhibitor of serine-proteases including plasmin, similarly tended to reduce vessel formation regardless of stromal cell identity (**Fig 4.1**, $p < 0.05$ by two-way ANOVA). The magnitude of the effect, however, was comparatively subtle for EC-MSC co-cultures (**Fig 4.1D**). In the absence of GM6001, aprotinin did not affect vessel density. However, the combination of aprotinin and GM6001 revealed a synergistic inhibitory effect from aprotinin that depended on GM6001 concentration for EC-DF and EC-LF co-cultures (two-way ANOVA interaction term $p = 0.035$ and 0.0009, respectively) but not MSCs ($p = 0.46$, **Fig 4.1** and **supplemental, Fig 4.7**). In EC-LF and EC-DF co-cultures, concentrations of GM6001 that were orders of magnitude

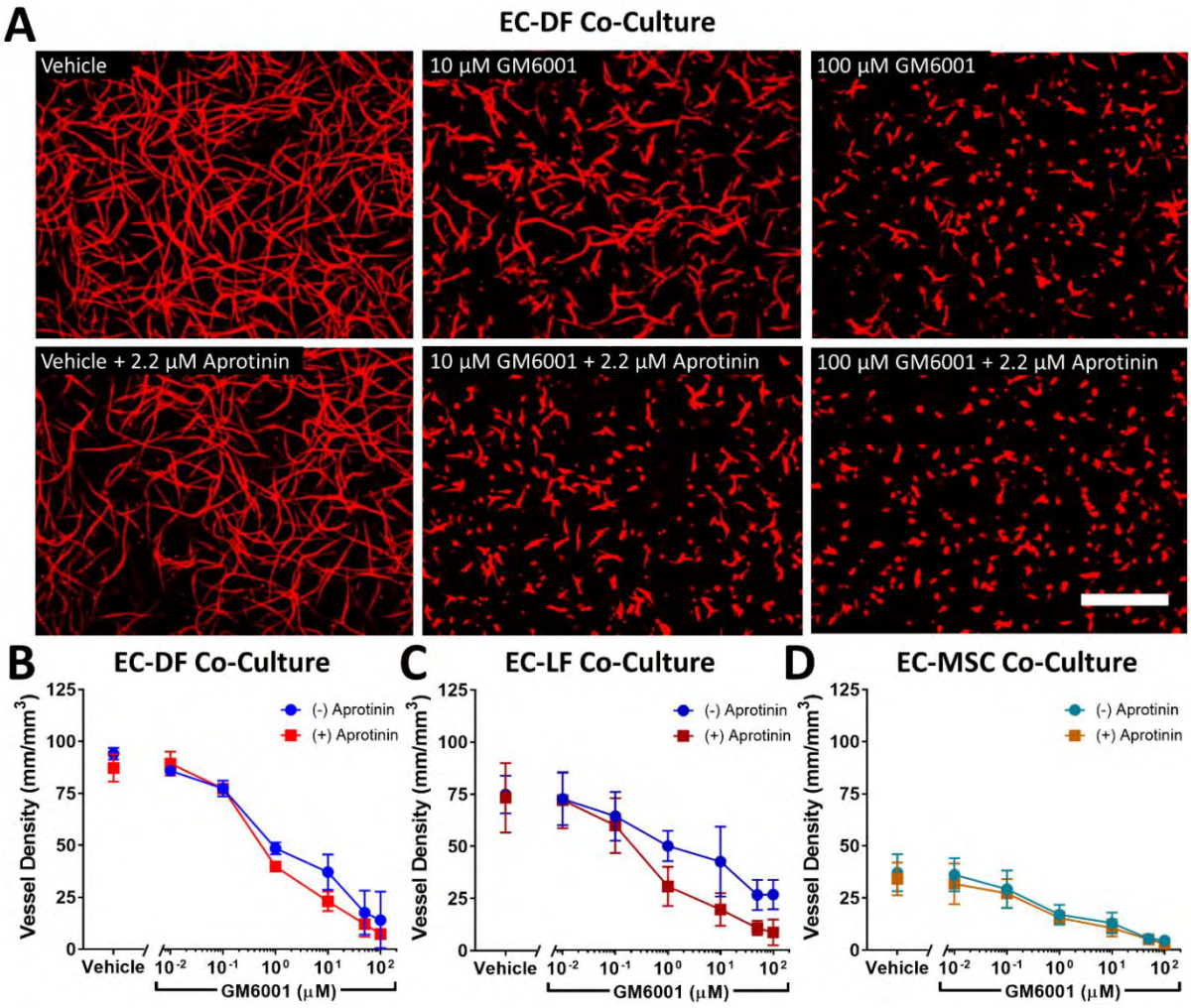

Figure 4.1: Aprotinin acts synergistically with GM6001 to inhibit vasculogenesis in endothelial cell (EC) co-cultures with dermal fibroblasts (DFs) and lung fibroblasts (LFs) but not in co-cultures with bone-marrow mesenchymal stem cells (MSCs) in 2.5 mg/mL fibrin hydrogels. Representative images of capillary-like networks formed in EC-DF co-cultures after 7 d with indicated inhibitor concentrations are shown stained with the endothelial-selective lectin from *Ulex europaeus* (UEA, red) to highlight networks (A). Scale bar = 500 µm. Multiple images at prespecified locations were acquired for each condition for co-cultures of ECs and DFs (B), LFs (C), or MSCs (D) for 3 independent experiments and network lengths were quantified per volume as outlined in the methods. Two-way ANOVA (GM6001, aprotinin, interaction) results: EC-DF ($p < 0.0001$, $p = 0.0218$, $p = 0.0349$), EC-LF ($p < 0.0001$, $p = 0.0059$, $p = 0.0009$), EC-MSC ($p < 0.0001$, $p = 0.0177$, $p = 0.459$).

greater than the nM IC50 range for most MMPs (208) were insufficient to fully inhibit capillary morphogenesis unless aprotinin also was present. Because inhibition of either protease system alone was insufficient to block capillary morphogenesis, these results support a model of partial proteolytic plasticity for vasculogenesis in EC-fibroblast co-cultures in fibrin. As a preliminary

study to assess whether plasminogen delivered in culture media serum contributed to this synergistic restriction of capillary morphogenesis, we also quantified vessel formation in serum-free media. Contrary to expectation, vessel formation in the presence of all 3 stromal cell types exhibited synergistic restriction of vessel formation with increasing concentrations of GM6001 and inclusion of aprotinin (**Supplemental, Fig 4.9**).

We also evaluated whether aprotinin and GM6001 induced changes in cell spreading and proliferation in serum containing cultures. The effects of protease inhibition on combined cell density (both EC and stromal cell) closely mirrored vessel density (**Supplemental, Fig 4.10**). Qualitatively, protease inhibition affected spreading of endothelial cells more than stromal cells. Aprotinin and maximal GM6001 severely attenuated, but did not completely block, spreading of any stromal cell type (**Supplemental, Fig 4.11**).

4.4.2 Direct matrix degradation by plasmin is insufficient to support robust capillary morphogenesis.

To investigate the hypothesis that fibroblasts induce both MMP- and plasmin-mediated matrix remodeling during capillary morphogenesis, we generated synthetic extracellular matrices using 4-arm PEG-VS crosslinked with peptides selectively degradable nearly exclusively by either MMPs or plasmin (**Fig 2A**) (114, 127). Hydrogels formed from PEG-VS crosslinked with YKNR were rapidly degraded by plasmin as assessed by loss of shear modulus over time, while equivalent hydrogels formed from either a negative control peptide synthesized with the D-isomer of lysine and arginine (Y_D-KN_D-R) or VPMS were unaffected by plasmin after 24h (**Fig 4.2B**). Inclusion of aprotinin at 2.2 μM prevented YKNR-hydrogel degradation by plasmin, resulting in gels with G' values of 141 ± 10 Pa after 24 hours ($p=0.42$ compared to untreated

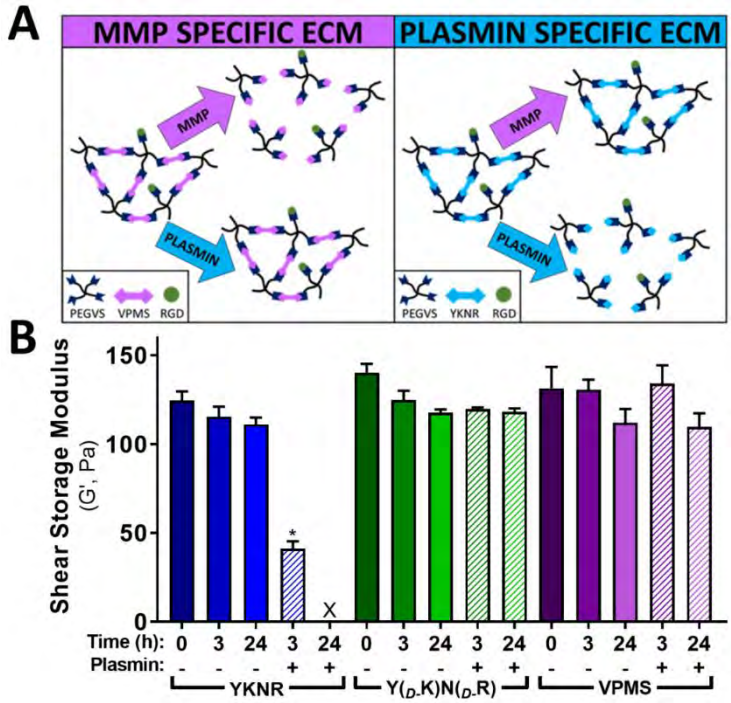

Figure 4.2: Design of MMP- and plasmin-selective PEG-VS hydrogels. We designed PEG-VS hydrogel scaffold systems with selective protease sensitivity by crosslinking multiple-arm PEG-VS with dithiol peptides with selective sensitivity to plasmin or MMPs (A). Hydrogels were crosslinked, swollen in PBS overnight, exposed to plasmin (5 mU/mL), and at indicated times, characterized by shear rheology. Hydrogels crosslinked with YKNR were readily degradable by plasmin as measured by shear rheology, whereas VPMS and Y_D-KN_D-R crosslinked hydrogels were insensitive to plasmin Fig 2: Design of MMP- and plasmin-selective PEG-VS hydrogels. We designed PEG-VS hydrogel scaffold systems with selective protease sensitivity by crosslinking multiple-arm PEG-VS with dithiol peptides with selective sensitivity to plasmin or MMPs (A). Hydrogels were crosslinked, swollen in PBS overnight, exposed to plasmin (5 mU/mL), and at indicated times, characterized by shear rheology. Hydrogels crosslinked with YKNR were readily degradable by plasmin as measured by shear rheology, whereas VPMS and Y_D-KN_D-R crosslinked hydrogels were insensitive to plasmin (B).

YKNR control). Taken together, these data show that plasmin exclusively degrades YKNR hydrogels.

Because DFs are readily available from skin and therefore may represent a viable cell source for engineered microvascular constructs, we primarily focused on this stromal cell type for further investigation in engineered PEG-VS hydrogel matrices with some comparison to LF supported cultures. When ECs and DFs were co-encapsulated within plasmin-sensitive YKNR hydrogels with formulations similar to our prior work (~40 mg/mL PEG-VS) (114), there was no

clear evidence of capillary morphogenesis. By contrast, capillary-like structures were observed in MMP-sensitive VPMS hydrogels (**Fig 4.3A and 4.3B**). To investigate the possibility that vasculogenesis was limited by a grossly supraphysiologic number of matrix cleavage sites, we reduced the concentration of PEG-VS to generate hydrogels with decreasing crosslink density, as assessed by shear rheology, to the practical limits of gelation (G' range for 27 mg/mL PEG-VS hydrogels 37 to 61 Pa, Fig 3C). This approach reduced the number of proteolysis events required for local hydrogel dissolution as well as diffusion restrictions. Hydrogel crosslinking, assessed

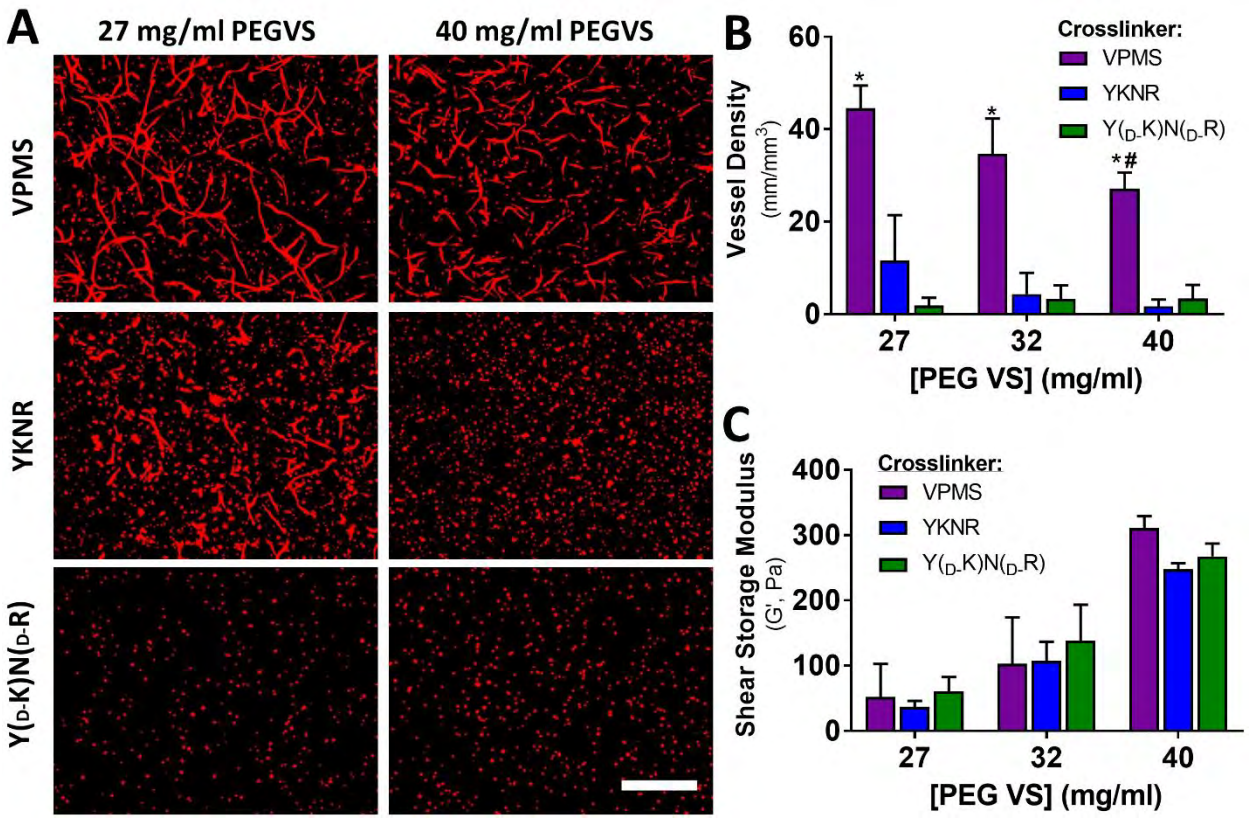

Figure 4.3: Capillary morphogenesis is severely restricted in YKNR hydrogels regardless of crosslinking density. UEA (red) images from the centers of the constructs (see methods) are shown for loose (27 mg/mL PEG-VS) and dense (40 mg/mL) VPMS, YKNR, and Y_D-KN_D-R crosslinked hydrogels. Capillary-like networks formed in EC-DF co-cultures at all concentrations of PEG-VS when crosslinked with VPMS. In YKNR hydrogels, limited vessel formation was only observed in the softest (27 mg/mL) hydrogel formulation. No vessel formation was observed in non-degradable hydrogels (A). Scale bar: 500 μm. Vessel network length was quantified in each scaffold (*: p = 0.0009 compared with Y_D-KN_D-R at fixed concentration, #: p = 0.008 compared with 27 mg/mL VPMS) (B). Peptide identity did not influence the shear modulus of hydrogels (two-way ANOVA: p = 0.40) (C).

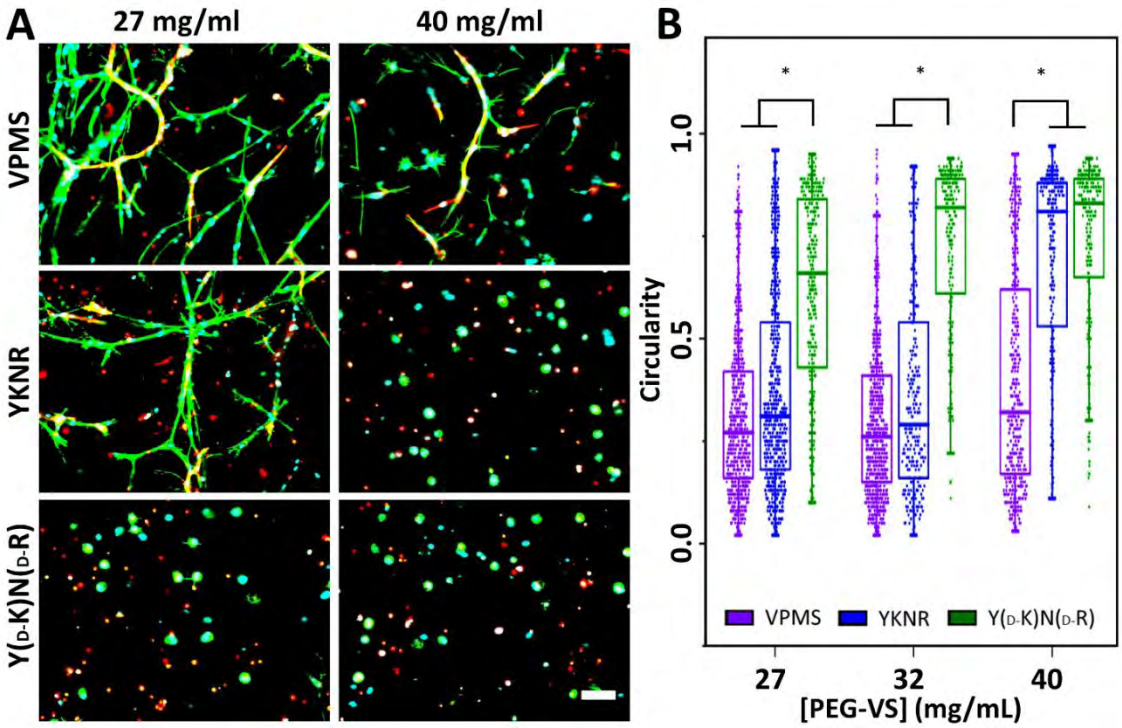

Figure 4.4: Reduced crosslinking density allows for fibroblast spreading in YKNR crosslinked PEG-VS hydrogels. ECs and DFs were encapsulated in PEG-VS hydrogels with varying peptide identity and crosslinking density, controlled by initial PEG-VS concentration. UEA (red), phalloidin (green), and DAPI (blue) co-stained images from the centers of the constructs are shown for loose (27 mg/mL PEG-VS) and dense (40 mg/mL) VPMS, YKNR, and $Y_{D}KN_{D}R$ crosslinked hydrogels (A). Fibroblasts are phalloidin positive but UEA negative. Scale bar: 100 μm. Circularity was quantified (see methods) as a measure of cell spreading in loose (27 mg/mL PEG-VS), intermediate (32 mg/mL), and dense (40 mg/mL) crosslinked hydrogels (*: $p \leq 0.003$ for comparison shown) (B).

by shear rheology, did not depend on the crosslinking peptide identity (p= 0.30, **Fig 4.3C**). In loosely crosslinked YKNR hydrogels, we observed rare areas of minimal capillary morphogenesis (Fig **4.3A** and **4.3B**), but the formation of capillary-like structures was never as robust as observed in VPMS crosslinked hydrogels. Lack of vessel formation in 27 mg/mL YKNR hydrogels was also observed in LF supported cultures in a preliminary comparison to DF supported cultures (**Supplemental, Fig 4.12**). Quantified vessel density in 27 mg/mL YKNR hydrogels was similar to that seen in $Y_{D}KN_{D}R$ controls (Fig 3B, p= 0.42). In VPMS hydrogels, vessel density was greater in 27 mg/mL compared with 40 mg/mL (Fig 3B, p = 0.008). Capillary

morphogenesis in VPMS hydrogels did not depend on the vasculogenic medium used (**Supplemental, Fig 4.13**).

To confirm that cell-mediated degradation is possible in plasmin-selective hydrogels, we examined cell spreading in EC-dermal fibroblast co-cultures (**Fig 4.4A**) and quantified cell circularity as a measure of cell spreading (**Fig 4.4B**). Circularity discriminates rounded versus spread cells (values of 1 indicate perfectly round cells, lower circularity indicates increased elongation). Circularity was low for a large fraction of cells in all VPMS and loosely-crosslinked YKNR hydrogels but was near 1 for most cells in 40 mg/mL YKNR hydrogels (**Fig 4.4B**). The lack of spreading in any Y_D-KN_D-R hydrogels indicated cell spreading depended on matrix degradation (**Fig 4.4B**). Qualitatively, we noted cell spreading in YKNR hydrogels predominantly occurred in UEA negative fibroblasts (**Fig 4.4A**), suggesting EC spreading was disproportionately restricted in plasmin-selective hydrogels.

4.4.3 Hydrogels with dual susceptibility to both plasmin and MMPs do not enhance vasculogenesis compared with MMP-selective hydrogels.

Our results to this point suggested that plasmin-mediated matrix remodeling was not sufficient to support capillary morphogenesis but did not rule out the possibility that plasmin may have an auxiliary role, perhaps partially degrading the matrix ahead of vessel invasion to facilitate localized MMP mediated degradation. To assess this possibility, we generated a synthetic ECM in which each crosslink could be degraded either by MMPs or by plasmin using a concatenated YKNR+VPMS dual susceptible peptide **(Fig 4.5A**). Hydrogels crosslinked with the dual susceptible peptide were degradable by both plasmin and collagenase (used as a surrogate for MMP-mediated degradation) **(Fig 4.5B**) and had shear moduli similar to VPMS controls (**Fig 4.5C**). EC-DF cocultures in dual susceptible hydrogels resulted in vessel density, projected cell

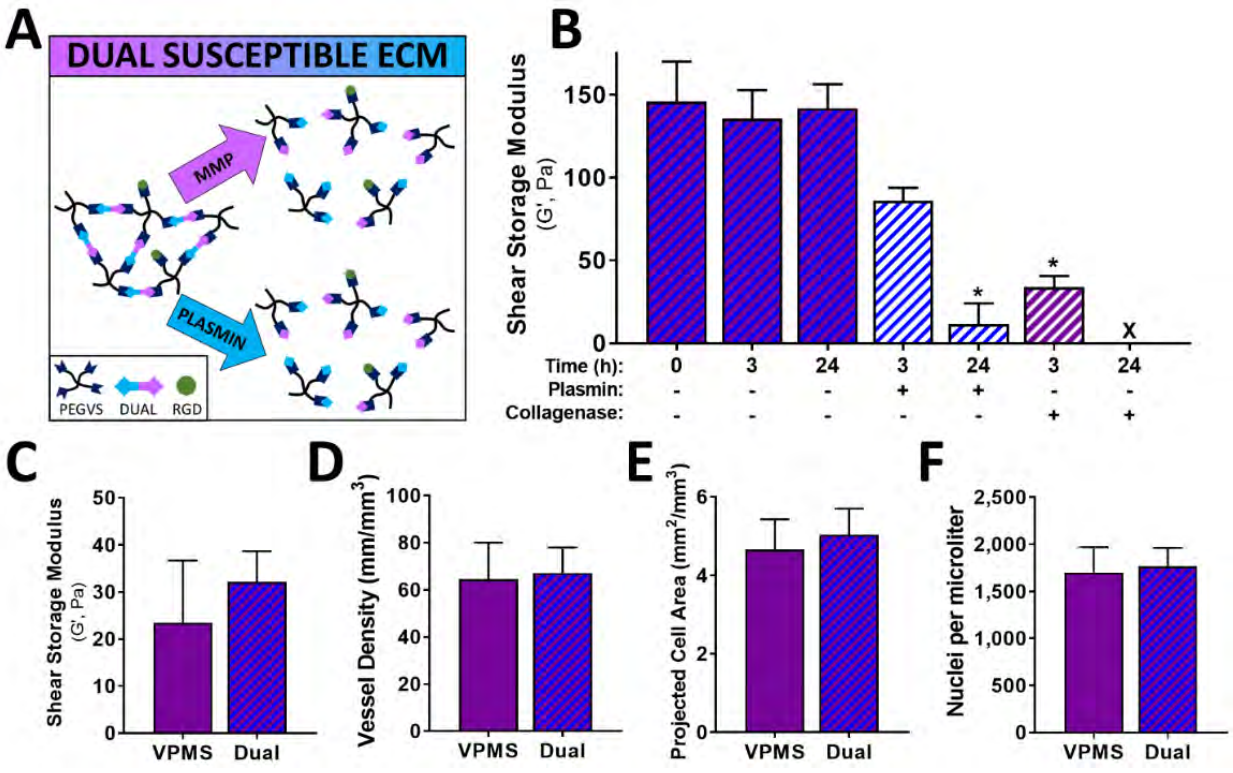

Figure 4.5: Hydrogels with crosslinks sensitive to either plasmin or MMPs did not enhance capillary morphogenesis. PEG-VS hydrogels were crosslinked with a concatenated peptide containing both VPMS and YKNR sequences and used to form scaffolds in which each crosslink was susceptible to either MMPs or plasmin (A). Dense PEG-VS hydrogels were crosslinked with the dual susceptible peptide, swollen in PBS overnight, exposed to indicated proteases, and at indicated times, characterized by shear rheology (B). EC-DF co-cultures were generated in intermediate-crosslinked (32 mg/mL PEG-VS) scaffolds crosslinked with either VPMS or dual-susceptible peptides (C-F). Network structure of these scaffolds, assessed by shear rheology, did not depend on crosslinking peptide ($p = 0.36$) (C). Vessel density, quantified after 7 d, was similar for VPMS and dual susceptible peptides ($p = 0.65$) (D). Cell spreading was estimated by projected cell area per volume and did not differ for VPMS and dual susceptible peptides ($p = 0.11$) (E). There were no differences in cell density after 7 d, measured by automated counting of DAPI stained nuclei per volume ($p = 0.63$) (F).

area, and nuclei density equivalent to gels crosslinked with the VPMS peptide (**Fig 4.5D, 4.5E, 4.5F**). Similarly, EC-LF cocultures did not exhibit any differences in vessel formation or nuclei densities between hydrogels crosslinked with either VPMS or dual susceptible peptides (**Supplemental, Fig 4.14A, 4.14B**)

4.4.4 Synergistic restriction of vasculogenesis by broad spectrum inhibition of MMP- and serine protease-dependent pathways is abolished in MMP-sensitive hydrogels.

Since plasmin can activate soluble MMPs, including those involved in capillary morphogenesis (5), another potential explanation for the reduced vasculogenesis in fibrin cultures containing aprotinin may be inhibition of plasmin-dependent activation of MMPs. To investigate this possibility, inhibition experiments similar to those shown in Fig 1 were repeated in VPMS crosslinked PEG-VS hydrogels that could only be degraded by MMPs. Similar to results in fibrin, GM6001 reduced vessel formation in a dose dependent manner (**Fig 4.6**, two-way ANOVA $p = 0.0003$). However, unlike in fibrin, we observed no meaningful differences in vasculogenesis when aprotinin was added to cultures containing GM6001 (**Fig 4.6**, two-way ANOVA, aprotinin effect $p = 0.21$, interaction $p = 0.75$). Similarly, no synergistic effect was observed in EC-LF co-cultures (**Supplemental, Fig 4.15**).

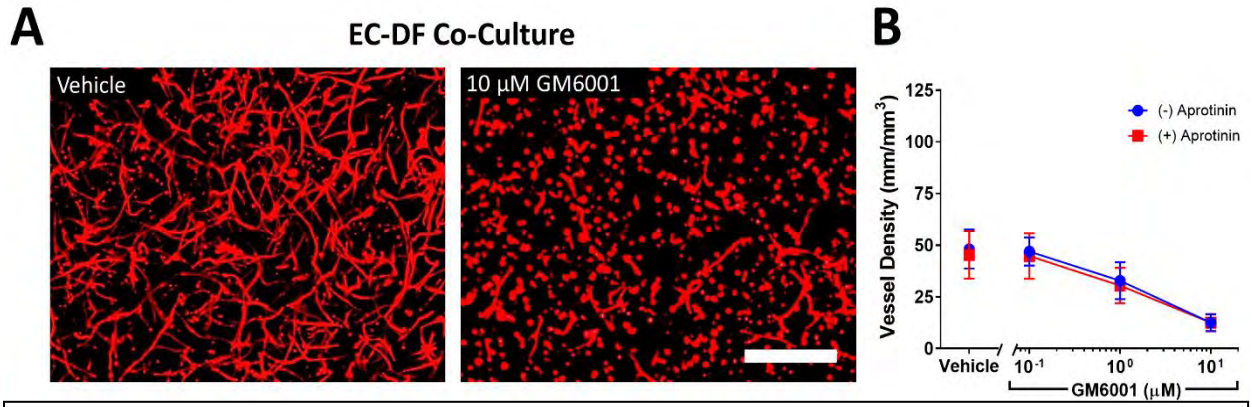

Figure 4.6: Cooperative GM6001 and aprotinin inhibition is abolished in VPMS crosslinked hydrogels. EC-DF co-cultures were generated in intermediate-crosslinked (32 mg/mL PEG-VS) hydrogels and cultured for 7 d in the presence of protease inhibitors GM6001 (concentration shown) or aprotinin (2.2 µM). Representative images stained with UEA (red) under indicated conditions are shown (A). Scale bar: 500 µm. Vessel density was quantified for each condition (B). Two-way ANOVA (GM6001, aprotinin, interaction) results: ($p < 0.0003$, $p = 0.21$, $p = 0.75$).

4.5 DISCUSSION

The goal of these studies was to implement a biomaterial engineering approach to investigate the relative importance of plasmin- and MMP-mediated matrix degradation in capillary morphogenesis. Our previous work has suggested that the identity of stromal cells used to support capillary morphogenesis influences the relative importance of MMP- and plasmin-

dependent matrix remodeling in fibrin (7, 101). These differences correlate with vessel function (7, 10, 11). Therefore, determining the relative roles of plasmin and MMPs in capillary morphogenesis may have critical implications for neovessel function and in the design of biomaterial scaffolds to support vascularization.

First, we investigated whether stromal-cell-dependent differences in the mechanism of proteolysis in fibrin hydrogels observed in angiogenesis models (7, 101) extended to a model of vasculogenesis. This model mimics vascularization strategies often deployed for tissue engineering applications that involve injection of populations of cells (11, 114) or pre-patterned cell aggregates (118, 209) that organize into microvasculature. The phenotype and angiogenic potential of microvascular ECs (98, 210) and stromal cells (7, 10, 11, 101, 211) vary widely according to their origin. We chose umbilical vein-derived ECs and supporting cells derived from bone marrow, lung, and dermis to explore in our model because our prior work has suggested differential utilization of MMP- and plasmin-mediated proteolysis with these combinations (7, 101). Furthermore, this EC source has been utilized widely for understanding mechanisms of capillary morphogenesis (212). Though we did not specifically test ECs from other origins, an essential role for MMPs in capillary morphogenesis has been described for microvascular (12, 213), macrovascular (7, 12), and stem cell-derived (98) ECs as has a role for plasmin with ECs derived from both macrovascular (7) and microvascular sources (58–61). As a result, we anticipate that programs of proteolytic remodeling implied by our investigation are likely generalizable to endothelium from a variety of origins.

For EC-fibroblast co-cultures in this model, we observed 1) a synergistic inhibition of capillary morphogenesis between aprotinin and high concentrations of GM6001 (≥ 10 μM) and 2) robust inhibition required both inhibitors. In contrast, GM6001 alone was sufficient to block

capillary morphogenesis in EC-MSC co-cultures. These results suggest that fibroblasts can induce a program of capillary morphogenesis that utilizes both MMP- and plasmin-dependent mechanisms of matrix remodeling consistent with our prior observations (7, 101). The observed IC50 for GM6001 for capillary morphogenesis, regardless of stromal cell identity, was approximately 1 μM. This level is at least two orders of magnitude greater than the IC50 for most MMPs (208), suggesting that inhibition of capillary morphogenesis, and thus any evidence of escape from MMP inhibition due to pericellular plasmin activity, does not occur until MMP activity is fully abolished. While it is possible the observed aprotinin-GM6001 synergy represents off-target effects from the single inhibitor used for each enzyme class in these studies, the fact that similar findings have been observed with a wide range of inhibitors for both MMPs and plasmin pathways in similar models (7, 55, 98, 101) suggests this explanation is unlikely. Together, these results suggest that plasmin can act as a pericellular protease only in circumstances in which the preferred MMP-dependent pathway is essentially inactivated, highlighting the essential role MMPs play.

To investigate the role of plasmin further, we designed synthetic PEG hydrogel ECMs (114, 127) in which matrix degradation was selectively limited to MMP- or plasmin-mediated mechanisms by crosslinking the scaffold with protease-selective peptides. We selected the peptide sequences VPMSMRGG (denoted VPMS), which can be degraded by a variety of MMPs (MT1-MMP and MMPs 1, 2, 3, 7, and 9) (214), support cell invasion (130), and support capillary morphogenesis (114) and YKNR, which is plasmin-sensitive and previously optimized for Michael addition reactions (132). Although this approach provides a selectively degradable ECM model, PEG-VS hydrogels lack many of the pro-angiogenic properties of fibrin, which include a fibrous architecture, macro-porous features, binding sites for multiple cell adhesion

molecules other than RGD, and binding sites for a variety of growth factors (215). Also, cells encapsulated in PEG-VS were never exposed to thrombin, which can activate endothelial cells, though the short duration of exposure in our study (30 min) leads to minimal EC activation (216) and is unlikely to have a meaningful impact over a 7 d culture period. Furthermore, soluble proteases may play an important role in cell-mediated degradation and migration in peptide crosslinked PEG-based hydrogels (217, 218). This property may restrict capillary morphogenesis, which requires membrane bound MT1-MMP in natural ECMs (12). Despite these limitations, capillary morphogenesis occurred in all VPMS-crosslinked hydrogels. However, a higher initial cell density was needed (targeted at the typical final cell density observed in fibrin gels) and the resulting capillary-like networks were never as extensive as in fibrin.

Initially, in formulations similar to our previous work (40 mg/mL) (114), we observed that spreading of both ECs and stromal cells was severely restricted in YKNR-crosslinked hydrogels. This observation is potentially explained by the fact that PEG-VS hydrogels have a nanoscale architecture with a mesh size on the order of 10-100 nm, in contrast to micron-scale pores in fibrin (219). As a result, the number of pericellular crosslinks that require degradation to permit cell spreading is at least 400 times greater in 40 mg/mL PEG-VS hydrogels compared with 2.5 mg/mL fibrin (estimated using the starting concentrations of each material, with 2 degradation events per PEG-VS molecule and 1 degradation event per fibrin molecule (220) needed for network dissolution). We also previously observed significant diffusion restrictions in these hydrogels for larger molecular weight molecules similar in size to plasminogen (114), which is supplied by serum and fibrinogen impurities in our vasculogenic culture system and is a necessary precursor to plasmin-mediated proteolysis.

To overcome these limitations, we generated PEG-VS matrices near the limits of gelation to reduce the number of pericellular crosslinks and minimize diffusion restrictions. In these loosely crosslinked YKNR hydrogels, we observed invasion of the surrounding matrix by fibroblasts. A persistent lack of spreading in control plasmin-insensitive Y_{D}-KN_{D}-R hydrogels confirmed cell spreading depended on degradation of the YKNR peptide. These observations indicated that limitations in vasculogenesis could be attributed to differences in the proteolytic preferences of endothelial cells rather than gross limitations in matrix degradability or plasminogen diffusion. This observation that plasmin-mediated degradation requires the PEG-VS hydrogel scaffold to be near the gelation point also may explain conflicting reports regarding the ability of fibroblasts to degrade YKNR crosslinked PEG hydrogels (132, 219). However, only in very loosely crosslinked YKNR hydrogels did we begin to observe occasional rudimentary vasculogenesis, which was never seen in similar soft control Y_{D}-KN_{D}-R hydrogels. In contrast, very soft control hydrogels crosslinked with VPMS tended to support more robust network formation, suggesting a correlation between MMP-degradability and vasculogenesis that highlights the dominant role of MMPs in capillary morphogenesis.

These findings are also consistent with other studies noting that increasing crosslink degradability (91) or a more loosely crosslinked network structure (221) correlate with increased capillary morphogenesis. Furthermore, in adipocyte-derived stem cell-EC cocultures, others have observed evidence that plasmin-mediated ECM degradation becomes increasingly important in densely crosslinked fibrin(62). Consequently, we hypothesized that plasmin may partially degrade the fibrin network rendering it more susceptible to MMPs and thus facilitating vasculogenesis. To evaluate this hypothesis, we generated PEG hydrogels where each crosslink was susceptible to either MMPs or plasmin by merging both the VPMS and YKNR peptides

sequences. These hydrogels were indistinguishable from VPMS-crosslinked controls, both in initial physical properties and in their ability to support capillary morphogenesis. These findings suggested that partial ECM-degradation by plasmin did not contribute significantly to capillary morphogenesis and that the kinetics of ECM remodeling were dominated by MMPs in our PEG-hydrogel co-culture system.

A possible explanation of the apparent role of plasmin-dependent pathways in fibrin hydrogels (based on inhibitor studies) but the failure of capillary morphogenesis in selectively plasmin-sensitive ECMs is that plasmin's role does not involve direct matrix degradation. Plasmin is a potent activator of MMP-3, which in turn activates MMP-9 to increase cellular invasiveness (222). If indirect plasmin-mediated activation of MMPs contributed to vasculogenesis, then we hypothesized that we should observe a synergy between aprotinin and GM6001 not only in fibrin but also in VPMS hydrogels. Moreover, the VPMS peptide is 8-times more sensitive to cleavage by MMP-9 than MT1-MMP (214), which is of critical importance in vessel formation (7, 55), making VPMS hydrogels an ideal environment to test this hypothesis. However, our experiments demonstrated no synergy between GM6001 and aprotinin in VPMS PEG-VS hydrogels, again highlighting the importance of MMPs alone.

There are several other possible explanations for the observed GM6001-aprotinin inhibition synergy in fibrin which we did not investigate further. Plasmin binding to $\alpha_v\beta_3$ on endothelial cells has been shown to induce endothelial migration (63), offering a potential alternative mechanism by which it may stimulate angiogenesis. Aprotinin also inhibits other serine proteases. Kallikrein, which is synthesized and secreted by ECs and cleaves kininogens into pro-angiogenic kinins (223), may also be present and inhibited at the concentration of aprotinin

utilized here (IC50 1-100 nM) (224) to reduce capillary morphogenesis under conditions of MMP inhibition.

Taken together, these results emphasize the utility of engineered ECM mimetics to better understand the mechanisms by which the ECM regulates complex morphogenetic programs in 3D. In particular, our results underscore the essential role for MMP-mediated ECM degradation during capillary morphogenesis and generalize the findings of prior studies in fibrin and collagen hydrogels (7, 12, 55, 56) to a precisely defined synthetic ECM. In contrast, our findings do not support a role for plasmin-mediated matrix remodeling in capillary morphogenesis, but instead suggest plasmin may contribute only under very limited circumstances (e.g. in fibrin with near complete MMP inhibition or in situations of supraphysiologic fibrin concentration (62)); such circumstances are unlikely to be physiologically significant. Our model also provides a tool to investigate matrix remodeling in organotypic capillary morphogenesis with specific EC and stromal cell combinations. Finally, the unique matrix-centric perspective of these studies provides strong evidence to justify the preferential selection of MMP-degradable peptide crosslinkers in synthetic hydrogels used to study vascular morphogenesis (69, 89, 91, 106, 221, 225–227) and promote vascularization.

4.6 SUPPLEMENTAL FIGURES

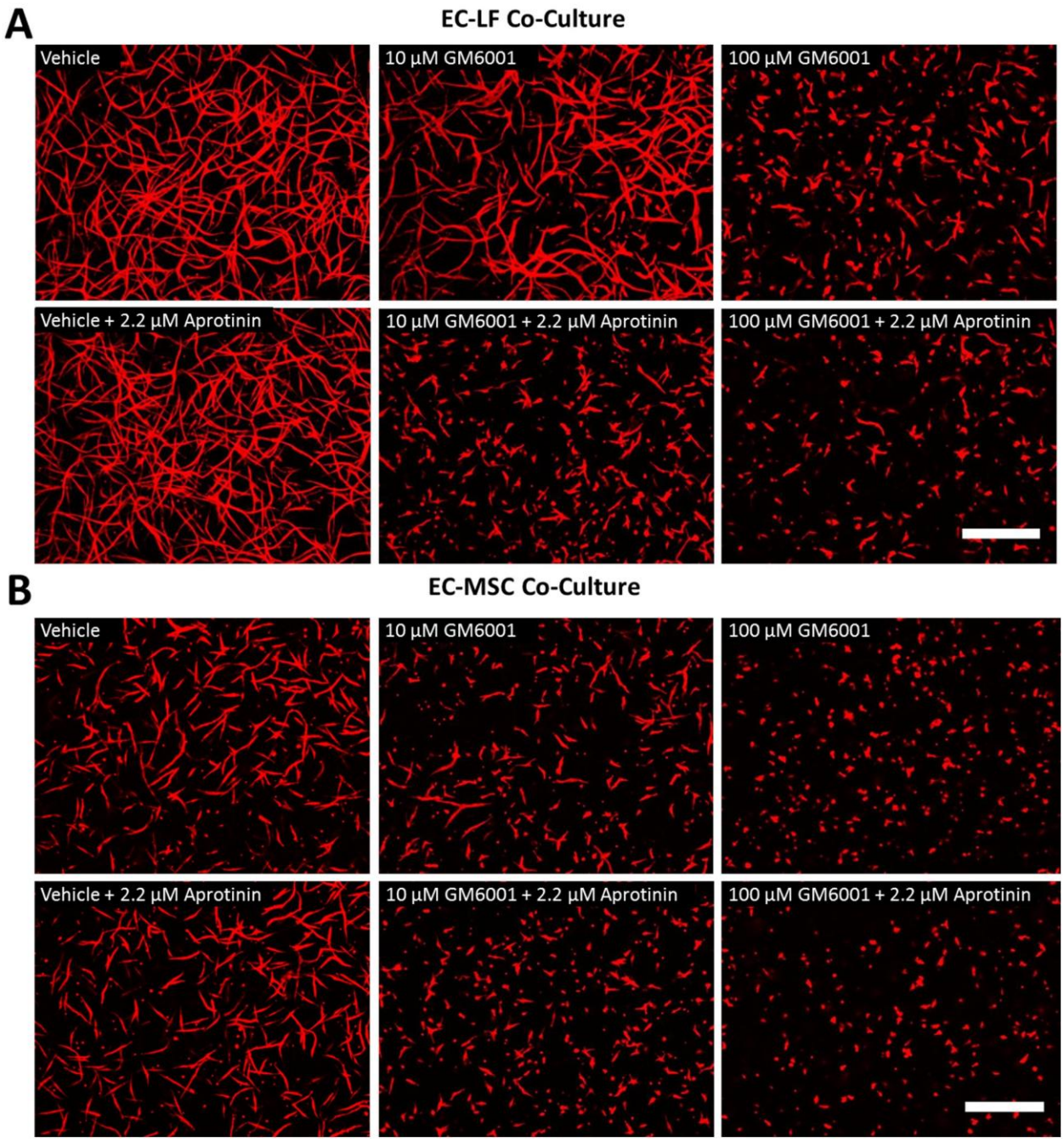

Figure 4.7: Representative images of capillary-like networks formed in EC-LF (A) or EC-MSC (B) co-cultures in 2.5 mg/mL fibrin at 7 d. Inhibitor concentrations are indicated, endothelial cells are shown stained with UEA (red) to highlight networks. Scale bar = 500 microns.

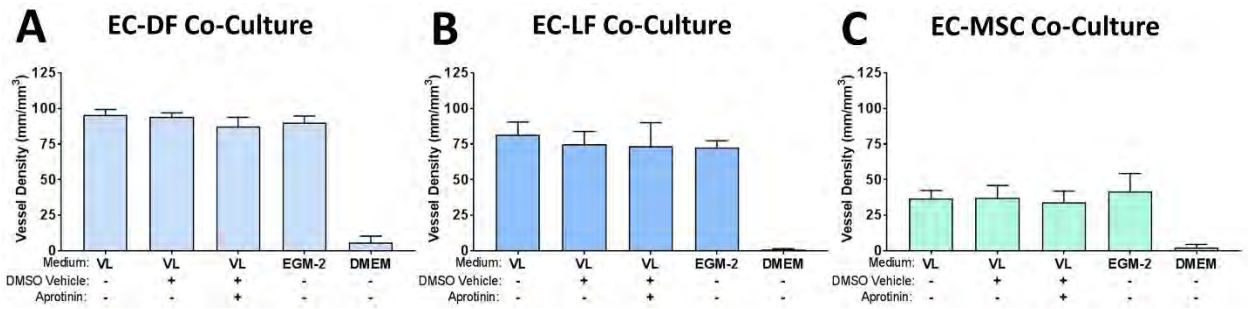

Figure 4.8: Vasculogenesis in fibrin hydrogels is equivalent in Vasculife VEGF (VL) and EGM-2 and is not affected by DMSO vehicle. Both types of vasculogenic culture medium were used for experiments (see methods). Shown are quantified network lengths for EC co-cultures with DFs (A), LFs (B), and MSCs (C) in 2.5 mg/mL fibrin after 7 d in culture. Vasculife medium with DMSO, with and without aprotinin, is replicated from Fig 1 for comparison. DMEM only, a non-vasculogenic medium, was used as a negative control for vasculogenesis.

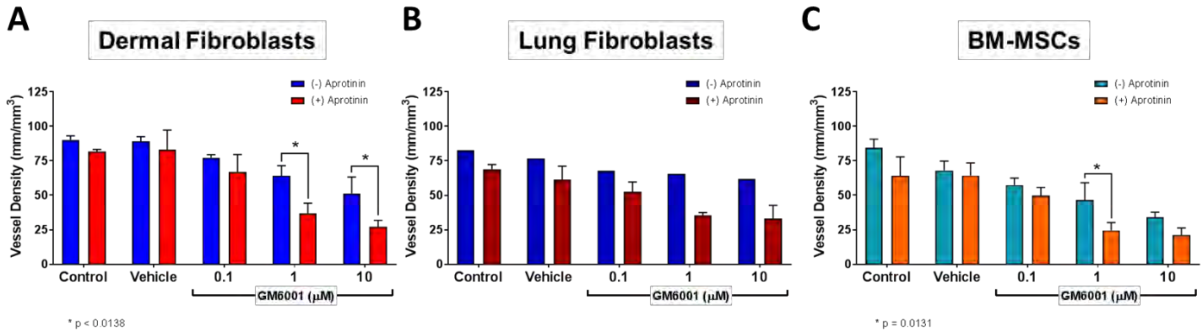

Figure 4.9: In serum free culture media, aprotinin acts synergistically with GM6001 to inhibit vasculogenesis in endothelial cell (EC) co-cultures with dermal fibroblasts (DFs), lung fibroblasts (LFs) and bone-marrow mesenchymal stem cells (MSCs) in 2.5 mg/mL fibrin hydrogels. Multiple images at prespecified locations were acquired for each condition for co-cultures of ECs and DFs (A), LFs (B), or MSCs (C) for 3 independent experiments and network lengths were quantified per volume as outlined in the methods. In 2 of 3 experiments, 3D fibrin constructs formed from lung fibroblasts completely degraded during the culture precluding quantification of vessel density but inclusion of aprotinin stabilized the constructs in all cases (B). *: $p < 0.05$ for specified conditions.

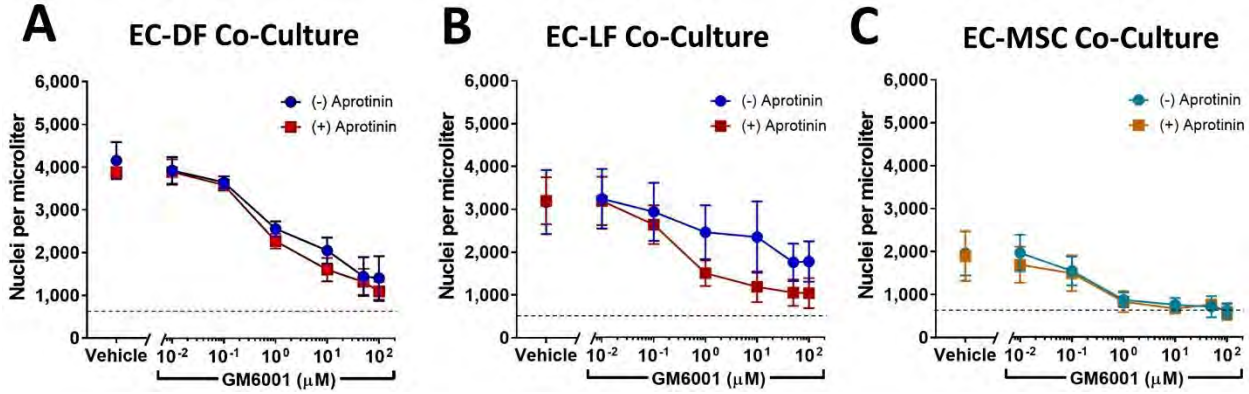

Figure 4.10: GM6001 cooperates with aprotinin to inhibit cell proliferation in a similar fashion as capillary morphogenesis. Multiple DAPI stained images at prespecified locations were acquired for each condition for co-cultures of ECs with DFs (A), LFs (B), and MSCs (C) for 3 independent experiments and the density of nuclei (as a measure of cell density) was quantified as outlined in the methods. Dotted line represents baseline nuclear density measured the day after seeding. Two-way ANOVA (GM6001, aprotinin, interaction) results: EC-DF ($p < 0.0001$, $p = 0.0301$, $p = 0.3718$), EC-LF ($p < 0.0001$, $p = 0.0405$, $p = 0.0003$), EC-MSC ($p < 0.0001$, $p = 0.0461$, $p = 0.1351$).

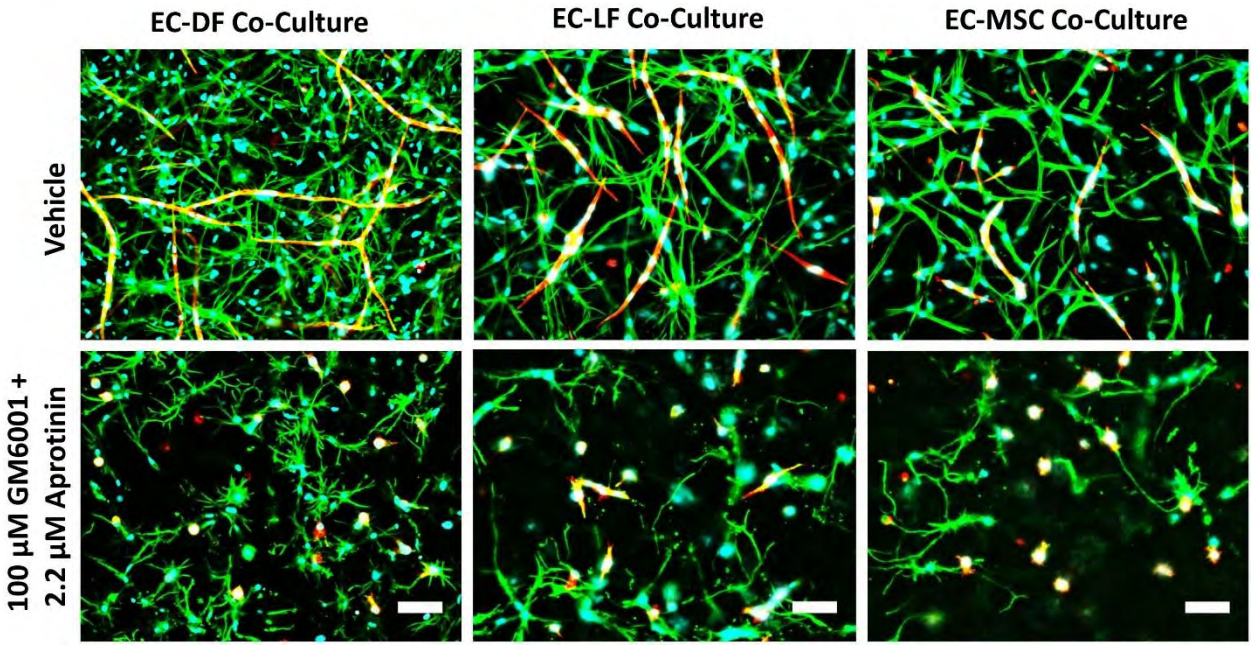

Figure 4.11: Dual inhibition with GM6001 and aprotinin severely attenuates, but never fully abolishes, stromal cell spreading in fibrin. Representative areas of EC co-cultures with DFs, LFs, and MSCs in 2.5 mg/mL fibrin are shown fixed at 7 d and stained with UEA (red), phalloidin (green) and DAPI (blue) with indicated inhibitors added. Stromal cells are phalloidin positive but UEA negative. Scale bars: 100 µm.

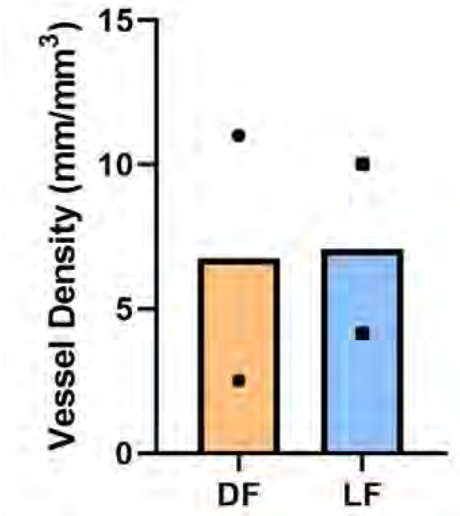

Figure 4.12: Capillary morphogenesis is equally restricted in 27 mg/mL YKNR hydrogels for EC-LF and EC-DF cocultures. Vessel network length was quantified on day 7 in each scaffold as defined in the methods. Results from 2 replicates and their mean value are shown from matched cultures of EC-DF and EC-LF in which EC pellets and hydrogel formulations were identical.

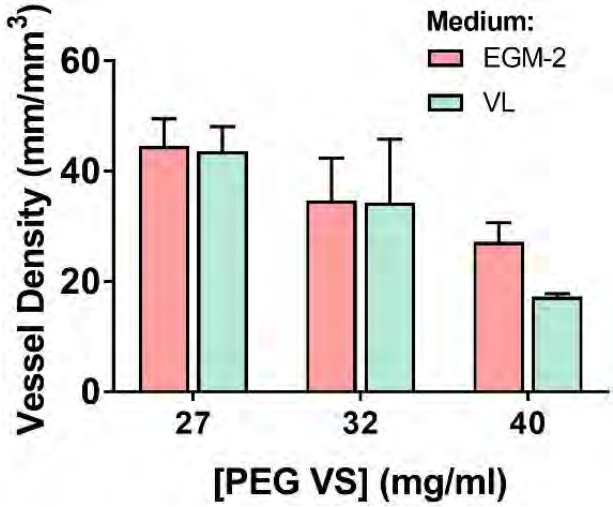

Fig 4.13: Capillary morphogenesis in VPMS-PEG-VS hydrogels did not depend on vasculogenic medium used. Vessel density was quantified in PEG-VS scaffolds with the indicated composition crosslinked with VPMS peptide then cultured for 7 d in either EGM-2 or Vasculife VEGF (VL) medium. No significant differences (N = 3) were noted comparing each medium in the same hydrogel composition (ANOVA media effect: $p = 0.23$, Tukey post hoc analysis for 40 mg/ml PEG-VS EGM-2 vs. VL: $p = 0.73$). We noted increased capillary morphogenesis in 27 mg/ml PEG-VS hydrogels compared with 40 mg/ml hydrogels regardless of medium used (Tukey post hoc analysis for 27 vs 40 mg/mL PEG-VS in the same medium: $p < 0.036$).

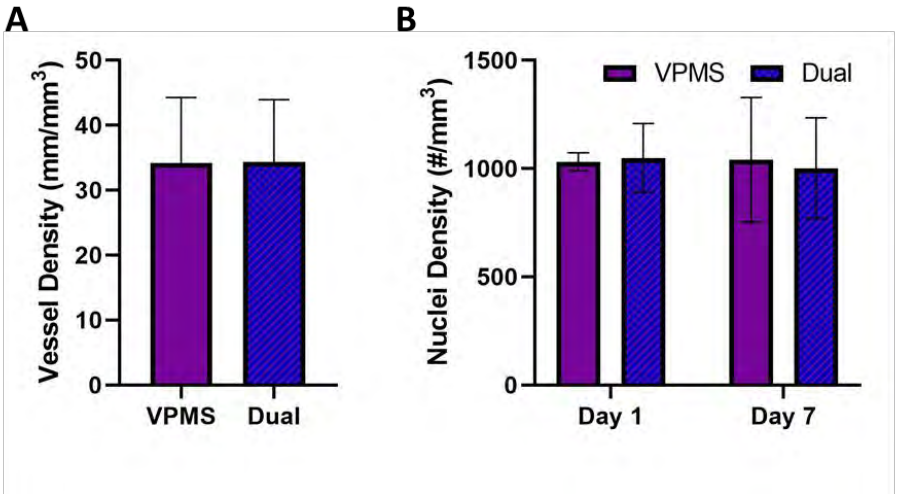

Fig 4.14 EC-LF cocultures demonstrate similar behavior as EC-DF cocultures with no enhancement of capillary morphogenesis in dual sensitive hydrogels. PEG-VS hydrogels were crosslinked with a concatenated peptide containing both VPMS and YKNR sequences and used to form scaffolds in which each crosslink was susceptible to either MMPs or plasmin. EC-LF co-cultures were generated in intermediate-crosslinked (32 mg/mL PEG-VS) scaffolds crosslinked with either VPMS or dual-susceptible peptides. Vessel density, quantified after 7 d, was similar for VPMS and dual susceptible peptides (A). There were no differences in cell density on d1 or after 7 d, measured by automated counting of DAPI stained nuclei per volume (B).

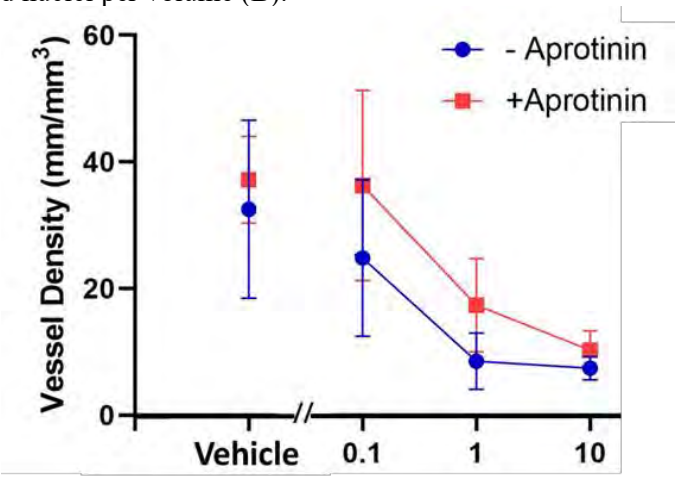

Figure 4.15: EC-LF cocultures do not exhibit cooperative GM6001 and aprotinin inhibition in VPMS crosslinked hydrogels. EC-LF co-cultures were generated in intermediate-crosslinked (32 mg/mL PEG-VS) hydrogels and cultured for 7 d in the presence of protease inhibitors GM6001 (concentration shown) or aprotinin (2.2 μM). Vessel density was quantified for each condition.Two-way ANOVA (GM6001, aprotinin, interaction) results: ($p < 0.0001$, $p = 0.081$, $p = 0.855$).

CHAPTER V

Enhanced Proteolytic Susceptibility Of Matrix Metalloproteinase-Selective Poly(Ethylene Glycol) Hydrogels Increases Capillary Network Formation.

5.1 ABSTRACT

Matrix metalloproteinase-mediated extracellular matrix (ECM) remodeling is essential for capillary morphogenesis. Here we employed poly(ethylene glycol) (PEG) based hydrogels engineered with varying MMP-mediated proteolytic susceptibility to investigate the effect of hydrogel degradability on capillary self-assembly in a 3D cell culture model analogous to vasculogenesis. We first demonstrated that incorporating a double repeat of the protease recognition sequence in the hydrogel crosslinker resulted in enhanced proteolytic susceptibility without affecting initial hydrogel mechanical properties. We then demonstrated that enhanced proteolytic susceptibility resulted in increased capillary network density after 8 days in culture but was not associated with a significant difference in total nuclei density depending on crosslink identity. Both hydrogel formulations exhibited hydrogel stiffening during culture, with a higher degree of stiffening associated with enhanced proteolytic susceptibility. A preliminary study of hydrogels implanted subcutaneously suggested that enhanced proteolytic susceptibility may also facilitate morphogenesis *in vivo* but is severely restricted compared to *in vitro* culture. Histological sectioning suggested minimal host infiltration in acellular hydrogels, and possible fibrous capsule formation at the hydrogel-tissue interface. These findings contribute to a fundamental understanding of the effect of proteolytic remodeling on capillary morphogenesis in

PEG hydrogels, and provide a convenient means of enhancing capillary morphogenesis in tissue engineering applications that require rapid tissue construct vascularization.

5.2 INTRODUCTION

Systematically characterizing the influence of synthetic scaffold properties on cellular phenotypic responses helps provide insights into factors that regulate capillary morphogenesis and techniques for improving vascularization of tissue constructs. This chapter specifically investigates how the susceptibility of poly(ethylene glycol) (PEG)-based hydrogels to matrix-metalloproteinase (MMP)-mediated proteolysis affects the rate at which vessels self-assemble. Increasing extracellular matrix density in tissue constructs effectively results in decreased degradability and typically correlates with decreased vessel formation in natural (176, 196, 228), semi-synthetic (202, 229, 230), and synthetic hydrogels (91, 114, 133, 221). Moreover, MMP inhibition is known to inhibit capillary morphogenesis in a dose dependent manner in both natural and synthetic hydrogels (7, 231). Together, these studies suggest proteolytic activity and matrix degradability are key regulators of vessel invasiveness. Changing the concentration of ECM, however, results in concomitant changes in diffusive transport (114, 176), matrix stiffness (64), and ligand presentation (196) and inhibitor studies may have off target effects. These numerous convolutions make PEG-based hydrogels appealing because the rate of degradation can be altered by changing the crosslink identity without affecting other matrix properties.

We have previously assessed the effect of proteolytic selectivity on capillary self-assembly in PEG hydrogels (12), but we have not directly addressed whether modulating PEG-hydrogel degradability to MMPs affects vessel formation. Other groups have demonstrated that matrix degradability affects the rate of cellular invasion (91) as well as the multicellularity of EC invasion (89) in synthetic hydrogels, but the effect of matrix degradability on vessel formation in

a vasculogenic model of capillary self-assembly has not been investigated. We compared 2 distinct proteolytically degradable crosslinkers; a commonly used MMP-sensitive crosslinker termed "VPMS" (114, 123, 130, 231) and a double repeat of the protease recognition sequence to enhance hydrogel degradability. Although this changes the crosslink length, it is negligible compared to the length of the arms of the PEG molecules. Including multiple repeats of the protease recognition sequence in the peptide crosslinker in a similar hydrogel system has previously been shown to increase proteolytic degradability without affecting hydrogel swelling, mesh size, or compressive modulus (91). In addition to quantifying differences in vessel formation depending on crosslink identity, cellular proliferation and change in hydrogel mechanics over time was also quantified. Furthermore, morphogenetic behavior *in vitro* was compared to an *in vivo* subcutaneous implant model.

5.3 MATERIALS AND METHODS

5.3.1 Cell culture

Human umbilical vein endothelial cells (ECs) were harvested from fresh umbilical cords and cultured in fully supplemented EGM2 (Lonza, Walkersville, MD) as previously described (172)[15]. ECs were used between passages 2-4. Normal human dermal fibroblasts (DFs, Lonza) were cultured in Dulbecco's modified eagle medium (DMEM) supplemented with 10% fetal bovine serum (FBS) and 1% penicillin streptomycin and were used up to passage 15. Both cell types were cultured at 37 ºC and 5% CO_2 with thrice weekly medium exchange.

5.3.2 PEG-VS hydrogel formation

Hydrogels were formed from 4-arm poly(ethylene glycol) vinyl sulfone (PEG-VS; 20 kDa, Jenkem USA, Allen TX) and a combination of thiol containing adhesive and protease-sensitive peptides adapted from published protocols (114, 127)[14,19]. All reagents were prepared in

batches of single-use aliquots. To minimize variability between experiments, all hydrogels presented within this chapter were formed from identical aliquots from single batches of PEG-VS and peptides. Peptides, dissolved in 25 mM acetic acid, and PEG-VS, dissolved in ultrapure water, were 0.22 μm filtered, lyophilized, and stored desiccated at -20 ºC. Precise thiol content of each batch of peptide aliquots was determined using Ellman's reagent. An optimal thiol:vinyl sulfone ratio which yielded a hydrogel shear modulus of 200 Pa for acellular hydrogels was determined for each crosslinking peptide. Immediately before use, PEG-VS was dissolved in HEPES (100 mM, pH 8.4) to achieve a final concentration in formed hydrogels of 30 mg/ml PEG-VS and CGRGDS peptide (RGD, Genscript, Piscataway, NJ) was reacted with the PEG-VS for 30 min to acheive a final concentration of 500 μM. In rapid succession, dithiol crosslinking peptides at the optimized thiol:vinyl sulfone ratio (accounting for RGD conjugation) were added to the PEG-VS solution, gently mixed, and 50 μl of precursor solution was dispensed into a sterile 1 mL syringe with the needle end cut off, and allowed to polymerize for 1 h at 37 ºC in a sealed 50 mL conical tube.

Crosslinking peptides included: Ac-GCRDVPMS↓MRGGDRCG-NH2 ("VPMS") and Ac-GCRDVPMS↓MRGGVPMS↓MRGGDRCG-NH2 ("2xVPMS") each containing an N-terminal acetylation and a C-terminal amidation (Genscript, cleavage sites indicated by ↓). Polymerized hydrogels were punched into culture medium or phosphate buffered saline (PBS).

5.3.3 Mechanical and proteolytic characterization of PEG-VS hydrogels

Hydrogels were allowed to swell overnight, then were mounted on an AR-G2 rheometer (TA Instruments, New Castle, DE) between an 8-mm measurement head and a Peltier stage, each covered with P800 sandpaper. Shear storage modulus (G') was determined at 0.05 N normal force, 5% strain amplitude, and 1 Hz frequency and averaged over a 1-minute time sweep. For

proteolysis experiments, hydrogels were allowed to swell overnight then transferred to 1 U/mL collagenase IV from *Clostridium histolyticum* (used as a qualitative surrogate for MMP degradation as both MMPs and collagenase IV can degrade the VPMS peptide sequence) in PBS supplemented with 0.4 mM $CaCl_2$ and 0.1 mM $MgCl_2$. The shear modulus of hydrogels were measured at 0, 1.5, and 3 h to determine differences in degradation depending on crosslinking peptide.

5.3.4 *In vitro* vasculogenesis assay

Hydrogels were formed as above except that a cell pellet was resuspended in the crosslinking peptide precursor solution immediately before mixing with PEG-VS solution to achieve a final cell density of $5x10^6$ cells/mL of each cell type. VPMS and 2xVPMS replicates were paired to receive identical cell pellets.50 µl samples of the resulting suspension was then dispensed into 1 mL syringes and polymerized as above for 1 hour. Hydrogels were then punched out into 2 mL of Vasculife VEGF medium in a 24-well plate. Media was exchanged on day 1 then on alternate days thereafter for 8 days. At the end of the experiment, *in vitro* hydrogel co-cultures were fixed with Z-fix (Anatech, Battle Creek, MI) for 1 hr, rinsed 4x in PBS, and then stored at 4 °C.

5.3.5 *In vivo* subcutaneous implant model

All animal procedures were performed in accordance with the National Institutes of Health (NIH) guidelines for laboratory animal usage and approved by the University of Michigan's, Institutional Animal Care and Use Committee. Male CB17/SCID mice (6–8 weeks old; Taconic Labs, Hudson, NY) were used for all experiments. Mice were anesthetized in an induction chamber with 5% isoflurane at 1 L/min O2 (Cryogenic Gases, Detroit, MI) using a V-1 Tabletop isoflurane vaporizer system equipped with an Active Scavenging Unit (VetEquipt,

Livermore, CA). Once mice were fully anesthetized, they were moved to the surgical bench and fitted with an active scavenging nose cone with the isoflurane level reduced to 1%. Carprofen (5mg/kg) was administered to each animal prior to surgery and 24 hrs post-surgery via subcutaneous injection. The dorsal flanks of each mouse were shaved and depilatory agent (Nair; Thermo Fisher Scientific, Pittsburg, PA) was applied to remove any remaining hair. The surgical site was then sterilized with three alternating applications of ethanol and betadine (Thermo Fisher Scientific, Fremont, CA).

Once animals were prepared for surgery, hydrogels to be implanted were retrieved from the incubator. Implanted hydrogels were paired with identical hydrogels cultured in *in vitro* assays for direct comparison of morphogenetic behavior. Each mouse received 2 implants: paired 2xVPMS and VPMS hydrogels with identical cell pellets. Hydrogels were implanted intact after 1 day in Vasculife VEGF medium. Two incisions were made on either side of the dorsal flank approximately 1 cm wide and a subcutaneous pocket approximately 2 cm deep was created. The hydrogel was then inserted into the subcutaneous pocket while being careful not to trap any air. The surgical incision was then closed with non-absorbable sutures. Animals were euthanized on day 7 (8 days after hydrogel formation) by CO_2 overdose and hydrogels were retrieved via gross dissection with adherent adjacent skin and muscle layers intact. Hydrogels were immediately fixed for 4 hours in Z-fix, and then moved to a 10x dilution of Z-fix in PBS overnight at 4 °C. Samples were then washed 4x in PBS and stored in 70% ethanol at 4 °C.

5.3.6 Fluorescent imaging and quantification methods

Imaging and analysis of *in vitro* hydrogels and whole-mount imaged *ex vivo* samples were performed identically. All PEG-VS hydrogels were cut down the cylinder diameter prior to staining, yielding two halves. Samples were stained with rhodamine-conjugated lectin from *Ulex*

europaeus (UEA, Vector Laboratories, Burlingame, CA, specific for endothelial cells, 1:200), 4', 6-diamidino-2-phenylindol (DAPI, 1 μg/ml, Sigma), and AlexaFluor 488 phalloidin (1:200). PEG-hydrogels were imaged on the cut side to ensure images were representative of cellular behavior within the hydrogels. Images were acquired using an Olympus IX81 microscope equipped with a disk scanning unit (DSU, Olympus America, Center Valley, PA) and Metamorph Premier software (Molecular Devices, Sunnyvale, CA). For all analyses, confocal z-stacks were acquired using the DSU. Z-series were collapsed into maximum intensity projections prior to analysis. Quantifications of vessel and nuclei densities were performed on 200 μm stacks (50 μm/slice) imaged at 4x. Total vessel length per region of interest (ROI) was quantified using the Angiogenesis Tube Formation module in Metamorph and reported as vessel length per volume of ROI (2.16 x 1.65 x 0.3 mm). Total nuclei per ROI was quantified using a custom ImageJ script (included in appendix).

5.3.7 Histological sectioning and staining

Excess tissue was removed from implants, and samples were placed in embedding cassettes (UNISETTE cassette with lid; Simport, Beloeli, QC, Canada), dehydrated, and embedded in paraffin using a KD-BMII tissue embedding center (IHCWorld, Ellicott City, MD). Samples were oriented such that the cutaneous layer would be sectioned first. Sections 10 μm thick of embedded samples were then generated with a Thermo Fisher Scientific HM 325 rotary microtome and placed on glass slides. Paraffin sections on glass slides were dewaxed in xylene baths twice for 5 min and then washed in progressively decreasing concentrations of ethanol solution. Slides were then rehydrated in deionized water and stained with Mayer's hematoxylin (Electron Microscopy Sciences, Hatfield, PA) and Eosin Y (Sigma-Aldrich) as previously described (109). Toluene mounting solution (Permount; Thermo Fisher Scientific) was added to

coverslips before placing on top of each slide. Slides were left to dry before imaging. After staining, slides were imaged using an Olympus IX81 microscope with a DP2-Twain color camera (Olympus America, Center Valley, PA) and the CellSens Imagining Software (Olympus).

5.3.8 Statistics

Statistical analysis was performed using GraphPAD Prism (La Jolla, CA). Unless noted, data are represented as mean ± standard deviation of at least 3 independent experiments. Data were analyzed using one- or two-way ANOVA with Sidak post-hoc testing for pre-specified comparisons. A value of $\alpha < 0.05$ was considered significant.

5.4 RESULTS

5.4.1 Enhanced hydrogel degradability accelerates vessel formation *in vitro*

We first optimized our hydrogel formulations to produce acellular hydrogels with shear moduli of ~200 Pa and assessed differences in proteolytic degradation depending on crosslink

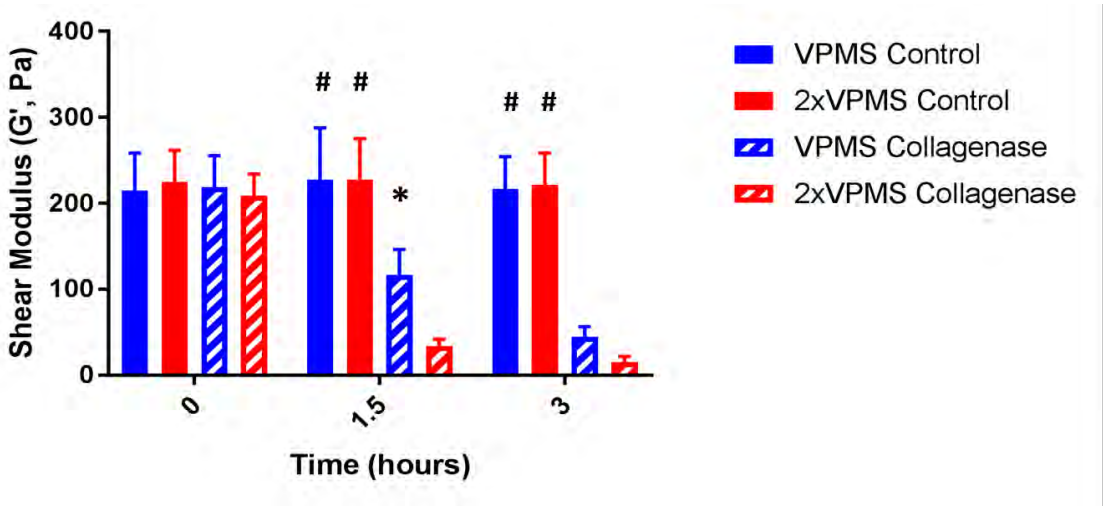

Figure 5.1: 2xVPMS hydrogels have increased proteolytic susceptibility compared to VPMS hydrogels. Hydrogels were crosslinked, swollen in PBS overnight, exposed to collagenase (1 U/mL), and at indicated times, characterized by shear rheology. Hydrogels crosslinked with either peptide were readily degradable as measured by shear rheology. #: $p < 0.05$ relative to collagenase treatment (same peptide and time point). *: $p < 0.05$ compared with 2xVPMS peptide (same treatment and time point). N = 3

identity. Hydrogels crosslinked with either peptide showed significant decreases in shear modulus over time when incubated with collagenase, indicating hydrogel degradation (**Fig 5.1**). Hydrogels crosslinked with 2xVPMS had significantly lower shear moduli than VPMS hydrogels at 1.5 hrs, indicating accelerated degradation (**Fig 5.1**).

Acellular hydrogel formulations yielding ~200 Pa hydrogels were chosen to account for a significant drop in hydrogel shear modulus to ~100 Pa with incorporation of cell pellets (**Fig 5.2 A**). Cellular hydrogels with ~100 Pa shear moduli were empirically targeted to minimize modulus, which facilitates vessel formation, while still maintaining enough integrity to handle for surgical implantation.

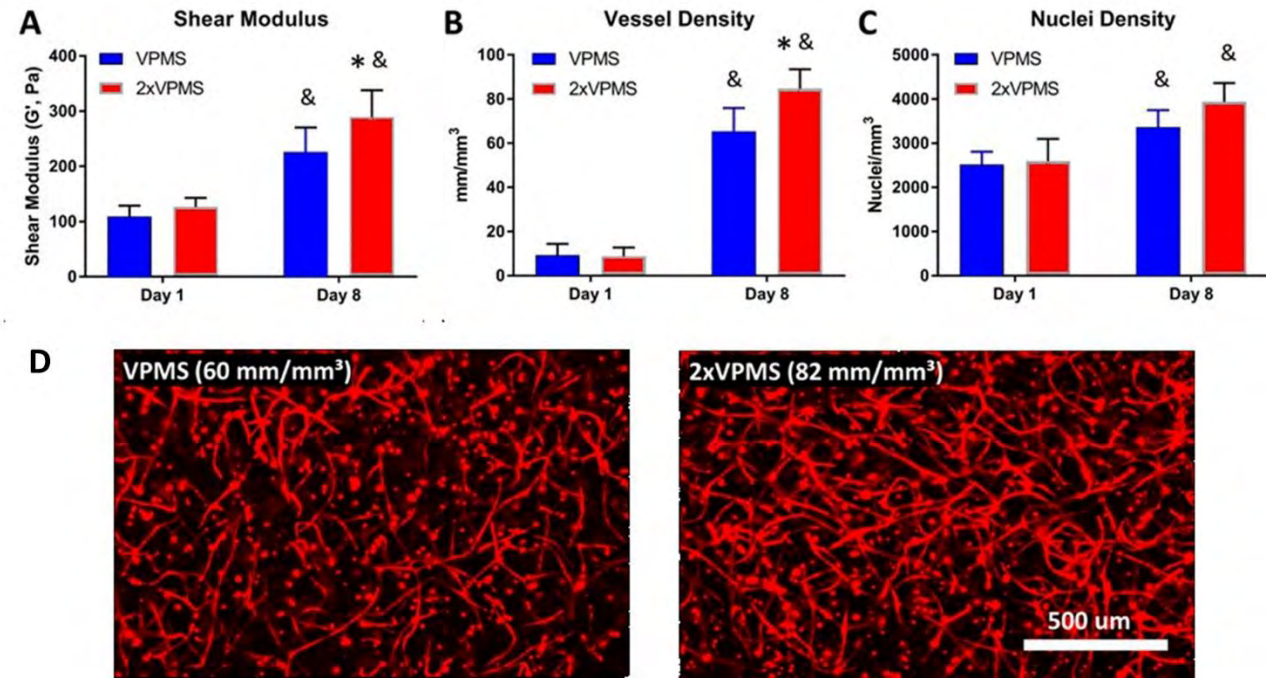

Figure 5.2: Enhanced crosslink proteolytic susceptibility results in increased vessel density. Cellular hydrogel constructs were formed with either VPMS or 2xVPMS crosslinkers and cultured for 8 days. A) The shear storage modulus (*G'*) of constructs was determined after overnight culture (day 1) and on day 8. B) Vessel density in the bulk of the constructs was estimated as described in the methods. C) Cell density in the constructs on day 1 and day 8 was quantified from DAPI stained images. D) Representative images of maximum intensity projections of confocal sections (z height = 200 µm) for ECs stained with UEA (red) on Day 8 from constructs formed with either crosslinker (vessel density of specific image is shown). *: $p < 0.05$, relative to VPMS (same day); &: $p < 0.01$ relative to day 1 (same crosslinker), N = 5.

Vessel density significantly increased over time for both VPMS and 2xVPMS hydrogels, with a significantly higher average vessel density in 2xVPMS hydrogels (85 ± 8 mm/mm³) compared to VPMS hydrogels (65 ± 11 mm/mm³) on day 8 (**Fig 5.2 B**). The overall nuclei density for both VPMS and 2xVPMS hydrogels also significantly increased over time, but no significant difference was observed depending on crosslink identity (**Fig 5.2 C**). Representative images of near average vessel formation are shown in **Fig 5.2 D**, with quantification of the vessel density for each specific image shown, to qualitatively illustrate the differences in vessel formation observed.

5.4.2 Enhanced hydrogel degradability improves vessel formation and cell spreading in subcutaneous implants, but morphogenesis is severely restricted compared to *in vitro*.

In a preliminary study, intact hydrogels were implanted in subcutaneous pockets on the dorsal flank of 6-8 week old CB17-SCID mice to assess whether differences in hydrogel degradability affected cellular morphogenesis *in vivo*. An example of the surgical site and implants immediately after surgery is shown in **Fig 5.3 A**. Overall cell spreading and vessel formation was qualitatively assessed by whole mount confocal imaging of UEA, DAPI, and phalloidin stained explants and compared to paired *in vitro* samples (**Fig 5.3 B**). Subcutaneous implants demonstrated some degree of vessel formation as indicated by elongated UEA-positive cells, and fibroblast cell spreading as indicated by UEA-negative phalloidin stained cells. Cell spreading and vessel formation in implants appeared more pronounced in 2xVPMS hydrogels compared to VPMS hydrogels but neither condition supported the robust interconnected network formation observed in *in vitro* culture for either type of hydrogel (**Fig 5.3 B**).

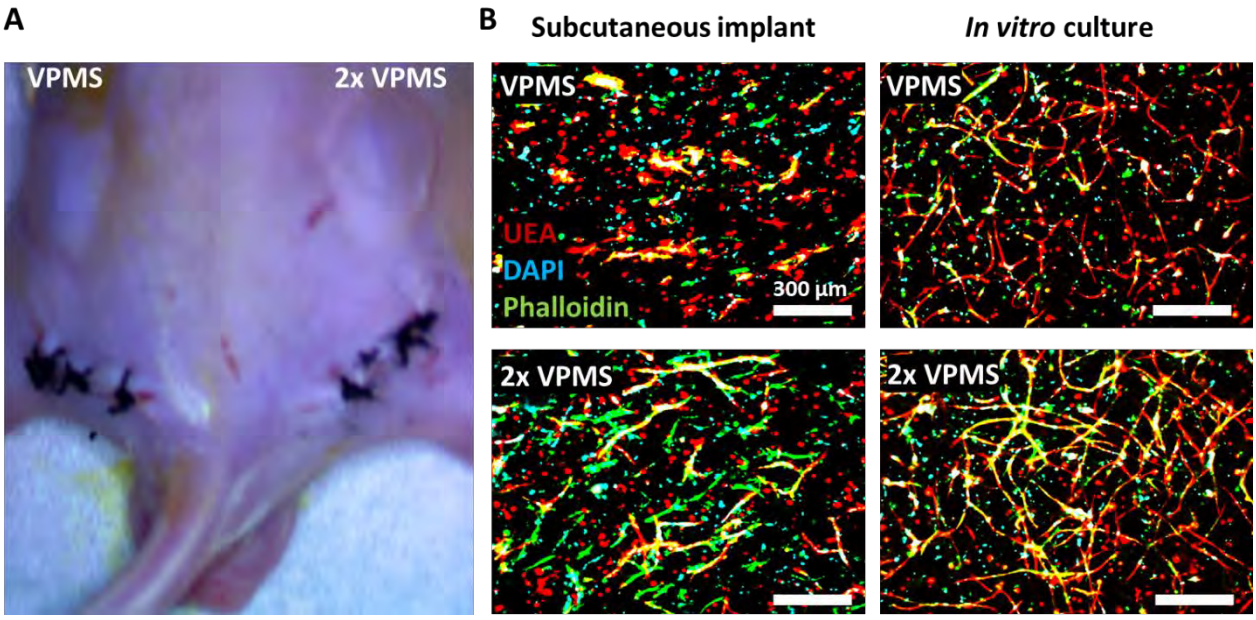

Figure 5.3: Enhanced hydrogel degradability improves vessel formation and cell spreading in subcutaneous implants, but morphogenesis is severely restricted compared to *in vitro*. Paired VPMS and 2xVPMS hydrogels were either implanted subcutaneously on day 1 for 7 days or cultured *in vitro* for 8 days. A) The surgical site immediately after hydrogel implantation. B) Representative images of maximum intensity projections of confocal sections (z height = 200 µm) for ECs stained with UEA (red), all nuclei stained with DAPI (cyan) and cell bodies stained with phalloidin (green) with comparison between paired hydrogels. N = 1.

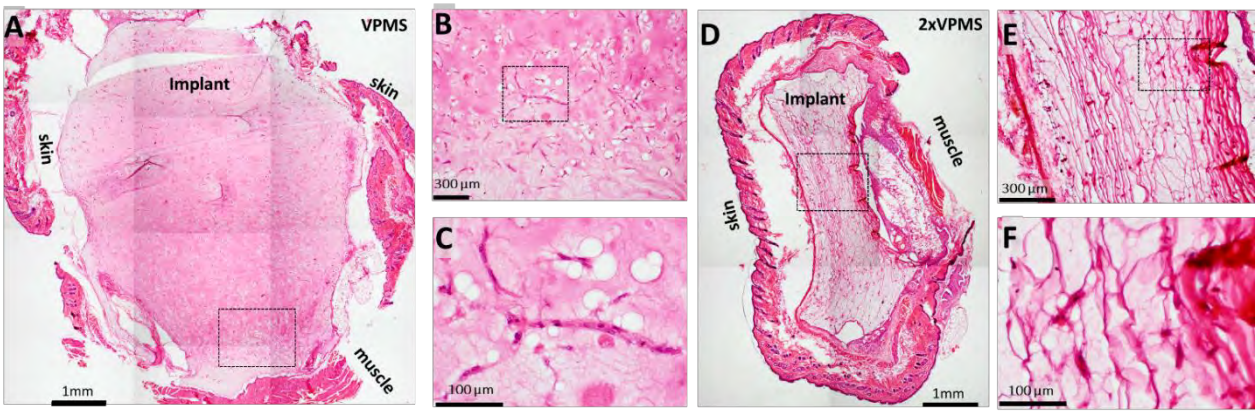

Figure 5.4: Cell spreading and vessel-like structures appear in H &E stained explant sections, but variable hydrogel collapse during processing precluded comparison depending on crosslinker. Paired explants were paraffin embedded, sectioned (10 µm thick) and stained with hematoxylin and eosin (H&E). Cell spreading and vessel-like structures were evident in the VPMS explant (A-C). Hydrogel collapse of the 2xVPMS explant (D-F) during paraffin embedding was evident macroscopically (D) and microscopically (E, F) distorting cellular structures (F). Progressive insets are outlined by dashed boxes for A, B, & C and for D, E, & F. Insets B and E have different digital magnifications.

In addition to whole mount imaging, cell spreading and formation of vessel-like structures was assessed with hematoxylin and eosin (H&E) stained sections of paraffin embedded explants (**Fig 5.4**). Some degree of cell spreading and vessel formation was evident throughout explant sections (**Fig 5.4 A-C**), as was seen in whole mount imaged explants (**Fig 5.3 B**). No evidence of red blood cells, indicative of inosculation with the host, was observed within the hydrogel implant. Hydrogel collapse of the 2xVPMS hydrogel (**Fig 5.4 D-F**) precluded comparison depending on crosslink identity. Hydrogel collapse was apparent from the macroscopic shape change of implant (**Fig 5.4 D**) and microscopic banding patterns (**Fig 5.4 E,F**). The macroscopic shape change and banding patterns were observed on sections throughout the thickness of the sample, indicating collapse occurred during dehydration and embedding rather than during sectioning (**data not shown**).

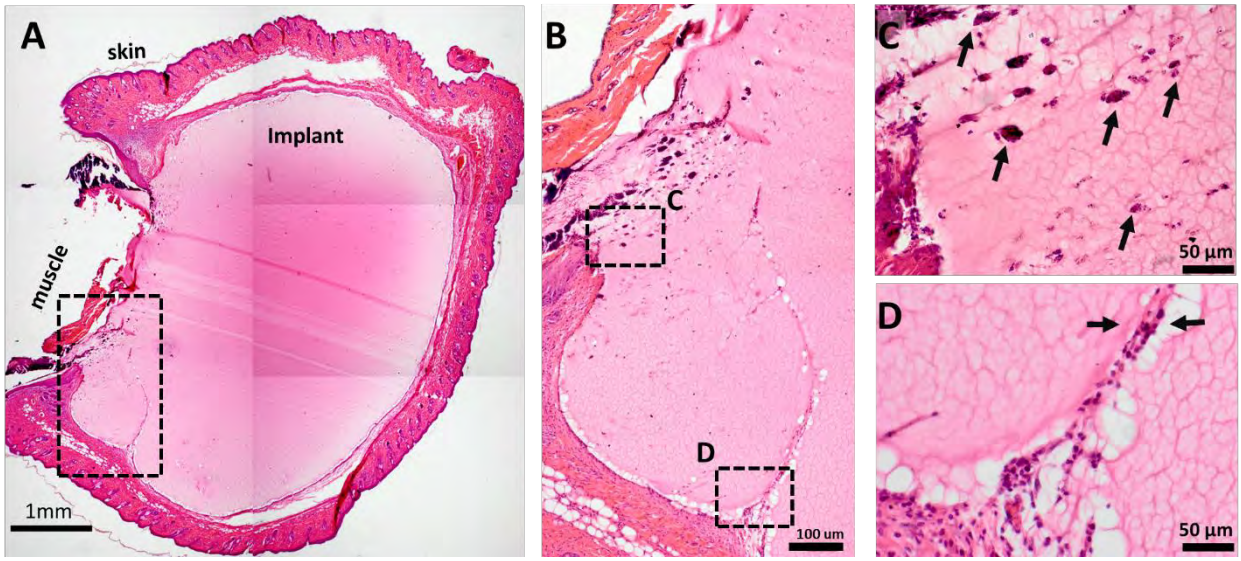

Figure 5.5: Minimal host infiltration is observed in an acellular VPMS implant. The acellular explant was paraffin embedded, sectioned (10 µm thick) and stained with hematoxylin and eosin (H&E). A) The implant appears largely devoid of cell bodies except for a single cellular protrusion from the skin and some infiltrating basophilic cells near the muscle. The region of the implant containing cellular infiltration is shown in (B), with cells indicated with black arrows in (C) and (D). Progressive insets are indicated with dashed boxes, the respective insets of (B) are indicated.

Histological assessment of an H&E stained acellular VPMS implant indicated minimal host cell invasion during the 7 days implanted (**Fig 5.5**). Coincidently, processing artifacts of the paired 2xVPMS acellular hydrogel precluded its assessment as occurred for the cellular hydrogel (**data not shown**). The implant appeared largely devoid of cellular infiltrate except for isolated highly basophilic cell bodies near the muscle (**Fig 5.5 A-**C) and a single continuous cellular protrusion emanating from the skin (**Fig 5.5 A, B, D**).

An eosinophilic layer with high cell density between the implant and host tissue was observed in some histological sections indicating a fibrous capsule may be forming (**Fig 5.6**). This capsule-like structure was not apparent in all sections, but occurred in sections of both acellular and cellular hydrogels. When observed, the capsule-like structure appeared most prominent adjacent to intact muscle (**data not shown**).

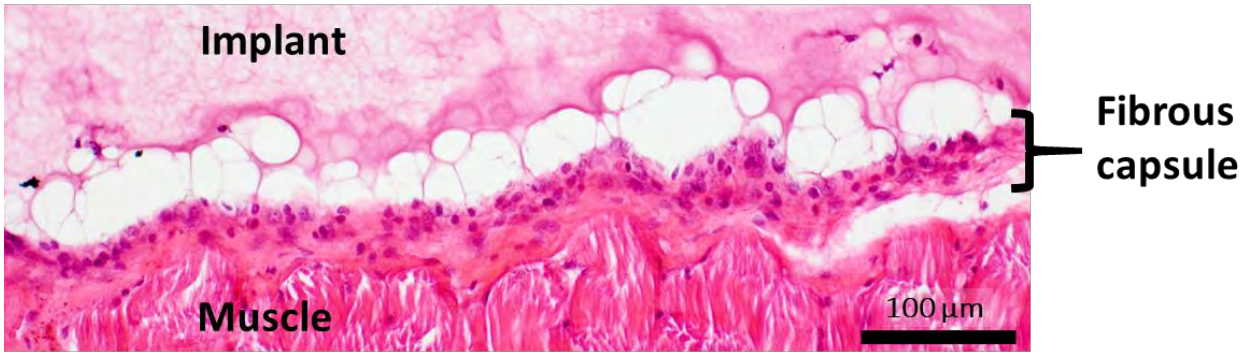

Figure 5.6: Possible fibrous capsule formation around hydrogel implants. In some paraffin embedded, hematoxylin and eosin (H&E) stained sections, an eosinophilic layer with high cell density between the implant and host tissue suggested potential fibrous capsule formation.

5.5 DISCUSSION

These results demonstrate that increasing the proteolytic susceptibility of PEG-based hydrogels by incorporating multiple repeats of a proteolytic recognition sequence into the peptide crosslinker is a convenient means of increasing vascular network self-assembly. These

results are broadly applicable to tissue engineering applications in which acceleration of morphogenetic processes in peptide-crosslinked hydrogels is desirable. Proposed applications of similar synthetic hydrogels which may benefit from accelerated morphogenesis of encapsulated cells include the repair of brain tissue following stroke (232), cardiac repair following ischemia reperfusion (233), fabrication of tissue engineered heart valves (234), revascularization of ischemic tissue (235), and to enhance angiogenic ingrowth of therapeutic organoids (121).

Incorporating multiple repeats of the proteolytic recognition sequence is not expected to significantly alter the hydrogel network structure. The VPMS crosslinker contains 16 residues compared to 24 residues for 2xVPMS. The contour length of a peptide in solution is approximately 4 ± 0.2 Å per residue (236) and the length of a 5 kDa PEG molecule has been estimated at 355 ± 45 Å (237). These measurements imply the length between the centers of adjacent crosslinked PEG molecules is ~77.4 nm compared to ~ 80.6 nm for VPMS and 2xVPMS crosslinked hydrogels if fully extended. Moreover, a similar study of PEG hydrogels in which a single recognition sequence was compared to a triple repeat (713 and 1889 g/mol, respectively) demonstrated no significant effect on hydrogel properties (91) despite being a larger difference in crosslinker MW than VPMS compared to 2xVPMS (1738 and 2554 g/mol). Moreover, the initial hydrogel mechanical properties for VPMS and 2xVPMS hydrogels were tightly controlled, demonstrating that the enhanced vessel formation in 2xVPMS hydrogels was due to differences in proteolytic susceptibility rather than changes in mechanics or network structure.

Although co-cultures in both VPMS and 2xVPMS hydrogels demonstrated increased total nuclei densities over time, there was no significant differences depending on crosslink identity. This suggests that differences in vessel formation were not attributable to differences in

cellular proliferation. Possible explanations for differences in vessel formation without differences in cellular proliferation may be due to enhanced cell spreading or migration in 2xVPMS hydrogels during network self-assembly.

Hydrogel mechanics were tracked over time to assess whether enhanced proteolytic susceptibility negatively affected hydrogel integrity during culture. On the contrary, enhanced matrix degradability resulted in a stiffer matrix after *in vitro* culture. Both VPMS and 2xVPMS hydrogels stiffened over time, with 2xVPMS hydrogels stiffening significantly more than VPMS. Cellular remodeling processes associated with this stiffening behavior are thoroughly investigated in **Chapter 6** of this dissertation, but briefly; they depend on active cellular contractility and correlate with enhanced collagen deposition and the degree of network formation (238).

A preliminary study of hydrogels implanted in a subcutaneous pocket suggested that enhanced hydrogel degradability may support improved vessel formation and cell spreading *in vivo*, but morphogenesis is severely restricted compared to *in vitro*. CB17/SCID mice were chosen because they lack T and B cells resulting in a deficient acquired immune system, allowing them to accept foreign tissue transplants. Myelopoiesis and the innate immune system, however, remain intact (239) allowing for cellular invasion of tissue implants. Implantation of intact hydrogels, rather than injection of hydrogel precursor solutions for *in situ* gelation as has been done before (114), was chosen for precise control of hydrogel mechanics. PEG hydrogel mechanics strongly affect degree of vessel formation (231), and need to be controlled to accurately assess differences depending on crosslink identity. PEG hydrogel gelation and resultant mechanics are very sensitive to impurities, as demonstrated by the 2-fold reduction of material properties with incorporation of a cell pellet. As such, the mechanics may be difficult to

control with *in situ* gelation because of stochastic differences in incorporated impurities between implant sites.

Whole mount confocal imaging of explanted hydrogels suggested that cell spreading and formation of vessel-like structures was more pronounced in a 2xVPMS hydrogel than its paired VPMS hydrogel. There, however, was no robust interconnected network formation as observed in their paired *in vitro* controls. Whole mount confocal imaging of explants provides assessment of the 3D structure of networks formed during implantation and allows direct comparison between *in vivo* and *in vitro* samples. Moreover, whole mount imaging avoids processing artifacts associated with hydrogel embedment necessary for histological sectioning, which are well-known to deform synthetic hydrogels (240–242). Substantial processing artifacts were evident in the histological assessment of some the hydrogel implants. Coincidently, processing artifacts for both the acellular and cellular 2xVPMS implants precluded comparison to their paired VPMS implants. Sections from the VPMS implants, however, were useful for qualitatively evaluating the presence of host infiltration into the acellular hydrogel and a potential foreign body response to the implant. Highly basophilic cells appeared to infiltrate the PEG implant on the surface adjacent to the muscle. These cells appeared morphologically similar to granulocytes, but further histological analysis would be needed to assess their identity. There also appeared to be a single continuous cellular projection emanating from the skin. Cellular invasion into similar hydrogels in subcutaneous pockets have been demonstrated, with a high density of cells infiltrating a VPMS-crosslinked PEG hydrogel up to 400 μm away from the tissue interface after 12 weeks in one study (123) and vascularized tissue projections from surrounding tissue into a proteolytically degradable PEG hydrogel observable at 14 days in another study (134). The ostensive foreign body response to our hydrogel implants may have

contributed to the relatively restricted morphogenesis and minimal integration with the host. The foreign body response to non-degradable, high density (200 mg/ml) PEG-hydrogels in a subcutaneous implant model in immunocompetent mice has previously been assessed and extensive fibrous capsule formation was observed (243). This inflammatory response was dependent on inflammatory protein adhesion, but was reduced when RGD was conjugated to the hydrogel (244).

Although no inosculation with the host was observed in our preliminary study after 1 week, angiogenic invasion and perfusion of similar VPMS hydrogels containing pancreatic islets, but no endothelial or stromal cells, has been shown to occur in 5 weeks (121). Moreover, angiogenic invasion of MMP-degradable PEG hydrogels has been significantly improved with cell demanded release of VEGF from implants (106, 107, 121) and fibroblasts have been demonstrated to secrete VEGF *in vitro* (52, 245). These previous studies suggest that despite possible capsule formation, angiogenic invasion and inosculation may be feasible at longer time points in this subcutaneous implant model.